CHALMERS
UNIVERSITY OF TECHNOLOGY

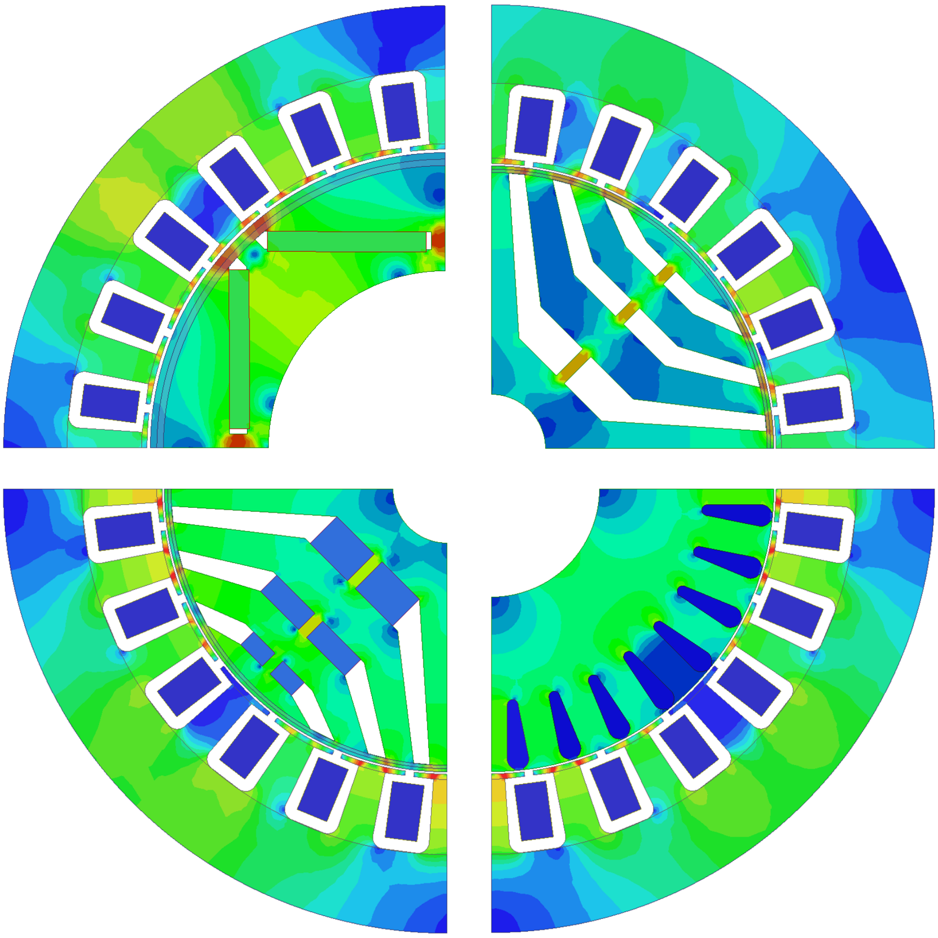

Electric Machine Comparison for Mild Hybrid Light Vehicles with Respect to Performance and Thermal Capability

Master's Thesis in Electrical Power Engineering

SEBASTIAN LARQVIST
HANNES ÖSTERGREN

Department of Energy and Environment
CHALMERS UNIVERSITY OF TECHNOLOGY
Gothenburg, Sweden 2017

MASTER'S THESIS 2017

Electric Machine Comparison for Mild Hybrid Light Vehicles with Respect to Performance and Thermal Capability

SEBASTIAN LARQVIST AND HANNES ÖSTERGREN

Department of Energy and Environment
Division of Electric Power Engineering
CHALMERS UNIVERSITY OF TECHNOLOGY
Gothenburg, Sweden 2017

Electric Machine Comparison for Mild Hybrid Light Vehicles
with Respect to Performance and Thermal Capability
Sebastian Larqvist & Hannes Östergren

Supervisors:
Stefan Skoog, Chalmers University of Technology
Patrik Stridh, Volvo Car Corporation
Alexander Robertsson, Volvo Car Corporation

Examiner:
Torbjörn Thiringer, Chalmers University of Technology

Master's Thesis 2017
Department of Energy and Environment
Division of Electric Power Engineering
Chalmers University of Technology
SE-412 96 Gothenburg
Telephone +46 (0)31 772 1622

Cover: Field plots over magnetic flux density in four studied machine topologies: PMSM, SynRM, PMSynRM and IM.

Gothenburg, Sweden 2017

Electric Machine Comparison for Mild Hybrid Light Vehicles
with Respect to Performance and Thermal Capability
SEBASTIAN LARQVIST
HANNES ÖSTERGREN
Department of Energy and Environment
Chalmers University of Technology

Abstract

In this thesis, various electric machine topologies have been modeled and optimized according to constraints related to mild hybrid applications. With the assistance of electromagnetic field calculation software using FEM simulations, the performance characteristics as well as thermal capability have been analyzed. By utilizing full vehicle simulations, the machines have been evaluated and the performance quantified when they are implemented in a 48 V mild hybrid system. Moreover, power losses for whole operating regions in various machine components have been specified, which are used as input data for the thermal models. From the thermal model, the temperature distribution within the machines have been determined during continuous operation. In this work, four machine topologies were chosen to be studied: PMSM, SynRM, PMSynRM and IM. A number of operating points relevant to mild hybrid systems were selected to be used as basis for the performance comparison.

From the simulations, it was found that the 8-pole PMSM has the highest operating efficiency of 96.9 %. The implemented ferrite magnets of the PMSynRM improve the highest operating efficiency by 1 % and increase the maximum torque by 7 Nm compared to the SynRM. The PMSM and the IM fulfill the cold crank torque requirement, and all machines can be operated at 10 kW continuously without exceeding the critical temperature limits. The SynRM has the most environmental friendly design in terms of material combination, emissions are 53 % less in comparison the 4-pole PMSM.

To conclude, due to beneficial properties such as high power and torque density, along with great performance in the specified operating points and solid thermal characteristics, the PMSM topology is found to be an interesting option to be utilized in mild hybrid traction applications. Furthermore, the ferrite magnets in the PMSynRM makes likewise this machine topology an interesting alternative to be applied in mild hybrids, due to the overall high operating performance in relation to its low material cost and CO_2 equivalent per produced machine.

Keywords: Mild Hybrid, Electric Vehicle, Electric Machine, PMSM, SynRM, IM, FEM, Operating Efficiency, Thermal Capability.

Acknowledgements

First of all, we would like thank our main supervisor Stefan Skoog for his vital support, feedback, and for sharing his inspiring research in the field of mild hybrid applications with us. We would also like to express our sincere gratitude towards our examiner Professor Torbjörn Thiringer, for always dedicating his time and his great encouragement during the thesis work. Furthermore, we would like to thank our supervisors at Volvo Cars, Patrik Stridh and Alexander Robertsson, for their commitment and for deepen our knowledge within the field of electrified vehicles. In addition, we would like to address our appreciation to Andreas Andersson for his helpful advice regarding FEM simulations, and to Emma Arfa Grunditz for her guidance concerning thermal modeling of electric machines.

I, Sebastian, would like to thank my family and friends for the continuous love and encouragement throughout the years, your support means everything.

I, Hannes, give my warmest thanks to my family, especially my dear fiancée Emma for the endless love and support through all the years.

Sebastian Larqvist & Hannes Östergren, Gothenburg, June 2017

List of Abbreviations

BEV	Battery Electric Vehicle
BSG	Belt Driven Starter-Generator
emf	Electromotive Force
FEM	Finite Element Method
HEV	Hybrid Electric Vehicle
ICE	Internal Combustion Engine
IM	Induction Machine
IPMSM	Interior Permanent Magnet Synchronous Machine
ISG	Integrated Starter-Generator
MTPA	Maximum Torque Per Ampere
PM	Permanent Magnet
PMSynRM	Permanent Magnet Assisted Synchronous Reluctance Machine
PMSM	Permanent Magnet Synchronous Machine
SRM	Switched Reluctance Machine
SynRM	Synchronous Reluctance Machine

Contents

1 Introduction **1**
- 1.1 Problem background . . . 1
- 1.2 Previous work . . . 2
- 1.3 Thesis aim and contributions . . . 2
- 1.4 Scope . . . 3

2 The 48 V Mild Hybrid System **5**
- 2.1 Characteristics of the 48 V system voltage level . . . 5
- 2.2 HEV drivetrain configurations . . . 7
  - 2.2.1 Series hybrid . . . 7
  - 2.2.2 Parallel hybrid . . . 7
  - 2.2.3 Mild hybrid . . . 8
- 2.3 Electric machine operation modes in a mild hybrid drivetrain . . . 9
  - 2.3.1 ICE cranking and idle stop and start . . . 9
  - 2.3.2 Power generation and regenerative braking . . . 10
  - 2.3.3 Power boost mode . . . 10
  - 2.3.4 Coasting mode . . . 10

3 The Electric Machines **11**
- 3.1 Basic electromagnetic theory . . . 11
- 3.2 Permanent Magnet Synchronous Machine . . . 14
  - 3.2.1 Steady state model . . . 14
  - 3.2.2 Mechanical output . . . 15
  - 3.2.3 Power losses . . . 16
  - 3.2.4 Control strategy . . . 16
- 3.3 Synchronous Reluctance Machine . . . 17
  - 3.3.1 Concept of reluctance . . . 17
  - 3.3.2 Steady state model . . . 18
  - 3.3.3 Mechanical output and power losses . . . 18
- 3.4 Induction Machine . . . 19
  - 3.4.1 Steady state model . . . 19
  - 3.4.2 Mechanical output . . . 20
  - 3.4.3 Power losses . . . 21
- 3.5 Thermal modeling . . . 21
  - 3.5.1 Modes of heat transfer . . . 21
  - 3.5.2 Lumped-parameter network modeling . . . 22

4 Case Setup **25**
4.1 Operating points of interest . . . 25
4.2 Machine scaling . . . 26
4.3 Operating limits . . . 26
4.4 Optimization of PMSM model . . . 27
4.5 Simulation setup . . . 29
4.5.1 PMSM . . . 29
4.5.2 SynRM . . . 32
4.5.3 PMSynRM . . . 34
4.5.4 IM . . . 36

5 Analysis of Performance and Vehicle Simulations **39**
5.1 Analysis of efficiency and losses . . . 39
5.1.1 Initial attempt on the IM . . . 47
5.2 Comparative evaluation of performance . . . 48
5.3 Full vehicle system simulations . . . 51
5.3.1 Highway drive . . . 52
5.3.2 City drive . . . 54

6 Implementation and Evaluation of Thermal Models **57**
6.1 Lumped-parameter network models . . . 57
6.1.1 Stator frame and cooling . . . 59
6.1.2 Stator yoke . . . 60
6.1.3 Stator teeth . . . 60
6.1.4 Stator windings . . . 61
6.1.5 Internal air . . . 63
6.1.6 Air gap . . . 64
6.1.7 Rotor core . . . 64
6.1.7.1 PMSM . . . 65
6.1.7.2 SynRM . . . 66
6.1.7.3 PMSynRM . . . 67
6.1.8 Shaft . . . 68
6.1.9 Bearings . . . 69
6.1.10 Summary of thermal resistances and capacitances . . . 70
6.2 Losses in machine parts . . . 70
6.3 Transient thermal response comparison . . . 74

7 Conclusions and Future Work **77**
7.1 Conclusions . . . 77
7.2 Future work . . . 78

Bibliography **81**

1
Introduction

1.1 Problem background

In today's global society one of the leading challenges is to restrain the negative impacts and consequences of global warming. The transportation sector is one of the main sources in the contribution of greenhouse gas emissions such as CO_2 and NO_x [1]. Therefore, the European Union and other governments are constantly challenging vehicle manufacturers with more stringent emission targets and enforced by law from the year of 2021, the fleet average of a manufacturer are not allowed to exceed an emission limit of 95 gCO_2/km [2]. This limit corresponds to a fuel consumption of approximately 4.1 liters/100km for petrol and 3.6 liters/100km for diesel, for the specified certification drive cycles. To cope with this limitation, vehicle manufacturers are investing in fuel saving solutions and introducing alternative powertrain technologies such as hybrid electric vehicles (HEVs) and battery electric vehicles (BEVs) in order to increase the vehicle electrification and to assist or completely replace the more traditional internal combustion engine (ICE).

The increasing vehicle electrification and requirements of the vehicle power supply have taken the existing 12 V power system to its operating limits. A new type of hybrid solution is the mild HEV which utilizes a low voltage electric machine supplied by a 48 V power system, in addition to the existing 12 V system [3]. By increasing the operating voltage level to 48 V, the system will be able to supply additional and larger electrical power loads in the vehicle at lower current magnitudes and thus increasing the overall system efficiency. The system has the potential to lower the fuel consumption and therefore also lower the emissions due to the more beneficial system efficiency on the 48 V side. In addition to operate as a combined alternator and starter, the electric machine will also have the ability to perform regenerative braking, power boost and coasting.

Since the 48 V system is a fairly new technical solution, there is not much research published in the subject regarding reduced CO_2 emissions. Therefore, it is highly desirable to evaluate the impacts in CO_2 emissions for a mild HEV powertrain and how they differ when different kinds of electric machine topologies are utilized in the system. Hence, the project will focus on the electric machine as a part of the mild HEV powertrain and evaluate the suitability of different machine topologies in a mild HEV system.

1.2 Previous work

There exists several interesting publications in the theme of comparative performance studies of electric machine topologies applicable for BEVs and HEVs. A common approach is to compare the topologies of interest to a reference machine, where in many cases this reference machine is an interior permanent magnet synchronous machine (IPMSM) based on the Toyota Prius 2010 machine [4], [5] and [6].

In addition to this, topologies without any permanent magnets in the rotor such as the induction machine (IM), the synchronous reluctance machine (SynRM) and the switched reluctance machine (SRM) are evaluated as solutions for the electric drive system in vehicle applications [6], [7] and [8]. The impacts of when the electric machine is implemented in a mild HEV solution have however not been evaluated in the same extend as for BEVs or HEVs. The PMSM is one of the most popular machine topologies to discuss due to its attractive characteristics, such as high power density, and studies of this topology in mild HEV applications can be found in [9], [10]. Moreover, numerous publications regarding electric machine design optimization have been reported [11], [12].

To conclude, a commonly used approach in the subject is to have fixed machine performance data as basis, such as required power and torque ratings, and thus the final results present an indication of the geometrical dimensions of each machine in order to provide the desired performance [13]. The opposite approach is adopted in this work, i.e. the position and the geometrical constraints of the electric machine in the mild HEV system are known and used as basis for the performance analysis.

1.3 Thesis aim and contributions

The aim of the work is to provide a comparison with respect to performance and thermal capability between various electric machine topologies in a 48 V mild hybrid system. Since there exists a strict limited amount of space in today's propulsion systems, the comparison takes into consideration constraints such as geometrical dimensions and required performance ratings. Based upon the technical constraints, the performance of each machine is quantified in parameters such as operating efficiency, power density and suitability for operating points considered relevant for the 48 V mild HEV system.

Moreover, an aim was to model the thermal capability and characteristics of the machines, which brought a need to determine the power losses in the main components of the machines. By utilizing existing full vehicle system simulations, the characteristics of the machines are related their operating performance when they are implemented in a 48 V mild HEV system. A final goal of the study was to evaluate the environmental impact related to the machine construction, in order to determine the suitability of mass production as well as the sustainability.

The main contributions of the work are:

- Machine design of various electric machine topologies with electromagnetic field software using FEM analyses and with few simulation iterations

- Comparative performance analysis of electric machines considered favorable for mild HEV applications, evaluated in key target parameters such as operating efficiency, power losses in the whole operating region as well as output power and torque density
- Determination of environmental impacts in the form of CO_2 emissions and costs related to the extraction of raw materials required for manufacturing respective machine topology
- Establishing thermal networks required for quantifying the thermal characteristics in different machine parts during continuous operation of electric machines.

1.4 Scope

The scope of the work is focusing on the performance of the electric machine topologies, both individually and during standardized driving cycles, as well as the thermal capability. The study has its focus on the electric machine performance only, and hence other components in the power system such as the inverter, cables and energy storage system are not included in the comparison. Voltage variations on the 48 V bus during motor and regeneration drive are neglected. The machines are modeled and optimized through electromagnetic field software using FEM analyses, and are limited to 3-phase machines. The machines are not build or physically modeled. Furthermore, the focus have been on well known machine topologies, that can be easily mass produced and has previously known qualities that are considered favorable for HEV applications. Moreover, the optimization process of each topology is limited to a few iterations due the time constraints.

The social and ethical aspects of the manufacturing of permanent magnets utilized in some of the machine topologies must be taken into consideration while designing the machines. As the mining and processing of the rare-earth materials mainly take place in China, companies can avoid strict environmental and social regulations [14]. A multitude of the rare-earth materials is highly toxic and in some cases even radioactive, and hence inhaling or ingestion these materials can cause severe organ damage. Therefore, the whole process must be carefully monitored and regulated to avoid harmful conditions for the workers in the mine, but also residents of the mining town which are in the danger zone of inhaling higher amounts of radioactive dust.

2
The 48 V Mild Hybrid System

In order to accomplish reduced CO_2 emissions in the transportation section, more efficient and environmental friendly drivetrain solutions are constantly under development. These type of influences lead to an increasing vehicle electrification. The operation of existing high power loads such as the water pump and air condition compressor are transferred from the ICE, in order to be operated independently and fully electrically [3]. In addition, new high power loads can be applied and an increasing vehicle power supply system enhances the possibilities to enable new functions for the integrated electric machine, which likewise can contribute to reduced CO_2 emissions. Due to the increasing electrical requirements, today's existing 12 V vehicle power supply has reached its practical operating limits. It is not sufficient enough to supply the required demand and has to prioritize important power loads at the expense of others. One of the key components to fulfill the increasing requirements is the degree of electrification of the drivetrain. Hence vehicle manufactures are upgrading the existing 12 V electrical system to a voltage level of 48 V, which establish the concept of mild HEVs.

2.1 Characteristics of the 48 V system voltage level

A typical 48 V mild hybrid system can consist of e.g. a belt driven starter-generator (BSG) at 10 kW peak power, or an integrated starter-generator (ISG) at 20 kW peak power [15]. Figure 2.1 shows the gain in continuous power output at certain current magnitudes for a transition from 12 V to 48 V on-board voltage level.

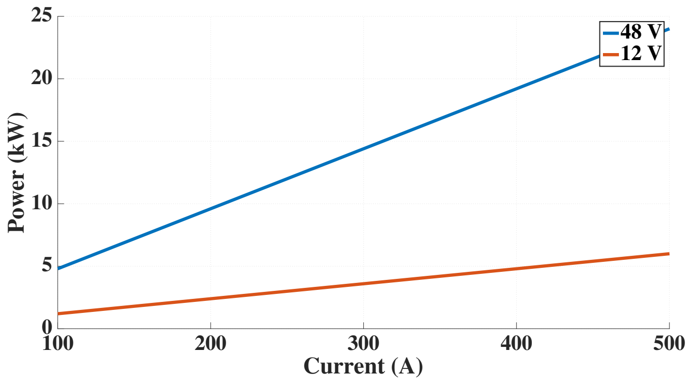

Figure 2.1 Power and current relation at operating voltages of 12 V and 48 V.

Regarding the trade-off between power output, safety and functionality, the 48 V mild hybrid power supply could be considered as a suitable option for mild vehicle electrification. It provides an opportunity to introduce a cost-optimized hybrid drivetrain solution, since the energy storage system does not need to have the same requirements on electrical safety, as in a BEV or HEV with higher voltage levels [16]. Since the operating voltage is below 60 V, electrical shock protection is not required. Figure 2.2 presents the operating range and voltage limits of the 48 V system according to the LV 148 standard, which has been issued by several vehicle manufactures [3].

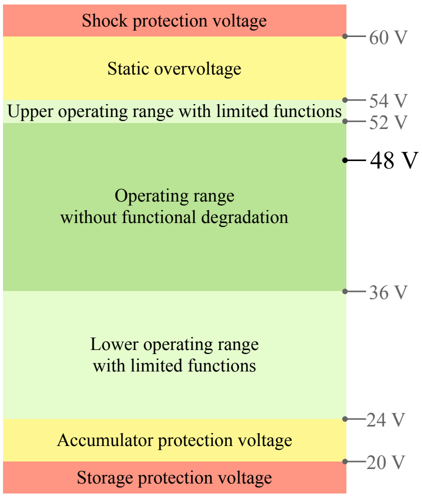

Figure 2.2 Operating range and voltage limits of the 48 V system according to the LV 148 standard.

The baseline of a 48 V power supply can be exemplified as illustrated in Figure 2.3, where it is implemented in a dual net topology with the already existing 12 V power supply through a DC-DC converter. Minor power loads such as the infotainment system are supplied by a 12 V battery, while the mild hybrid electric machine and other high power loads such as cooling fan and heating system are supplied by a 48 V battery. Additionally, the 48 V system enables mechanical loads to be alternatively electrically supplied, e.g. an electric climate compressor, and thus removing loads from the low-efficient accessory drive system of the ICE.

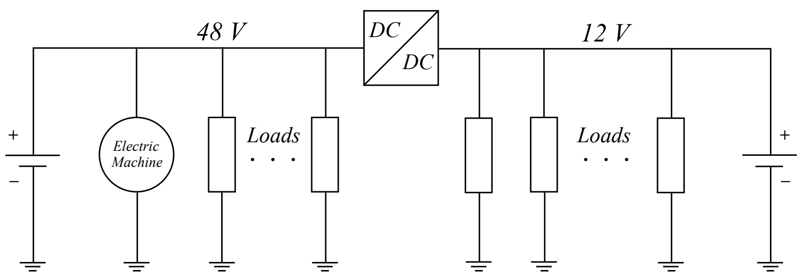

Figure 2.3 Baseline example of the 48 V power supply in a dual net topology with the 12 V system.

2.2 HEV drivetrain configurations

HEVs can be classified as series, parallel and mild hybrids depending on the power flow and the rating of the energy storage system utilized in the vehicle's drivetrain configuration.

2.2.1 Series hybrid

The series hybrid drivetrain configuration is often considered as the most elementary configuration. It has the simplest structure with two sources of energy and one single path for the mechanical power traction. It is the electric machine only that provides the driving power through the transmission to the wheels and thus this configuration is known as an electrically coupled drivetrain [17]. Depending on the control strategy, the electric machine is supplied with electric power either from a generator driven by an ICE, or a battery pack. A simple schematic sketch of a series hybrid drivetrain configuration is illustrated in Figure 2.4.

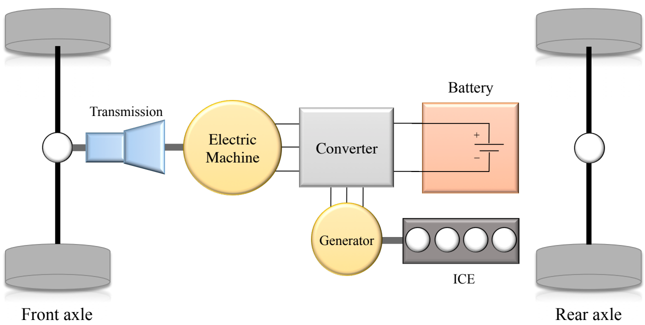

Figure 2.4 Simple schematic sketch of a series hybrid drivetrain configuration.

The ICE tends to be smaller in a series hybrid, since it does not directly drive the vehicle and by controlling it in such a way that it operates in optimal regions with high efficiency, fuel consumption can be lowered. The series hybrid can therefore be considered as suitable for suburban driving conditions. Due to a less powerful ICE, the battery pack in a series drivetrain needs to be larger in order to meet the required power demand. It also requires two electric machines, which makes them more costly and larger in size compared to a parallel drivetrain.

2.2.2 Parallel hybrid

Unlike in the series drivetrain, both the electric machine and the ICE can at the same time instance provide the required driving power through the transmission to the wheels in the parallel hybrid drivetrain configuration, and it is hence known as a mechanically coupled drivetrain. There exists fewer energy conversion steps since the ICE is directly connected to the driveshaft and consequently the overall efficiency is higher compared to a series hybrid [17]. Furthermore, irrespective of the size and power rating of the electric machine and battery pack, enhanced performance in the total powertrain are provided since the path for all propulsion power does not need to go through the electric machine. Figure 2.5 shows a simple schematic sketch of a parallel hybrid drivetrain configuration. The ICE and the electric machine need to be efficiently coupled in order to not affect the vehicle driving performance, which requires a complex control system.

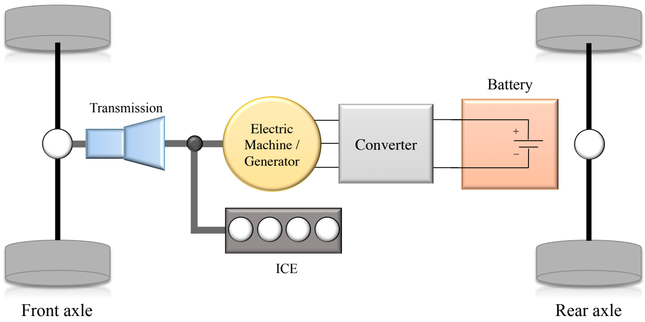

Figure 2.5 Simple schematic sketch of a parallel hybrid drivetrain configuration.

2.2.3 Mild hybrid

The mild hybrid drivetrain configuration is essentially a conventional ICE vehicle with an integrated electric machine with low power rating, and does therefore not require a large energy storage system [16]. As in the parallel drivetrain configuration, both the ICE and the electric machine can provide propulsion power to the wheels at the same time instance. However, the mild hybrid drivetrain has limited power capacity and functionality compared to the parallel hybrid drivetrain. There exists several mild hybrid system topologies depending on the position P0-P4 of the integrated electric machine, which are schematically presented in Figure 2.6.

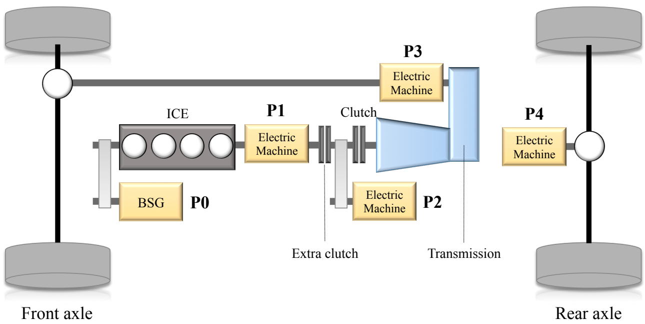

Figure 2.6 Simple schematic sketch of a mild hybrid drivetrain configuration with five system topologies (P0-P4).

The P0 topology features a BSG directly coupled to the ICE. It is a low cost solution, but with limitations in provided power and torque. In the P1 topology the electric machine is directly mounted on the crankshaft as an ISG located between the ICE and the transmission, replacing the inertia from the flywheel. This solution possess the ability to provide more torque compared to the P0 topology, but has the drawback of inefficient regenerative braking since the electric machine is always coupled to the ICE and will hence experience high mechanical friction losses from the ICE [18].

A solution to this issue is to implement the electric machine as shown in the P2 topology, with an additional clutch that can disconnect the ICE and hence reducing the mechanical friction losses. The electric machine can either be implemented as a side attached BSG or as an ISG directly mounted on the crankshaft as in the P1 topology. In a side attached configuration, the electric machine runs at a higher speed than the ICE, often with a transmission ratio of 1:2.7 [19], [20]. Since the ICE can be fully disconnected, the solution possess high regenerative braking capability and potential to propel the vehicle electrically [18].

In the P3 system topology the electric machine is mounted on the transmission to the front axle, while in the P4 topology it is directly integrated to the rear axle. P3 and P4 possess the highest regenerative braking potential, but does not provide as wide range of hybrid functions compared to the P2 topology. Moreover, the electric machine can also be integrated in the wheel hub, where the configuration is then titled as the P5 topology.

2.3 Electric machine operation modes in a mild hybrid drivetrain

Depending on the drivetrain configuration and integrated position of the electric machine, multiple operation modes are enabled in a mild HEV [15]-[18], [21]-[23]. ICE cranking and power generation are inherited from conventional vehicles with 12 V power supply system, while the other operation modes are unique for mild HEVs and vehicles with higher degree of electrification.

2.3.1 ICE cranking and idle stop and start

ICE cranking is the initial operating mode of the electric machine. When the ignition is switched on, the machine energizes the ICE by providing sufficient torque to accelerate the crankshaft to minimum operating speed, in order to initiate the combustion process. The crank torque is often required to be as high as 50-55 Nm [9], [23], or three to four times the nominal torque [12], in order to overpower the substantial resistance of the kinematic mechanism and is at its peak during cold climate conditions.

An additional applicable cranking operation is the idle stop and start function, which is already commonly utilized in modern HEVs. When the vehicle is at rest the electric machine shuts down the ICE and hence reduce the fuel consumption and CO_2 emissions significantly during urban city driving.

2.3.2 Power generation and regenerative braking

Once the ICE has taken control over the propulsion process, the electric machine operates in power generation mode as a conventional alternator. By converting the mechanical energy from the rotating crankshaft, it supplies the on-board electric loads in the vehicle and recharges the battery in order to maintain a steady state-of-charge level and hence prolonging the battery life time.

Moreover, compared to a conventional alternator the electric machine in a mild HEV possess the ability to perform generative braking. When the accelerator pedal is released or when the braking pedal is pressed, a regenerative braking torque is provided and the kinetic energy of the vehicle is utilized by the electric machine in order to charge the battery.

2.3.3 Power boost mode

In situations when the vehicle needs to perform launching, overtaking or uphill driving, the electric machine operates as a motor providing power boost for rapid accelerations. It assists the ICE with additional torque in order to fulfill the desired power demand. Furthermore, this operation enables to downsize the ICE without affecting the performance.

2.3.4 Coasting mode

A drivetrain concept with an additional clutch between the ICE and the electric machine, as shown in Figure 2.6, allows the ICE to be disconnected in order to let the vehicle be driven fully electrically. Since the power rating of the electric machine integrated in a mild HEV is lower compared to vehicles with higher degree of electrification, this operating mode is primarily applicable in limited range and constant speed situations, and is hence referred to as coasting mode.

3

The Electric Machines

Following chapter provides an insight into basic concepts regarding electric machine operation, what is considered to be necessary information about the machine topologies studied in this work as well as thermal modeling of electric machines.

3.1 Basic electromagnetic theory

To completely understand the operation principles of electric machines, it is necessary to study some basic electromagnetic theory. By applying a current through a conductor a surrounding magnetic field is generated around it, where the field strength is highest close to the conductor surface. With the knowledge of the current direction, the orientation of the magnetic field flux can be determined by the "Right Hand Rule". Figure 3.1 shows the magnetic flux lines and how they are superimposed in a parallel go and return circuit.

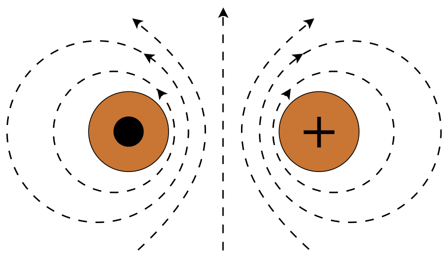

Figure 3.1 Magnetic flux lines in a parallel go and return circuit.

By wrapping the current carrying conductor in multiple parallel go and return circuits a coil is formed, and each turn of the coil will increase the magnetic field inside it. The coil's ability to produce a magnetic flux is defined as its magnetomotive force MMF and can be expressed as

$$MMF = NI \tag{3.1}$$

where N is the number of turns of the coil and I is the current in the circuit. In order to concentrate the flux and prevent it from spreading out into the surrounding space the coil is wrapped around an iron core with an air gap, as depicted in Figure 3.2.

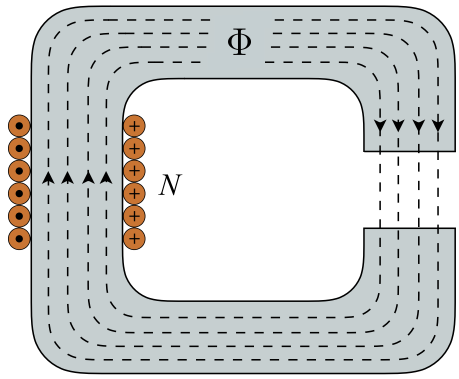

Figure 3.2 Magnetic flux lines circulating inside an iron core with an air gap.

Since iron is a material with low reluctance and hence possess good magnetic properties, the flux will stay inside the core and complete its circuit through the core and the air gap. By shaping the iron it is thus possible to guide the flux to wherever it is needed. The magnetic flux Φ (Wb) through a bounding surface of an arbitrary volume can be expressed as

$$\Phi = \iint B \, dS \tag{3.2}$$

where B is the magnetic flux density (T or Wb/m^2) and dS is the differential area of the bounding surface. According to Ampère's Circuital Law, the magnetic field intensity along any closed circuit is equal to the enclosed current flowing through the surface bounded by the circuit and can be mathematically represented as

$$\oint H \, dl = \iint J \, dS = I_{enclosed} \tag{3.3}$$

where H is the magnetic field intensity (A/m), dl is the differential length of the closed circuit, J is the current density (A/m^2) and $I_{enclosed}$ is the enclosed current. The relation between the flux density and the field intensity can be defined as

$$B = \mu_0 \mu_r H \tag{3.4}$$

where μ_0 is the permeability of free space and μ_r is the relative permeability, which varies considerably between different materials and also with the local magnetic field intensity level. Since the relative permeability of iron is much higher than the relative permeability of air, the magnetic field intensity will be greater in the air gap than in the iron core. This is however only valid for small air gaps since the reluctance of the air gap increases proportionally with its length.

One important parameter in electric machine applications is the magnetic flux linkage Ψ (Wb). A coil is multiple loops of a current carrying conductor linked together, and by linking these loops the effect of the total magnetic influence going through the loops is increased. The flux linkage of a coil can be calculated as

$$\Psi_{coil} = N \Phi_{coil} \tag{3.5}$$

where Φ_{coil} represents the magnetic flux of the coil.

According to Faraday's Law of Induction, a fluctuating magnetic field will induce a voltage in an electromagnetic circuit located inside the field. This can be mathematically expressed as

$$e = -\frac{d\Psi}{dt} \tag{3.6}$$

where e is the electromotive force (emf).

The inductance L of an electromagnetic circuit can be calculated as followed.

$$L = \frac{\Psi}{I} \tag{3.7}$$

When an AC current is flowing through a winding, the winding can be represented by a resistive and an inductive element. This will cause a voltage drop over the winding and the voltage v can be calculated as

$$v = Ri + L\frac{di}{dt} \tag{3.8}$$

where R is the winding resistance and i is the current.

If a permanent magnet (PM) is placed in the pulsating magnetic field in the air gap of the iron core, the PM will start to rotate with an angular speed of ω_r (rad/s) [24], as depicted in Figure 3.3.

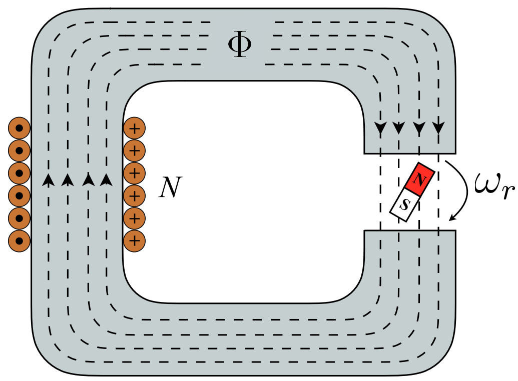

Figure 3.3 Rotating PM located inside the magnetic field in the air gap of the iron core.

This is the most basic operation principle of electric machines. Due to the presence of the rotating PM, the voltage can now be expressed as

$$v = Ri + L\frac{di}{dt} + \omega_r \Psi_m \cos(\omega_r t) \tag{3.9}$$

where Ψ_m is the flux linkage of the PM.

3.2 Permanent Magnet Synchronous Machine

The permanent magnet synchronous machine (PMSM) is one of the most popular choices and widely used electric machines in the field of HEV applications. It is often considered as the most adequate alternative due to advantageous properties such as superior power density and high overall efficiency in the nominal speed range [13].

In the same way as for the additional electric machines studied in this work, the PMSM stator consists of highly permeable laminated steel plates with equidistantly distributed slots containing copper windings. When the windings are excited by an external three phase AC supply, a revolving magnetic field is generated inside the stator core which rotates at synchronous speed.

The rotor of the PMSM typically consists of highly permeable laminated steel plates which as for the stator serve as conduction path for the magnetic flux, and high energy PMs which establish the rotor excitation. Interaction between the constant magnetic field of the rotor and the revolving magnetic field of the stator causes the rotor capable of running at synchronous speed. The PMs can either be surface, inset or interior mounted, and due to their ability to establish a substantial magnetic flux in the air gap without any excitation current it is possible to design PMSMs with high overall efficiencies [7].

3.2.1 Steady state model

A commonly used approach is to electrically model the PMSM by dynamic dq-representation, as shown in Figure 3.4, where the d-axis is directed in the direction of the rotor magnetic flux, while the q-axis is located 90 electrical degrees ahead of the d-axis [22].

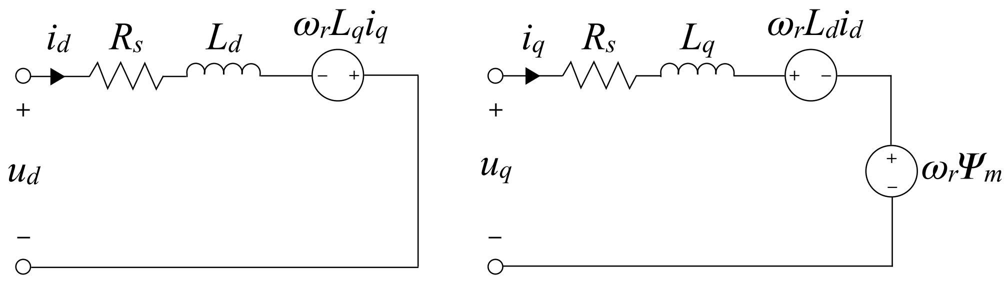

Figure 3.4 PMSM electric model by dynamic dq-representation.

Stator voltage equations can then be defined as

$$u_d = R_s i_d + L_d \frac{di_d}{dt} - \omega_r L_q i_q \tag{3.10}$$

$$u_q = R_s i_q + L_q \frac{di_q}{dt} + \omega_r L_d i_d + \omega_r \Psi_m \tag{3.11}$$

where R_s is the stator resistance, i_d and i_q are the d- and q-axis stator currents, L_d and L_q are the d- and q-axis stator winding inductances, ω_r is the electrical rotor angular speed and Ψ_m is the flux linkage related to the PMs in the rotor. Since the electrical system has a much smaller time constant in relation to the mechanical system, the stator voltage equations can be reformulated as

$$u_d = R_s i_d - \omega_r L_q i_q \tag{3.12}$$

$$u_q = R_s i_q + \omega_r L_d i_d + \omega_r \Psi_m \tag{3.13}$$

where the current time derivative is neglected and thus electrical steady state is achieved.

3.2.2 Mechanical output

The electromechanical torque output can be expressed as

$$T_e = \frac{3n_p}{2}(\Psi_m i_q + (L_d - L_q) i_d i_q) \tag{3.14}$$

where n_p is the number of pole pairs in the machine. The electromechanical torque expression can be broken down into two main parts, which come from the PM torque production T_m arising from the PM flux and a reluctance torque production T_{rel} arising from the rotor saliency, which are defined as

$$T_m = \frac{3n_p}{2}(\Psi_m i_q) \tag{3.15}$$

$$T_{rel} = \frac{3n_p}{2}(L_d - L_q) i_d i_q \tag{3.16}$$

where L_q often is larger than L_d, due to higher reluctance properties in the PMs in comparison to the steel material. In order for the reluctance torque to provide a positive torque production, i_d needs to be negative [22].

The characteristics of the mechanical output can be categorized into one constant torque operation region and one constant power operation region. Starting from zero speed, the constant torque region provides maximum torque production at any speed, and continuously increasing power production with the speed of the machine. In order to counteract the rising back-emf, the applied voltage needs to increase but when the maximum voltage limit of the energy storage system is hit, it cannot increase further. This speed level is defined as the nominal speed of the machine and is also where the peak power operation occurs. To be able to further increase the speed, the d-axis flux linkage needs to be reduced to counteract the continuously rising back-emf, and thus the constant power region is also known as the field weakening region. This is achieved by applying higher current in the negative d-direction. In order to maintain a constant current magnitude, the q-axis current needs to be decreased and since the torque production is mainly related to the q-axis current, maximum torque output will decline in the constant power region, while the output power retain a flat profile characteristic.

3.2.3 Power losses

The power losses in the PMSM can be approximately categorized as resistive losses in the stator copper windings and iron losses which are mainly found in the stator core. The copper losses can be calculated from

$$P_{cu} = 3R_s I_{s,rms}^2 \tag{3.17}$$

where the rms phase current $I_{s,rms}$ can be written in dq-representation as $\sqrt{i_d^2 + i_q^2}$. The iron losses mostly depends on magnetic hysteresis and induced eddy currents and can be expressed as [25]

$$P_{fe} = k_h f B_{pk}^n + k_c f^2 B_{pk}^2 \tag{3.18}$$

where k_h and k_c are hysteresis respectively eddy current parameters, f is the frequency of the magnetic flux in the iron material, B_{pk} is the peak flux density in the B-H hysteresis curve, and n is a parameter dependent on B_{pk}, f and the steel material.

The power losses in the rotor in a PMSM are typically small due to the lack of windings. Hence losses in the rotor mainly consists of eddy current losses in the iron core and the PMs. In order to minimize these losses, design features such as thinner lamination plates, core material with high resistivity properties and a certain distribution of PMs could be applied [25].

3.2.4 Control strategy

Main power losses which appear in the PMSM are copper and iron losses as declared in Section 3.2.3, and different control strategies can be implemented in order to minimize these and hence improve the overall efficiency of the machine. A wide range of different combinations of d- and q-axis currents can be utilized in order to obtain a certain speed and torque operating point. The maximum torque per ampere (MTPA) method is a commonly utilized control strategy which analytically determines the optimal angle β between the d- and q-axis currents in order to achieve the highest possible torque for a given current magnitude, and thereby also minimizing the copper losses. Hence the d- and q-axis currents can be written as

$$i_d = I_s \cos(\beta) \tag{3.19}$$

$$i_q = I_s \sin(\beta) \tag{3.20}$$

where I_s is the stator current magnitude. With known d- and q-axis stator inductances, the MTPA angle can be calculated from [26]

$$\sin(\beta) = -\frac{\Psi_m}{4(L_d - L_q)I_s} - \sqrt{\left(\frac{\Psi_m}{4(L_d - L_q)I_s}\right)^2 + \frac{1}{2}} \tag{3.21}$$

where β is found between 90°-180° in motor operation, and between 180°-270° in generator operation.

3.3 Synchronous Reluctance Machine

The synchronous reluctance machine (SynRM) utilizes the reluctance of the rotor in combination with the revolving magnetic field inside the stator, in order to generate torque. Compared to the PMSM, the rotor of the SynRM does not contain PMs which makes it more robust for withstanding high centrifugal forces and is therefore commonly used in high speed applications. Furthermore, due to the absence of PMs the SynRM is less costly and the risk for demagnetization does not need to be considered [22]. Furthermore, it is less sensitive against high temperatures and hence very robust against high overloads.

In order to generate torque, the rotor is optimally designed to fully utilize the reluctance force. The rotor design can be categorized into three different topologies called salient pole, axially laminated anisotropy and transversely laminated anisotropy. In the axially laminated rotor each barrier are radially stacked towards the shaft, while in a transversely laminated rotor discs of laminate are stacked along the axis of the shaft [27].

3.3.1 Concept of reluctance

The concept of reluctance can be illustrated with the help of a rectangular object with anisotropic magnetic material. If a magnetic field is induced over the object its d-axis wants to be aligned with the magnetic field. Therefore, if there exists an angle difference δ, a torque will be produced in order to align the d-axis with the magnetic field, as shown in Figure 3.5. Torque is generated since the air has higher reluctance compared to the steel material of the object and thus the magnetic field will be highly concentrated in this material and create temporary poles as in a PM. Due to the revolving magnetic field inside the stator, the temporary poles of the rotor will try to follow and consequently the rotor will also rotate.

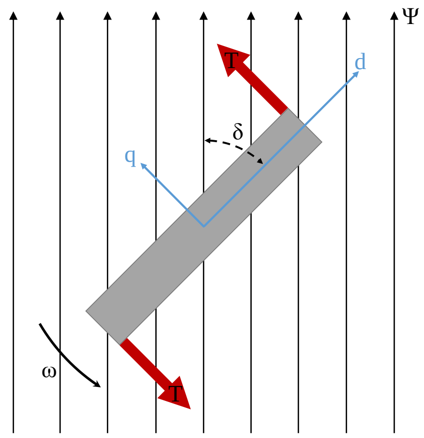

Figure 3.5 An anisotropic material located inside a magnetic field which hence produces a reluctance torque since the d-axis of the material is unaligned with the magnetic field.

3.3.2 Steady state model

The SynRM can be electrically modeled based on dynamic dq-representation, as illustrated in Figure 3.6.

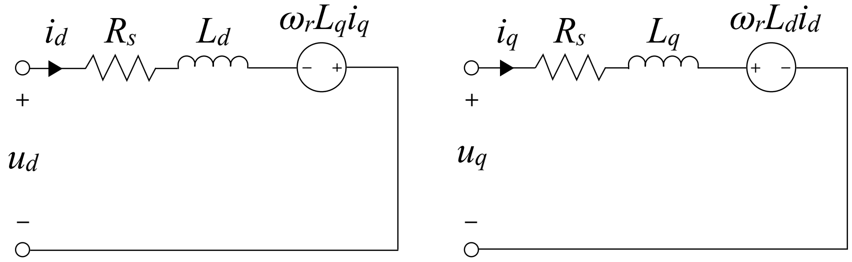

Figure 3.6 SynRM electric model by dynamic dq-representation.

The stator voltage equations can be derived directly from (3.10) and (3.11) by excluding the flux linkage from the PMs in the rotor. Modeled in the dq-plane, they can be written as followed.

$$u_d = R_s i_d + L_d \frac{di_d}{dt} - \omega_r L_q i_q \tag{3.22}$$

$$u_q = R_s i_q + L_q \frac{di_q}{dt} + \omega_r L_d i_d \tag{3.23}$$

Since the electrical system is much faster relative to the mechanical system and therefore has a much smaller time constant, the stator voltage equations can be rewritten as

$$u_d = R_s i_d - \omega_r L_q i_q \tag{3.24}$$

$$u_q = R_s i_q + \omega_r L_d i_d \tag{3.25}$$

where the current time derivative is neglected and thus electrical steady state is achieved. It can be observed that (3.24) is the same as (3.12).

3.3.3 Mechanical output and power losses

The electromechanical torque produced by a SynRM is equal to the reluctance torque produced by a PMSM and can be expressed as in (3.16). It can be concluded that the difference between the d- and q-axis stator winding inductances has a great impact on the torque production. The ratio between L_d and L_q is referred to as the saliency ratio and is defined as

$$\kappa = \frac{L_d}{L_q} \tag{3.26}$$

Due to the cross magnetization between the d- and q-axis stator inductances, the air gap length has a considerable effect on the output torque [28]. A small air gap length results in a high saliency ratio and thus a high output torque.

As for the PMSM the power losses in a SynRM can approximately be categorized as copper losses and iron losses. Copper losses is generally dominant and can be calculated from (3.17). The iron losses depend on induced eddy current and magnetic hysteresis, and will increase with frequency and therefore with the speed of the machine and are expressed as in (3.18).

3.4 Induction Machine

The induction machine (IM) is one of the most commonly used electric machines for industrial applications. They are technically mature, characterized as robust and a cheaper alternative compared to the PMSM. Compared to the PMSM and SynRM, the IM utilizes windings in the rotor in order to interact with the revolving magnetic field. Due to the revolving magnetic field generated from the stator windings, an emf will be induced in the rotor windings and hence also current, and thus the rotor will start to rotate. In other words, current is inducted by magnetic induction, and thereof its name (induction machine). In comparison to many other machines which are using brushes to commute current to the rotor windings, the rotor current in the IM is as described transferred through induction, like in a transformer.

Two commonly used rotor configurations are the squirrel cage rotor and the wound rotor. Due to high costs and short maintenance intervals the latter is less suitable to be utilized in BEVs and HEVs. The squirrel cage rotor are using solid aluminum or copper bars distributed in the rotor and short circuited by two end-rings, which makes this rotor type less costly and highly reliable [22], [29].

3.4.1 Steady state model

The IM can be modeled as a transformer, where the stator side is equivalent to the primary side whereas the rotor side is equivalent with the secondary side. It can be electrically modeled by dynamic dq-representation with amplitude invariant T-form, as shown in Figure 3.7.

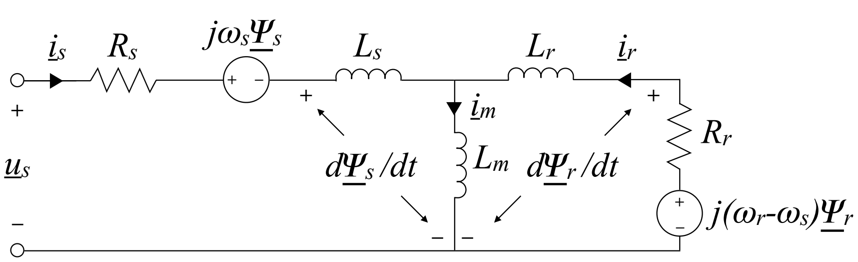

Figure 3.7 IM electric model by dynamic dq-representation with ampitude invariant T-form.

By applying Kirchhoff's voltage law, the stator and rotor voltage equations can be written as

$$\underline{u}_s = R_s \underline{i}_s + \frac{d\underline{\Psi}_s}{dt} + j\omega_s \underline{\Psi}_s \tag{3.27}$$

$$0 = R_r \underline{i}_r + \frac{d\underline{\Psi}_r}{dt} + j(\omega_r - \omega_s)\underline{\Psi}_r \tag{3.28}$$

where R_r is the rotor resistance, $\underline{i}_r$ is the rotor current, ω_s is the synchronous speed of the stator magnetic field, and where $\underline{\Psi}_s$ and $\underline{\Psi}_r$ are stator and rotor flux linkage respectively, and can be expressed as

$$\underline{\Psi}_s = L_s \underline{i}_s + L_m \underline{i}_r \tag{3.29}$$

$$\underline{\Psi}_r = L_r \underline{i}_r + L_m \underline{i}_s \tag{3.30}$$

where L_s is the stator leakage inductance, L_r is the rotor leakage inductance and L_m is the magnetization inductance of the machine. In steady state the flux linkage derivatives are neglected and hence (3.27) and (3.28) can be reformulated as

$$\underline{u}_s = R_s \underline{i}_s + j\omega_s L_s \underline{i}_s + j\omega_s L_m \underline{i}_m \tag{3.31}$$

$$0 = R_r \underline{i}_r + j\omega_s L_r \underline{i}_r + j\omega_s L_m \underline{i}_m - j\omega_r \underline{\Psi}_r \tag{3.32}$$

3.4.2 Mechanical output

Consider a situation where the rotor speed is equal to the speed of the magnetic field of the stator. Since both are rotating at the same speed, the windings in the rotor will not experience a fluctuating magnetic field. Consequently, no emf or current will be induced in the rotor windings and hence the rotor will, due to external or parasitic load torque, gradually slow down. However, when the rotor speed decreases it will start to experience a rotating magnetic field, so emf and current will be induced and the rotor will start to accelerate again. Accordingly, the rotor speed will never be able to rotate at the same speed as the magnetic field, which rotates at synchronous speed N_s. The IM is hence also called asynchronous machine. The speed difference between synchronous speed and rotor speed N_r is known as the slip s, and can be described as

$$s = \frac{N_s - N_r}{N_s} \tag{3.33}$$

where a negative slip is indicating that the machine is operating in generating mode. The electromechanical torque of the IM can be expressed as

$$T_e = \frac{3n_p}{2}(\Psi_{sd} i_{sq} - \Psi_{sq} i_{sd}) \tag{3.34}$$

where Ψ_{sd} and Ψ_{sq} are the d- and q-axis component of the stator flux linkage, respectively.

3.4.3 Power losses

The power losses of the IM can, as for the PMSM and SynRM, be generally categorized into resistive winding losses and iron losses. Since it contains current carrying conductors in both stator and rotor, the resistive losses are generally dominant. In this work, the resistive losses of the IM are denoted P_{cu} even though the rotor windings do not have to consist of copper, and is expressed as

$$P_{cu} = 3(R_s I_{s,rms}^2 + R_r I_{r,rms}^2) \tag{3.35}$$

where R_r is the rotor resistance and $I_{r,rms}$ is the rms current induced in the rotor. The iron losses depends on the hysteresis and eddy currents in the stator and rotor material, and will increase with the frequency of the machine and can also be calculated from (3.18).

3.5 Thermal modeling

Heat transfer in electric machines needs to be considered during the design in order to prevent overheating at high loads. Otherwise, serious damages can emerge, such as deterioration of winding insulation and demagnetization of PMs, which can culminate into immediate machine failures. Heat transfer occurs whenever a temperature difference exist between media or in a medium, and it can be categorized in three different modes called conduction, convection and thermal radiation [30]. In order to predict how the temperature inside an electric machine varies, a lumped-parameter thermal network can be utilized. This kind of network gives a reasonable estimate of the temperature distribution between the different components inside a machine, even with only a few nodes present [31].

3.5.1 Modes of heat transfer

Conduction can be seen as transfer of energy between higher energetic particles and lower energetic particles in substances such as solids, fluids or gases [30]. When these particles collide, energy is transferred to the less energetic particle and the thermal energy is spread out from the heat source. In an electric machine the heat conduction occurs between the solid parts of the machine, where the conductive heat transfer rate (W) can be described as

$$q_{cond} = -\lambda A \frac{\Delta T}{L} \tag{3.36}$$

where λ is the thermal conductivity of the material (W/mK), A is the cross sectional area perpendicular to the heat transfer (m^2), ΔT is the temperature difference (K) and L is the heat transfer distance (m).

Convection heat transfer occurs between a surface and a moving fluid or a gas and involves both contribution of random molecular motion and heat transfer by the moving fluid [30]. There exist two types of convection, called forced convection and natural convection. Forced convection occurs when a fluid or a gas is forced to move by an application such as a fan or a pump, while natural convection occurs naturally when air is heated and becomes lighter than the cold air and are subject to a buoyancy force which induces a vertical motion. Convection heat transfer can expressed as

$$q_{conv} = \alpha A(T_{surface} - T_{fluid}) \tag{3.37}$$

where α is the convection heat transfer coefficient, while $T_{surface}$ and T_{fluid} are the surface and fluid temperature respectively. In electric machines natural convection occurs e.g. between the frame and the surrounding ambient, while forced convection can be utilized to further improve the heat transfer with e.g. a shaft mounted fan. For machines with a need for even higher heat dissipation, liquid cooling with water or oil mixture can be utilized.

Thermal radiation is emitted by materials such as solids, liquids or gases with non zero temperature. For conduction and convection heat transfer a medium is needed to transfer the heat, while for thermal radiation heat is propagated by electromagnetic waves or photons, and is most efficient in vacuum. Thermal radiation heat transfer can be mathematically described as

$$q_{rad} = \epsilon\sigma A(T_{surface}^4 - T_{surr}^4) \tag{3.38}$$

where ϵ is the surface emissivity, σ is Stefan Boltzmann's constant, and $T_{surface}$ and T_{surr} are the surface and surrounding temperature respectively. Similar to (3.37), the thermal radiation heat transfer coefficient can be expressed as

$$q_{rad} = \alpha_{rad} A(T_{surface} - T_{surr}) \tag{3.39}$$

where the heat transfer coefficient of thermal radiation is

$$\alpha_{rad} = \epsilon\sigma A(T_{surface} - T_{surr})(T_{surface}^2 - T_{surr}^2) \tag{3.40}$$

3.5.2 Lumped-parameter network modeling

In order to design a lumped-parameter network, the different regions of the machine are lumped together with respect to material properties, thermal storage capacities, heat regeneration, and temperatures [25]. The lumped regions are then connected in a network using thermal impedances which are determined mainly by geometrical and material properties. The lumped-parameter network is then corresponding to an electrical network, where the temperature represents the voltage and the heat transfer is equivalent to the current. The temperature difference between two neighboring nodes, T_i and T_j, can in steady state be expressed as

$$T_i - T_j = \mathbf{G}^{-1}\mathbf{P} \tag{3.41}$$

where $\mathbf{P}$ is a vector that contains the electric machine losses for respective nodes, as in

$$\mathbf{P} = \begin{bmatrix} P_1 \\ P_2 \\ \vdots \\ P_n \end{bmatrix} \tag{3.42}$$

and $\mathbf{G}$ is the thermal conductance matrix in a n-node system defined as

$$\mathbf{G} = \begin{bmatrix} \sum_{i=1}^{n} \frac{1}{R_{1,i}} & -\frac{1}{R_{1,2}} & \cdots & -\frac{1}{R_{1,n}} \\ -\frac{1}{R_{2,1}} & \sum_{i=1}^{n} \frac{1}{R_{2,i}} & \cdots & -\frac{1}{R_{2,n}} \\ \vdots & \vdots & \ddots & \vdots \\ -\frac{1}{R_{n,1}} & -\frac{1}{R_{n,2}} & \cdots & \sum_{i=1}^{n} \frac{1}{R_{n,i}} \end{bmatrix} \tag{3.43}$$

In the same way as an electrical resistance is related to the conduction of electricity, the net thermal resistance R_{th} is associated with the conduction of heat. The thermal resistance for conduction in a region with differences in temperature can be written as

$$R_{th} = \frac{1}{G} = \frac{\Delta T}{q_{cond}} = \frac{l}{\lambda A} \tag{3.44}$$

In electric machines there exists parts which take the shape of a hollow cylinder or a segment of it. Radial heat transfer for this kind of geometry is mathematically derived as

$$R_{th} = \frac{ln(\frac{r_{out}}{r_{in}})}{\phi \lambda l_{thick}} \tag{3.45}$$

where r_{out} and r_{in} are the outer and inner radius of the hollow cylinder, ϕ is the segment angle (rad) and l_{thick} is the thickness of the segment.

The thermal resistance for axial heat transfer for the same type of geometry can be described as

$$R_{th} = \frac{l_{thick}}{\lambda \pi (r_{out}^2 - r_{in}^2)} \tag{3.46}$$

For convection heat transfer the thermal resistance can be written as

$$R_{th} = \frac{T_{surface} - T_{fluid}}{q_{conv}} = \frac{1}{\alpha A} \tag{3.47}$$

The heat radiation exchange between a surface and its surrounding is generally small and is defined as [30]

$$R_{th} = \frac{T_{surface} - T_{surr}}{q_{rad}} = \frac{1}{\alpha_{rad} A} \tag{3.48}$$

To be able to estimate the heat storage in different machine regions thermal capacitances are utilized. A thermal capacitance is defined by the material density ρ, the volume V and the specific heat c_p, as in

$$C_{th} = \sum_{i=1}^{n} \rho_i V_i c_{p,i} \tag{3.49}$$

Similar to the conductance matrix, a capacitance matrix can be arranged as

$$\mathbf{C} = \begin{bmatrix} C_{th,1} & 0 & \dots & 0 \\ 0 & C_{th,2} & \dots & 0 \\ \vdots & \vdots & \ddots & \vdots \\ 0 & 0 & \dots & C_{th,n} \end{bmatrix} \tag{3.50}$$

The change of temperature in a node can then be calculated as

$$\frac{d\mathbf{T}}{dt} = \mathbf{C}^{-1}(\mathbf{P} - \mathbf{GT}) \tag{3.51}$$

4

Case Setup

The development of electric machines has progressively generated advanced designs and machine constructions. Complex iron geometries cause the electromagnetic properties to alter with regard to the geometry appearances, which makes it impractical to sufficiently evaluate and model machines by analytical methods. Hence finite element methods (FEM) are utilized in order to analyze the electromagnetic properties and evaluate the performance, and has thus become the standard method when modeling electric machines.

When conducting FEM analyses it is essential to provide suitable simulation setups. Therefore, following chapter specifies quantitative operating points and performance requirements of which the selected electric machines should fulfill in order to be regarded as adequate for the mild hybrid application. In addition to this, operating limits which have been used as basis for the work are further specified. Moreover, elementary optimization processes and applied simulation setups for all investigated machines are presented in the following chapter.

4.1 Operating points of interest

In comparative studies of electric machines it is of great importance to clearly specify what kind of operating points and target parameters that are in focus of the study. In this work, the machines are operating in a mild hybrid drivetrain configuration and should thus be able to withstand conditions which are expected for such an application in order to be classified as adequate.

One of the most essential operating points of electric machines in HEVs is to crank the ICE when it is at rest. In order to overpower the substantial resistance of the kinematic mechanism, which is at its peak during cold climate conditions, the minimum output torque requirement which needs to be provided was assumed to be 55 Nm when when operating at low speed levels.

Regardless of how the electric machine is operating, it should always possess the ability to generate sufficient power to attain power balance in the system. Worst case scenario occurs during cold climate conditions when e.g. electric fan, heating system and other high power loads need to be running and supplied with power. Hence the output power needs to be evaluated at idle speed of the ICE (750 rpm) and high electric load (2.5 kW). Assuming that the transmission ratio is 1:2.7, the idle speed of the ICE corresponds to a speed of 2000 rpm for the electric machine. It was furthermore assumed that the ICE has a maximum speed of 6800 rpm, which hence results in a maximum speed of 20000 rpm for the electric machine.

From several driving cycles with mild hybrid systems it can be concluded that one of the most frequent operating point for the electric machine occurs at speeds around 4600 rpm and at loads of 1 kW [32]. Operating regions with high overall efficiency varies significantly depending on machine topology and design, and one could argue that a machine with high efficiency in the most frequent operating region is more beneficial than others. Therefore, the machine efficiency at 4600 rpm and 1 kW was chosen to be evaluated.

To conclude, the operating points of interest for the study are:

- Maximum output torque at low speed levels
- Maximum output power at 2000 rpm
- Efficiency at 4600 rpm and 1 kW.

4.2 Machine scaling

The amount of space available in today's vehicles for the electric machine is strictly limited. For this study, a total cylindrical space of 200 mm axial length and 185 mm outer diameter was assumed to be disposable, which includes the power inverter and cooling unit. Assuming that the geometrical requirement for the inverter is 60 mm, cooling unit is 10 mm and the stator end windings at respective side requires maximum 30 mm, consequently results in an electric machine with 80 mm stack length and 165 mm stator outer diameter.

The stator winding resistance consists of one active part representing the active stack length l_{active}, and one passive part representing the winding overhang $l_{passive}$. Electric machines with low length and high diameter ratio will thus have dominant resistive losses in the end windings and limited output torque, since primarily the active length of the machine contributes to the torque production. The active length is scaled within the limits of the geometrical constraints according to [33]

$$l_{av} = l_{active} + l_{passive} = l_{stk} + 1.2\tau_p + 2d_{ext} \tag{4.1}$$

where l_{av} is the average conductor length of a half turn, l_{stk} is the active stack length (80 mm), τ_p is the winding pole pitch and is calculated by $\frac{\pi D}{2n_p}$, where D is the stator inner diameter and n_p is the number of pole pairs in the machine. Furthermore, $2d_{ext}$ is the axially winding overhang and is assumed to be 50 mm [33].

4.3 Operating limits

The maximum applied DC voltage U_{DC} during motoring mode is set to 48 V. By applying third harmonic injection, the DC voltage is utilized to a higher extent by adding a zero-sequence to the electric machine in which the neutral point will alter up and down [34]. By this floating neutral point, the added zero-sequence waveforms are cancelled out and the maximum output voltage is increased without increasing the DC voltage. The output rms magnitude of the AC phase voltage $U_{ph,rms}$ can then be calculated by

$$U_{ph,rms} = m_a \frac{U_{DC}}{\sqrt{2}\sqrt{3}} \tag{4.2}$$

where a modulation index m_a of 0.9 is used in order to ensure controllability of the current. This sets the output limit of the AC phase voltage in relation to the applied DC voltage.

Initially, the maximum rms magnitude of the phase current density $J_{rms,max}$ is set to 20 A/mm^2. The maximum rms magnitude of the phase current $I_{ph,rms,max}$ flowing in each winding of the machine is then calculated from [25]

$$I_{ph,rms,max} = \frac{J_{rms,max} k_{ff} A_{slot} n_{pb}}{n_{wl} n_{wt}} \tag{4.3}$$

where k_{ff} is the stator slot fill factor, A_{slot} is the area of a single slot, n_{pb} is the number of parallel branches, n_{wl} is the number of winding layers and n_{wt} is the number of winding turns.

4.4 Optimization of PMSM model

The PMSM utilized in this work is a scalable model based on the Toyota Prius 2004 machine with 48 stator slots, containing distributed double layered 3-phase copper windings, 4 parallel branches and 8 poles [35]. However, it has thinner stator yoke and teeth and a different angle for the interior mounted PMs. The winding fill factor in the stator slot area is set to 45 %, which is within the boundaries used for fill factor determination in industrial IMs [36]. In Table 4.1, this machine setup is referred as Model A.

In order to achieve an adequate PMSM, some design parameters were modified and impacts on the performance analyzed. One could argue that 48 stator slots are excessive for a machine with such limited geometrical dimensions, and thus a PMSM was designed containing 24 stator slots with wider slot width, single layer windings and constant fill factor of 45 %. Wider slots with equal fill factor results in larger winding area and hence less current density for a given current magnitude which gives lower copper losses. The number of winding turns is adjusted in order to achieve a nominal speed between 7000-8000 rpm. Furthermore, the slot opening width is kept constant and hence lower torque ripple can be achieved. This machine setup is referred to as Model B in Table 4.1.

The rotor in PMSMs can suffer from adverse stress at high rotational speeds due to intense centrifugal force from the interior PMs. In order to avoid such severe impacts, the PMs were arranged, as illustrated in Figure 4.1, twice the distance further in from the rotor outer radius and half the distance further away from its neighbouring magnet pole. Consequently, less torque ripple and a higher nominal speed can be obtained, but also a minor reduction in maximum output torque. In Table 4.1, this machine setup is referred to as Model C.

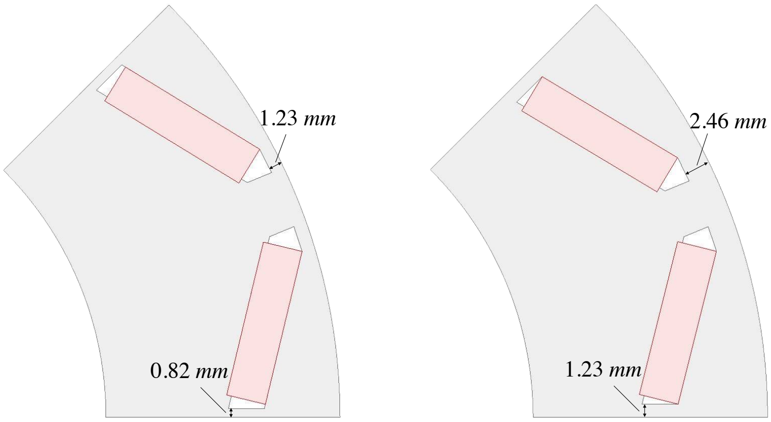

(a) Model A-B. (b) Model C.

Figure 4.1 Arrangement of rotor PMs, where for Model C the PMs are located closer to the centre point of the machine in order to improve the robustness.

Due to the limited machine dimensions, a PMSM with 4 poles was designed with equivalent PM volume as the 8-pole PMSM. The 4-pole PMSM is referred as Model D in Table 4.1, where a summary of machine parameters as well as performance data for the four investigated PMSM models are presented.

Table 4.1 Summary of machine parameters and performance data for the modeled PMSMs.

	Model A	**Model B**	**Model C**	**Model D**
Number of stator slots	48	24	24	24
Number of poles	8	8	8	4
Number of parallel branches	4	4	4	2
Number of winding layers	2	1	1	1
Number of winding turns	1	3	3	2
Slot wedge width (mm)	3.28	6.56	6.56	9.02
Slot bottom width (mm)	4.92	9.84	9.84	10.52
Distance between PMs and rotor radius (mm)	1.23	1.23	2.46	2.77
Distance to neighbouring magnet pole (mm)	0.82	0.82	1.23	2.50
Magnet thickness (mm)	3.73	3.73	3.73	3.73
Magnet width (mm)	29.52	29.52	29.52	59.04
Nominal speed (rpm)	6000	7600	7800	7400
Peak power (kW)	60	62	54	38
Maximum torque (Nm)	84.3	68.9	60.5	52.5
Torque ripple ($\%$)	9	22	14	17
$J_{rms,max}$ (A/mm^2)	20	15	15	20
$I_{ph,rms,max}$ (kA)	1.224	1.253	1.253	1.235

The 8-pole PMSM with 24 stator slots and modified PM position (Model C) fulfill the minimum torque requirement, has a nominal speed in the desired speed range and acceptable torque ripple. Hence it was considered as the most suitable option and selected to be further analyzed. Even though the 4-pole PMSM (Model D) does not fulfill the minimum torque requirement, it was likewise chosen to be further analyzed since the additional machine topologies in this work are expected to have these number of poles.

4.5 Simulation setup

All machine topologies in this work are modeled in 2D and simulated with FEM in the electromagnetic field software Ansys Maxwell. Each machine is swept in the speed range of 1-20000 rpm with steps of 500 rpm, and at each speed step a torque sweep is conducted from zero to the maximum torque which can be provided at current speed. Every speed and torque combination is evaluated by FEM in 121 operating points in the dq-current plane with 81 samples during two electrical periods, where data is extracted from the second period only in order to obtain correct iron losses. By assuming that the inductances are speed independent, they are extracted for all current magnitudes from zero to maximum torque at 1000 rpm. Through interpolation from the operating points, a torque map in the dq-current plane is created from which the MTPA and field weakening region operating points are numerically found. The procedure is performed for both motoring and generating mode.

The approach of simulating the IM differs in contrast to the synchronous machines, due to the slip which adds an extra dimension to the simulations. Additionally, the time for reaching steady state is longer which requires more electric periods. The rotor speed is swept in a speed range of 1000-9000 rpm with steps of 500 rpm, where the electrical supply frequency is varied in order to evaluate the slip in each operating point. By evaluating the stall torque at maximum current, the maximum torque of the machine was found, along with the nominal speed point. In addition, the slip values required for stall operation in each speed level are studied to evaluate the impact on the slip for different speeds. The machine is swept in the torque range between zero and maximum torque in nominal speed in order to evaluate the slip for maximum efficiency for each operating torque. By extrapolating the stall torque slip with the maximum efficiency slip, a matrix of optimal slip for each operating point prior to the nominal speed is generated.

Data such as total copper and iron losses as well as losses in the different machine parts such as the stator teeth and yoke, active and end windings, rotor, PMs and bearings are extracted from the simulations. Since the resistance of the end windings are not taken into consideration in Ansys Maxwell, they are subsequently added in order to obtain accurate estimations of the copper losses. For simplicity, parasitic leakage inductances in the end windings are ignored in this work. With known losses, parameters such as output power and machine efficiency are mapped as a function of torque and speed.

4.5.1 PMSM

Machine data for the 8- and 4-pole PMSM can be found in Table 4.2. By aligning the d-axis of the machines with the centre of the positive A-phase pole at the initial simulation time step, maximum flux linkage is achieved.

Table 4.2 Summary of machine data for the simulated PMSMs.

	PMSM 8-pole	**PMSM 4-pole**
Nominal speed	7800 rpm	7400 rpm
Peak power	54 kW	38 kW
Maximum torque	60.5 Nm	52.4 Nm
$J_{rms,max}$	15 A/mm^2	20 A/mm^2
$I_{ph,rms,max}$	1.253 kA	1.235 kA
Number of stator slots	24	24
Number of parallel branches	4	2
Number of winding layers	1	1
Number of winding turns	3	2
l_{active}	80 mm	80 mm
$l_{passive}$	102.2 mm	154.3 mm
Stator outer diameter	164 mm	164 mm
Stator inner diameter	110.7 mm	110.7 mm
Stator yoke thickness	9.33 mm	11.79 mm
Slot wedge width	6.56 mm	9.02 mm
Slot bottom width	9.84 mm	10.52 mm
Slot area	137.26 mm^2	137.26 mm^2
Winding cross-section area	61.77 mm^2	61.77 mm^2
Fill factor	45 %	45 %
Tooth width	8.5 mm	7.3 mm
Tooth height	16.4 mm	13.9 mm
Slot opening width	1.64 mm	1.64 mm
Air gap length	0.615 mm	0.615 mm
Rotor outer diameter	109.47 mm	109.47 mm
Rotor inner diameter	65.6 mm	65.6 mm
Magnet thickness	3.73 mm	3.73 mm
Magnet width	29.52 mm	59.04 mm
Iron material	NO30	NO30
Magnet material	NMX-37F	NMX-37F

Machine geometries with mesh densities for the simulation setup along with interpolated torque bounded by the operating points in the dq-plane and the trajectory of the MTPA line resulted from the current control algorithm are presented in Figure 4.2 and 4.3 for the 8- and 4-pole PMSMs, respectively. Due to the influence from the PMs, torque can be provided even though the d-axis current is zero.

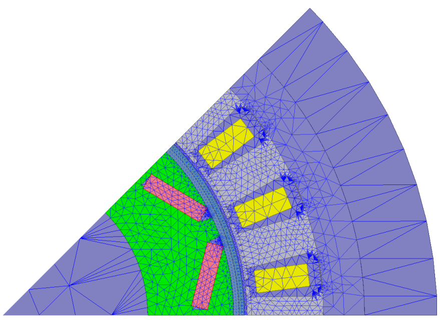

(a) Machine geometry.

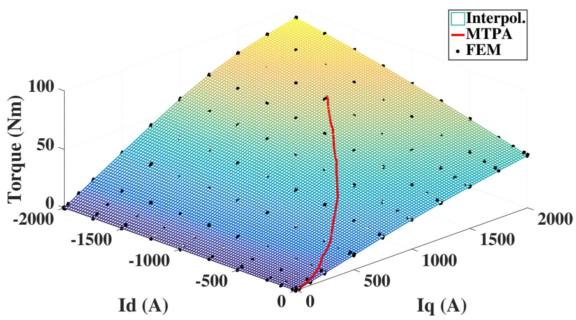

(b) MTPA result.

Figure 4.2 Machine geometry with mesh density used for FEM simulations, and interpolated torque in the dq-plane with operating points and MTPA line, for the 8-pole PMSM.

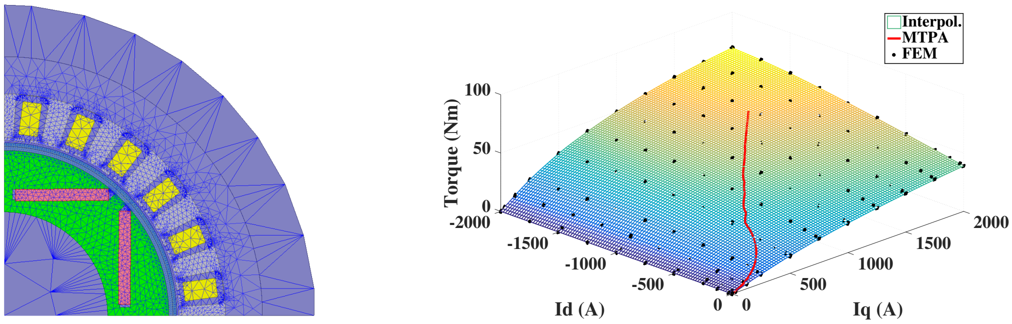

(a) Machine geometry. (b) MTPA result.

Figure 4.3 Machine geometry with mesh density used for FEM simulations, and interpolated torque in the dq-plane with operating points and MTPA line, for the 4-pole PMSM.

The trajectory of the MTPA algorithm follows the current combination which generates most torque for a given current magnitude by operating at optimal current angle. This is however only valid in the constant torque region and bounded by a current limit circle. When the machine reaches nominal speed, the maximum voltage limit is hit and hence the criteria to not exceed the voltage limit in the constant power region needs to be considered. Thus the MTPA algorithm trajectory drops down in order to follow the voltage ellipse trajectories for speed levels above nominal speed. This is shown in Figure 4.4 and 4.5 for the 8- and 4-pole PMSMs respectively, where d- and q-current values for all torque levels, resulted from the MTPA algorithm, are presented.

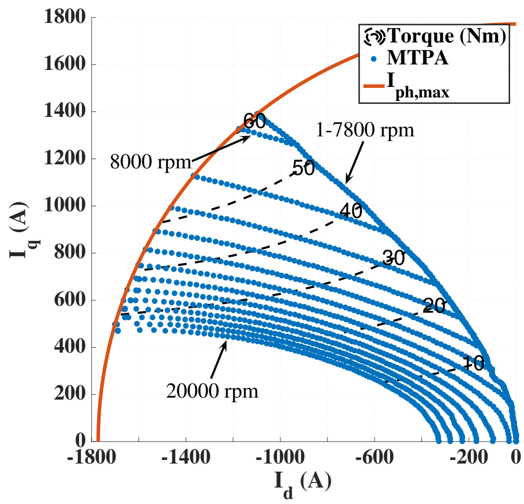

Figure 4.4 Results from the MTPA algorithm which shows d- and q-current values for the torque levels available from zero to maximum speed, for the 8-pole PMSM.

Figure 4.4 shows that the 8-pole PMSM can provide maximum phase current at all speed levels and thus it can be expected that the machine should have the ability to generate maximum output power in the whole speed range. This is however not valid for the 4-pole PMSM, where its MTPA trajectory presented in Figure 4.5 gives an indication of that for speed levels above 9000 rpm maximum phase current cannot be provided since the MTPA curve does not reach the current limit circle. The reason is that the impedance becomes too big since it increases proportionally with the frequency and hence the speed of the machine. It is thus not possible to provide more current with a maximum voltage magnitude of 48 V, when the impedance becomes too big for speed levels above nominal speed.

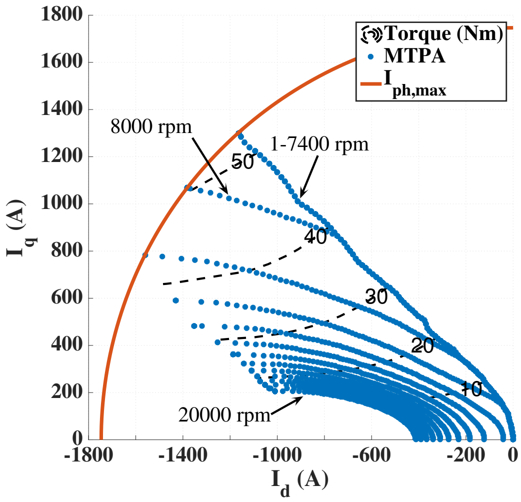

Figure 4.5 Results from the MTPA algorithm which shows d- and q-current values for the torque levels available from zero to maximum speed, for the 4-pole PMSM.

4.5.2 SynRM

Machine data for the SynRM utilized in this work can be found in Table 4.3. By aligning the q-axis of the machine with the centre of the positive A-phase pole at the initial simulation time step, maximum flux linkage is achieved. Equivalent stator design has been utilized as for the stator of the 4-pole PMSM. However, the stator yoke region is thicker in order to avoid saturation, which consequently gives smaller stator teeth for equal slot size. Furthermore, the air gap length is decreased in order to achieve a high torque output.

Table 4.3 Summary of machine data for the simulated SynRM.

	SynRM
Nominal speed	7000 rpm
Peak power	29 kW
Maximum torque	44.8 Nm
$J_{rms,max}$	20 A/mm^2
$I_{ph,rms,max}$	1.235 kA
Number of poles	4
Number of stator slots	24
Number of parallel branches	2
Number of winding layers	1
Number of winding turns	2
l_{active}	80 mm
$l_{passive}$	149.6 mm
Stator outer diameter	164 mm
Stator inner diameter	105.27 mm
Stator yoke thickness	14.51 mm
Slot wedge width	9.02 mm
Slot bottom width	10.52 mm
Slot area	137.26 mm^2
Winding cross-section area	61.77 mm^2
Fill factor	45 %
Tooth width	6.6 mm
Tooth height	13.94 mm
Slot opening width	1.64 mm
Air gap length	0.4 mm
Rotor outer diameter	104.47 mm
Rotor inner diameter	20 mm
Number of barriers	3
Iron material	NO30

Figure 4.6 presents the SynRM geometry with mesh density for the simulation setup, along with interpolated torque bounded by the operating points in the dq-plane, as well as the trajectory of the MTPA line resulting from the current control algorithm. Since torque can only be provided by the influence from reluctance, the interpolated torque goes to zero whenever the d- or q-axis currents go to zero.

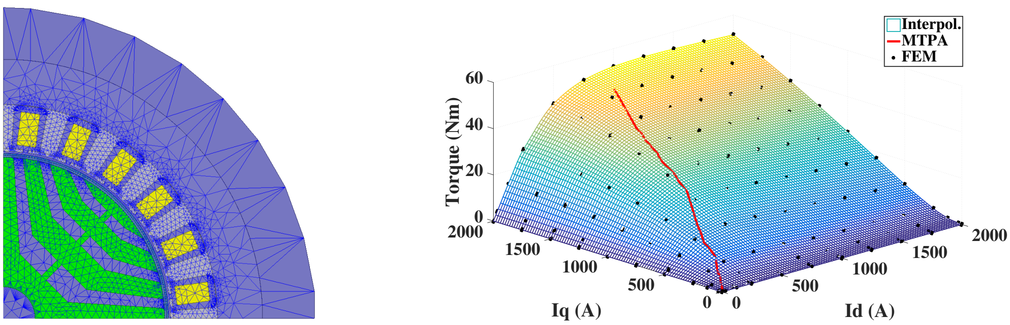

(a) Machine geometry.　(b) MTPA result.

Figure 4.6 Machine geometry with mesh density used for FEM simulations, and interpolated torque in the dq-plane with operating points and MTPA line, for the SynRM.

The results from the MTPA algorithm in Figure 4.7 indicates that for speed levels above 8000 rpm, the SynRM will not be able to provide maximum output power, since the MTPA curves does not reach the current limit circle. The MTPA line shifts into the region where the q-axis current is larger than the d-axis current, which means that the torque production is mainly generated from the q-axis current.

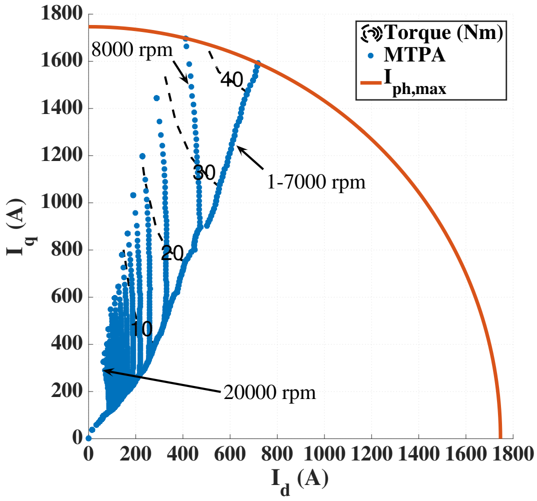

Figure 4.7 Results from the MTPA algorithm which shows d- and q-current values for the torque levels available from zero to maximum speed, for the SynRM.

4.5.3 PMSynRM

To improve the overall performance of the SynRM, PMs are implemented in the rotor barriers. The specific machine is hence defined as a PM-assisted synchronous reluctance machine (PMSynRM). Machine performance data can be found in Table 4.4. It has equal stator and rotor dimensions as the SynRM.

In general, rare-earth magnets are often utilized in PMSMs due to their superior energy density and beneficial ability to generate significantly high performance characteristics. In addition to the automotive sector, they are adopted in a broad range of commercial applications such as electronic devices and new energy technologies such as wind turbines, which might consume more magnet material than the automotive if the trend of using PMSMs persists. Due to the rapidly growing sectors where rare-earth magnets are desired, their demand worldwide are expected to increase [37]. Such magnets are made of rare-earth materials, such as Dysprosium for preventing irreversible demagnetization, which makes them very expensive [38]. Moreover, there exists some concerns regarding the stability of future supplies of rare-earth materials [39].

With the disadvantageous circumstances related to rare-earth magnets taken into consideration, one could possibly argue that the quantities of rare-earth material used in commercial applications need to be reduced in order to not provoke the demand even further. For the PMSynRM, it is therefore chosen to use ferrite magnets as a substitute for the rare-earth magnets. Ferrite magnets do not posses the same superior energy density as rare-earth magnets, but are still commonly used in commercial applications due to their low cost and high productivity, and are often a compound of iron oxide and barium or strontium carbonate. For the PMSynRM, the ferrite magnet Y30-BH is chosen to be utilized.

Table 4.4 Summary of machine data for the simulated PMSynRM.

	PMSynRM
Nominal speed	7100 rpm
Peak power	35 kW
Maximum torque	51.8 Nm
$J_{rms,max}$	20 A/mm^2
$I_{ph,rms,max}$	1.235 kA
Ferrite magnet material	Y30-BH

PMSynRM geometry with mesh density for the simulation setup along with interpolated torque bounded by the operating points in the dq-plane and the trajectory of the MTPA line resulted from the current control algorithm are presented in Figure 4.8. Compared to the MTPA result for the SynRM in Figure 4.6 (b), it can be seen in Figure 4.8 (b) that the PMSynRM has torque production from the PMs since the interpolated torque is not zero even though the d-axis current goes to zero. It is though not as substantial as for the PMSMs with rare-earth magnets.

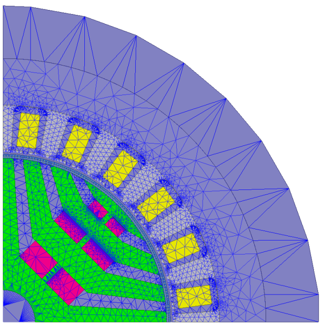

(a) Machine geometry.

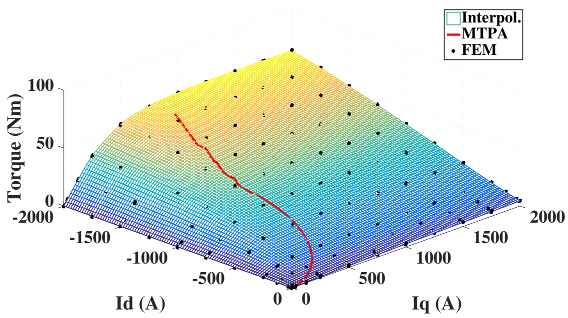

(b) MTPA result.

Figure 4.8 Machine geometry with mesh density used for FEM simulations, and interpolated torque in the dq-plane with operating points and MTPA line, for the PMSynRM.

Figure 4.9 presents the results from the MTPA algorithm for the PMSynRM. As for the SynRM, the machine will not be able to provide maximum output power for speed levels above 8000 rpm, since the MTPA curve does not intersect current limit circle.

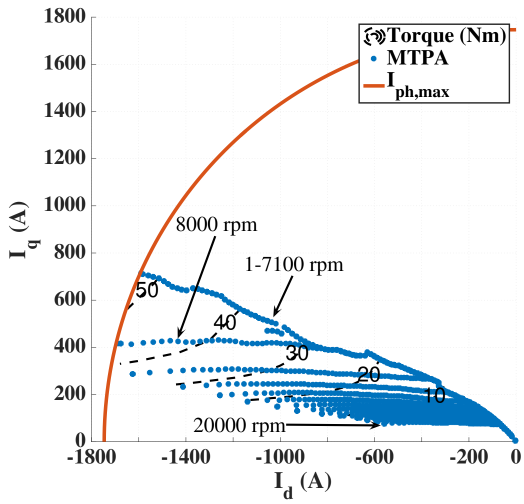

Figure 4.9 Results from the MTPA algorithm which shows d- and q-current values for the torque levels available from zero to maximum speed, for the PMSynRM.

4.5.4 IM

The IM has the same stator design as the SynRM and PMSynRM, in order to avoid saturation in the yoke region. The rotor of an IM can be designed in various of combinations. In this work, an IM with 32 rotor bars has been used as starting reference [40]. The design of the rotor bars is optimized through simulation sweeps in order to reduce the rotor resistance and leakage of the IM and hence increasing the performance. Additionally, aluminum bars is used in the rotor instead of copper bars, in order to represent a less costly standardized IM [11].

Figure 4.10 illustrates the geometry of a rotor bar. The geometry parameters are swept in order to find the optimal design. Initially, the ratio between b_1 and b_2 is kept constant and the sweep of this parameter is presented in Figure 4.11 (a). Secondly, the sweep of the slot height h_1 is conducted and the results are shown in Figure 4.11 (b). The width of parameter b_1 is chosen for which the highest torque was generated. The width of parameter b_2 is swept while and the results are shown in Figure 4.11 (c). Lastly, a sweep of the the bar opening width b_0 is conducted and its results are shown in Figure 4.11 (d). The slip is been optimized for each individual parameter sweep in order to achieve maximum torque. To reach steady state, the simulations required 12 electrical periods.

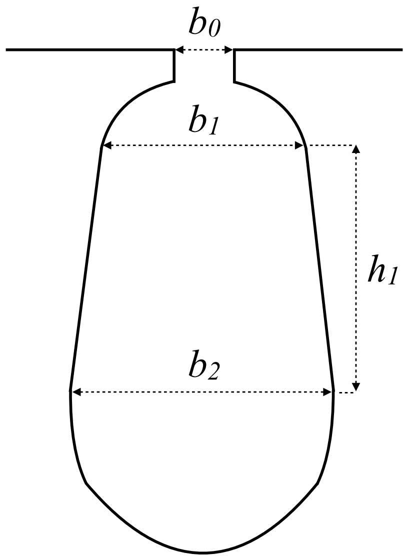

Figure 4.10 Rotor slot geometry.

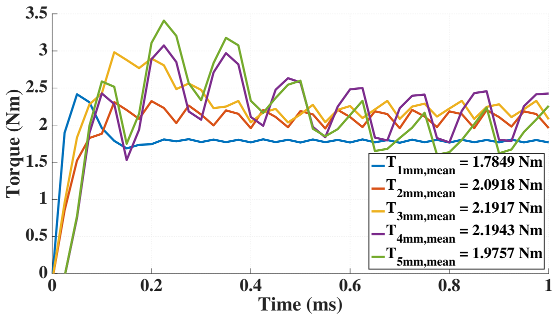

(a) Sweep of $b_1 = b_2$.

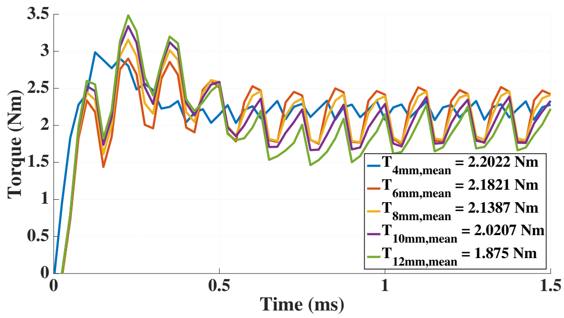

(b) Sweep of h_1.

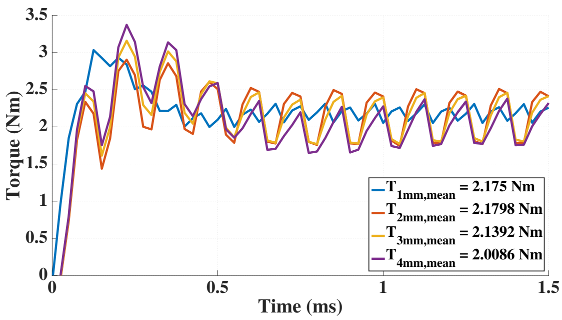

(c) Sweep of b_2.

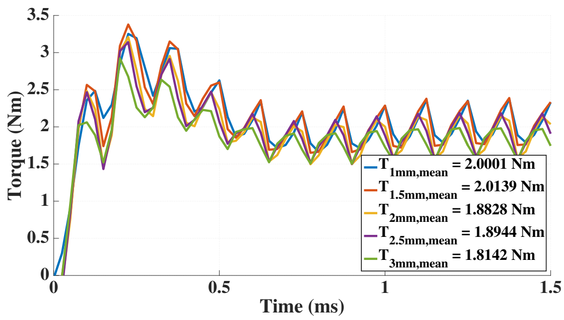

(d) Sweep of b_0.

Figure 4.11 Parameter sweep of IM rotor slots, at rms current magnitude of 100 A and synchronous speed of 3000 rpm.

The final IM geometry with mesh density for the simulation setup is shown in Figure 4.12. Data for rotor design and other machine performance are presented in Table 4.5. The stator geometry is equal to the SynRM and PMSynRM, and can hence be seen in Table 4.3.

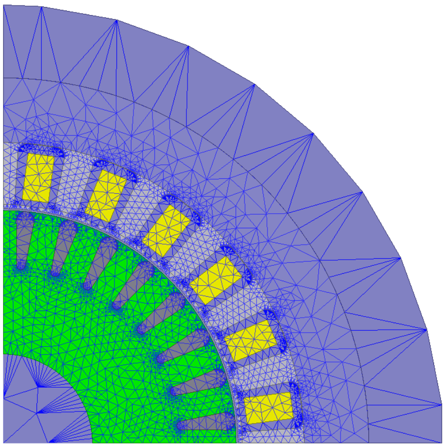

Figure 4.12 IM geometry with mesh density used for FEM simulations.

Table 4.5 Summary of machine data for the simulated IM.

	IM
Nominal speed	8500 rpm
Peak power	50 kW
Maximum torque	65 Nm
$J_{rms,max}$	20 A/mm^2
$I_{ph,rms,max}$	1.235 kA
Rotor outer diameter	104.47 mm
Rotor inner diameter	40 mm
Number of rotor bars	32
b_0	1.5 mm
b_1	4 mm
b_2	2 mm
h_1	10 mm
Iron material	NO30

5

Analysis of Performance and Vehicle Simulations

In this chapter, the results from the FEM simulations are presented and evaluated for respective machine topology. Efficiency maps for whole operating regions are analyzed, as well as corresponding power losses. A comparative assessment is presented, where machine performance is quantified for the operating points of interest. Moreover, the operating performance is related to machine mass and raw material costs, as well as CO_2 impacts from material production. Finally, performance numbers are implemented in full vehicle simulations in order to evaluate the machine as a part of a mild hybrid system.

5.1 Analysis of efficiency and losses

Efficiency maps in motoring and generation mode for the whole operating region are presented in Figure 5.1 and 5.2, for the 8-pole PMSM. Power losses include copper losses in stator windings, iron losses in stator and rotor lamination, PM losses and friction losses in bearings. Iron losses consist of eddy current and hysteresis losses.

The efficiency maps show the operating region where the highest efficiency is located. For the 8-pole PMSM, the highest efficiency is 96.9 % and is located between 12000-15000 rpm and between 20-30 Nm. However, a machine efficiency of 96 % covers mostly the whole operating region after nominal speed of 7800 rpm, i.e. in the field weakening region. In the constant torque region, the machine can provide a peak torque of 60.5 Nm. After nominal speed, the output torque declines until maximum speed point where it stops around 26 Nm.

The characteristics of the efficiency map in generation mode reflects the characteristics in motoring mode. However, the highest efficiency point is higher (97 %) and it covers a wider operating area in the field weakening region. This is due to that the magnetic flux in the air gap is higher during generation mode, which decreases the required current for the machine to provide a certain torque compared to in motoring mode. However, higher magnetic flux increases the iron losses in the machine, but the copper losses are substantially lowered due to less required current and thus the total power losses are reduced.

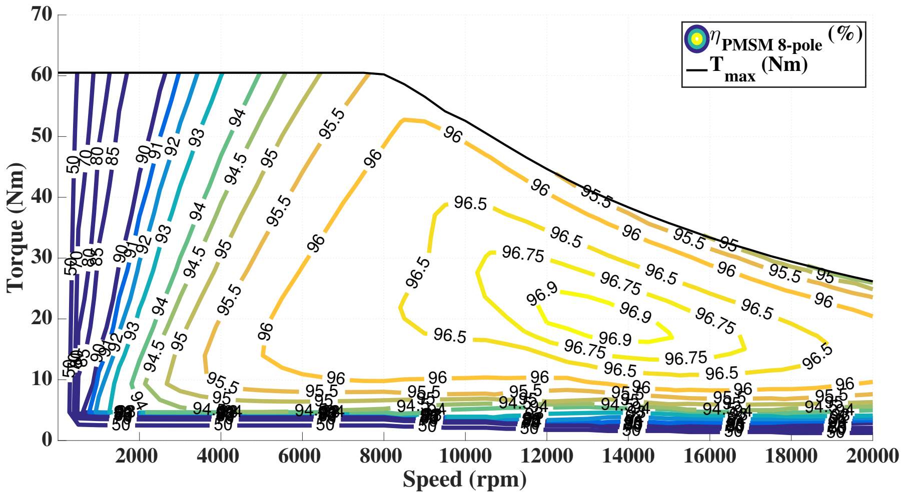

Figure 5.1 Efficiency map in motoring mode as a function of torque and speed, for the 8-pole PMSM.

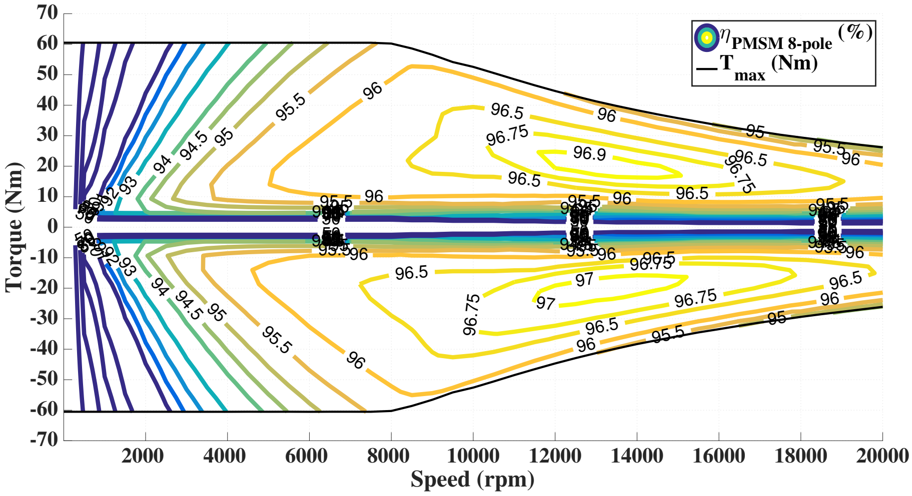

Figure 5.2 Efficiency map in motoring and generation mode as a function of torque and speed, for the 8-pole PMSM.

Mechanical output power as well as power losses for the whole operating region are presented in Figure 5.2, for the 8-pole PMSM. Copper and iron losses dominates and hence losses in PMs and bearings are not presented in the following section. In constant torque operating region, the output power increase linearly until it hits the voltage limit at nominal speed. The machine can provide a peak output power of 54 kW in the whole field weakening region, which is in line with the results from the MTPA algorithm presented in Figure 4.4. It has thus an ideally flat constant power characteristic above nominal speed range.

Since the copper losses are dependent on the square of the current magnitude, they are highly torque dependent which can be seen Figure 5.3 (c). Below nominal speed, there exists no speed dependence but only torque dependence. Above nominal speed, more current is required in order to reduce the magnetic flux linkage, and therefore the copper losses increase for lower torque levels in this operating region.

Iron losses are strongly speed dependent and fairly torque dependent, especially close to maximum speed. They are though somewhat lower than the copper losses, and for this reason the characteristics of the total power losses take the shape of a combination of these two components, where it is mostly influenced by the characteristics of the copper losses. The total loss peak is hence located at maximum torque and speed operating point and is around 3 kW.

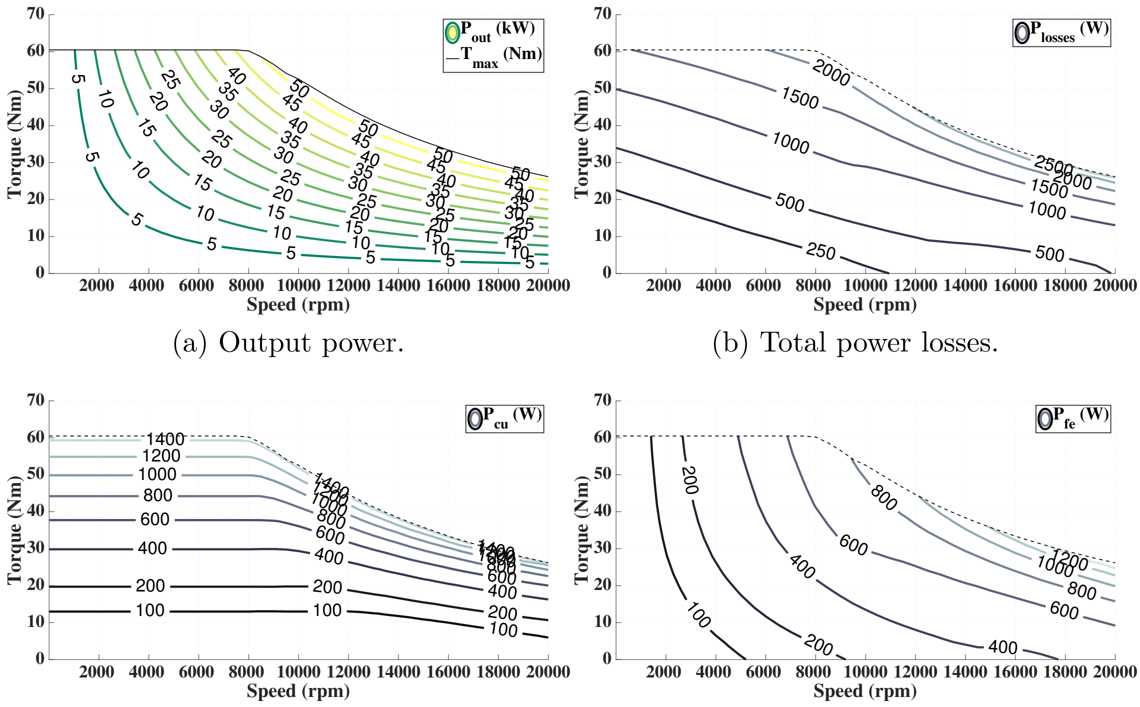

(a) Output power.

(b) Total power losses.

(c) Copper losses.

(d) Iron losses.

Figure 5.3 Output power and losses as a function of torque and speed, for the 8-pole PMSM.

Efficiency maps for the 4-pole PMSM in motoring and generation mode are presented in Figure 5.4 and 5.5, respectively. The highest efficiency is 96.4 % and is located in the centre point of the operating region at a speed of 10000 rpm and at a torque of 15 Nm. Between 7500-12000 rpm and 10-25 Nm, the machine has a operating efficiency of 96 %, but the area is though not as large as for the 8-pole PMSM. In the constant torque region, the machine can provide a maximum torque of 52.5 Nm. When the machine enters the field weakening region after the nominal speed point of 7400 rpm the torque falls off until maximum speed where it stops at 18 Nm. The characteristics of the efficiency map in generation reflects the characteristics in motoring mode, but marginally larger area with maximum efficiency, as for the 8-pole PMSM.

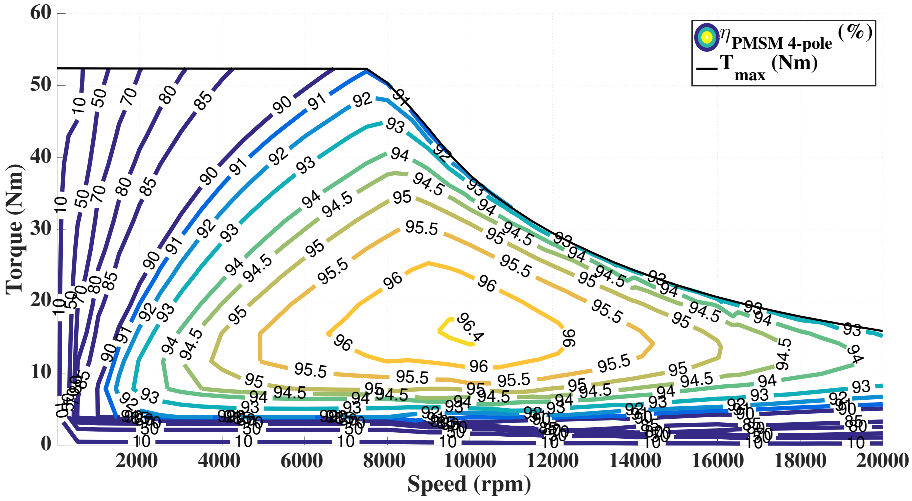

Figure 5.4 Efficiency map in motoring mode as a function of torque and speed, for the 4-pole PMSM.

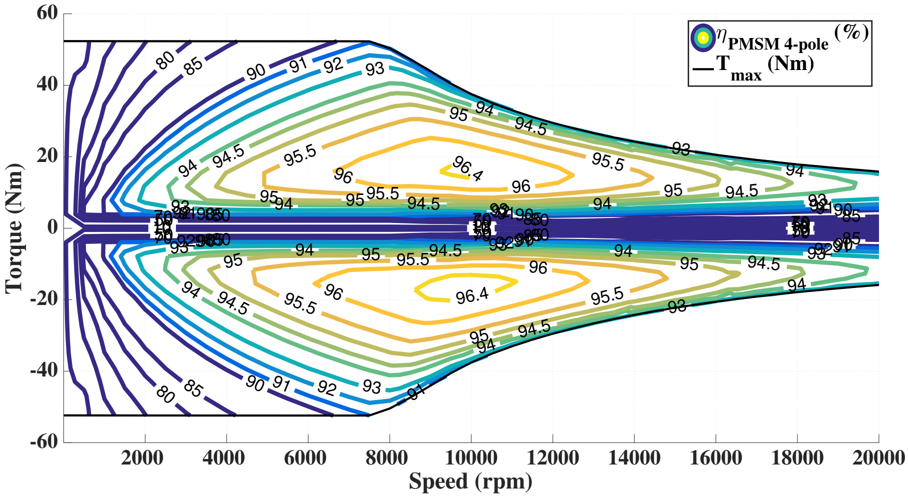

Figure 5.5 Efficiency map in motoring and generation mode as a function of torque and speed, for the 4-pole PMSM.

Figure 5.6 presents the mechanical output power and power losses for the whole operating region, for the 4-pole PMSM. The output power increases linearly until nominal speed is reached, where is reaches its peak power of 38 kW. Compared to the 8-pole PMSM, the machine does not have the ability to provide its peak power in the whole operating region above nominal speed. This is in line with the results from the MTPA algorithm in Figure 4.5.

The most dominant power losses are the copper losses. They are higher compared to the copper losses in the 8-pole PMSM since the winding pole pitch length is longer for the 4-pole PMSM. The peak of the copper losses occur when the machine can provide maximum current, i.e. below nominal speed at maximum torque and is around 3 kW. The iron losses are very speed dependent, but are not as dominant as the copper losses. Therefore, the total power losses are mostly torque dependent and have a peak of 3.5 kW at the maximum torque point at nominal speed.

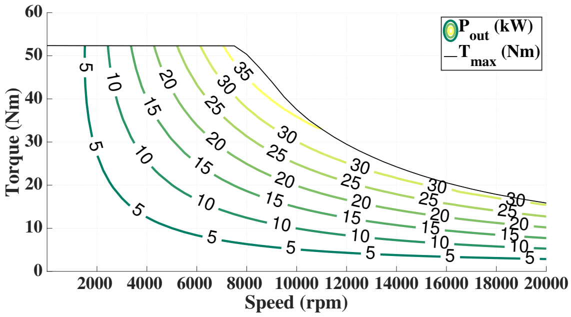

(a) Output power.

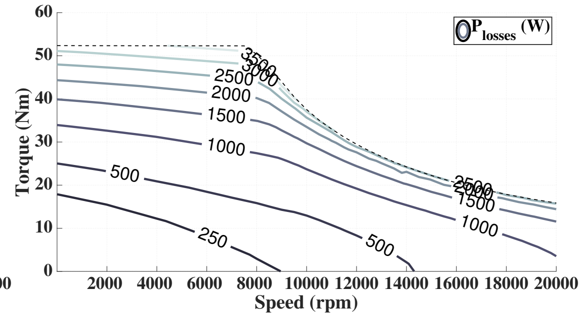

(b) Total power losses.

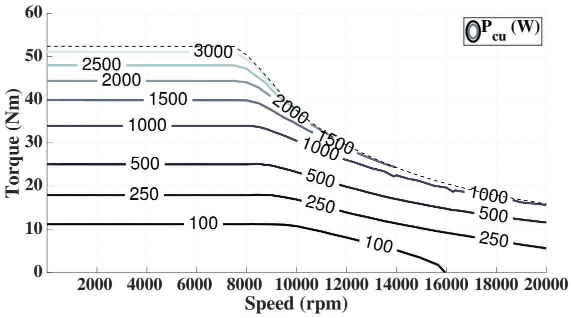

(c) Copper losses.

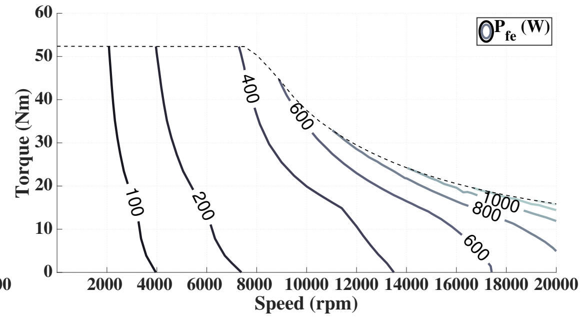

(d) Iron losses.

Figure 5.6 Output power and losses as a function of torque and speed, for the 4-pole PMSM.

Efficiency maps in both motoring and generation mode are presented in Figure 5.7 and 5.8 respectively, for the SynRM. Corresponding power losses components are included as for the PMSMs, excluding losses for the PMs. Highest efficiency point of 95 % is found in the operating region between 10000-12000 rpm, and 8-12 Nm. Areas with best efficiency are found in the field weakening region, whereas for the constant torque region the efficiency drops substantially.

Peak torque available in the operating region below nominal speed point is 44.8 Nm. Due to the absence of PMs, the SynRM cannot provide as high torque as the PMSMs. After nominal speed point, the torque drops quite dramatically and only 2 Nm can be provided at maximum speed.

Equivalent to the PMSMs, the efficiency map in generation mode for the SynRM reflects its characteristics in motoring mode, but where the operating area with peak efficiency is marginally expanded due to a increased magnetic flux flow in the air gap.

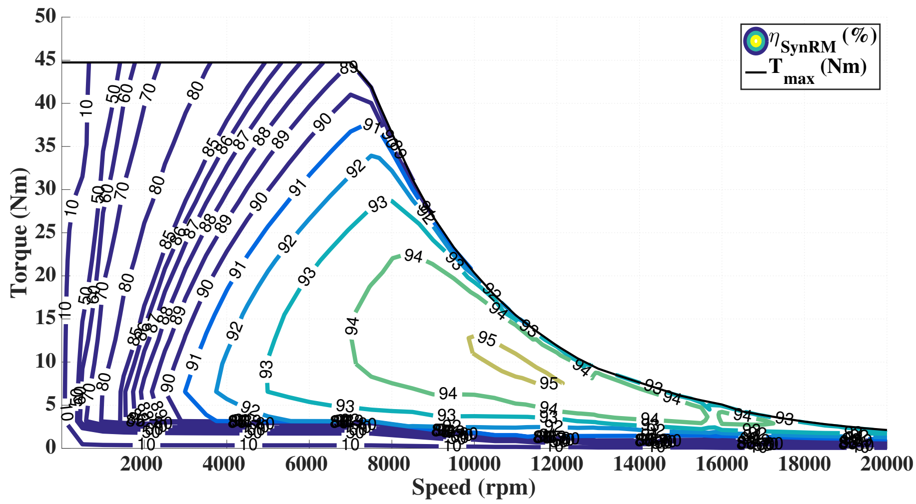

Figure 5.7 Efficiency map in motoring mode as a function of torque and speed, for the SynRM.

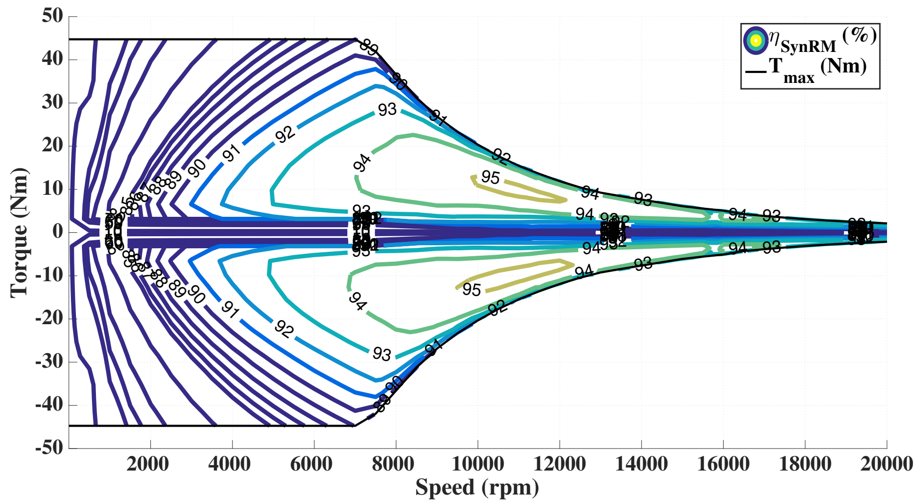

Figure 5.8 Efficiency map in motoring and generation mode as a function of torque and speed, for the SynRM.

Mechanical output power and power losses for the SynRM are presented in Figure 5.9. The output power increases linearly in the constant torque region until it reaches its peak power of 29 kW at the nominal speed point of 7000 rpm. The SynRM does not have the ability to maintain a flat constant power profile in the field weakening region. The output drops rapidly after the nominal speed point and at maximum speed the machine cannot even generate 5 kW of power. This can be associated with the design of the rotor barriers, which leads to a reduction in the saliency ratio during field weakening operation at high speeds [41]. The results are in line with plot of the MPTA algorithm in Figure 4.7.

The main power losses of the SynRM are copper losses and iron losses, presented in Figure 5.9 (c) and (d) respectively. Since the machine provides less torque for the same amount of current, the copper losses are higher compared to the 4-pole PMSM. The iron losses are mainly speed dependent, but at low torque levels they become very torque dependent and hence they are low slightly below maximum speed point. The characteristics of the total power losses resembles the copper losses, since they are the dominant loss component.

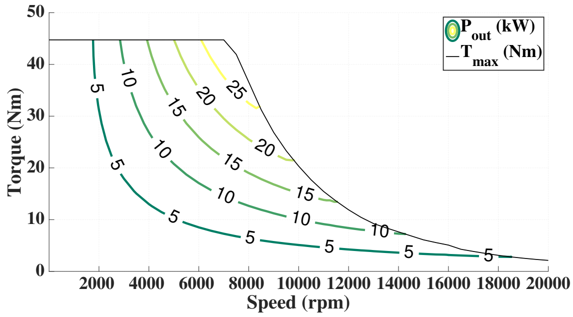

(a) Output power.

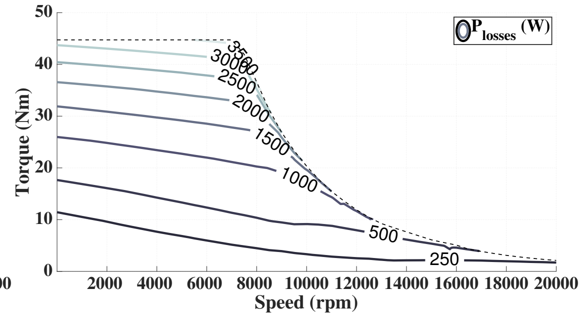

(b) Total power losses.

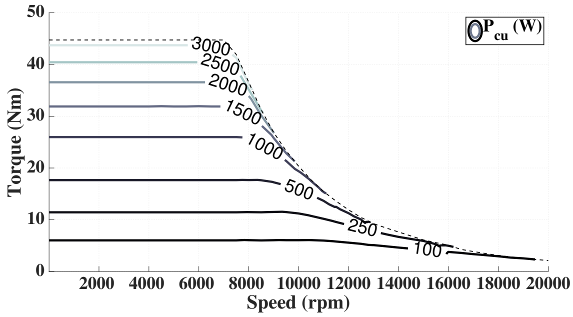

(c) Copper losses.

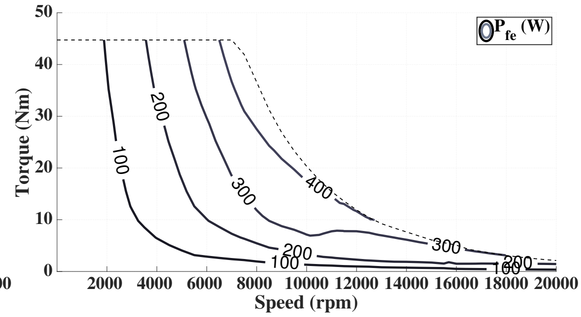

(d) Iron losses.

Figure 5.9 Output power and losses as a function of torque and speed, for the SynRM.

Efficiency maps in motoring and generation mode for the PMSynRM are presented in Figure 5.10 and 5.11. The losses of ferrite magnets can be categorized as core losses and due the low volume of the magnets and low impact of the iron losses, the magnet loss component are assumed to be negligible. Compared to the SynRM, the PMSynRM has an enhanced maximum efficiency along with expanded fields of improved performance. The maximum efficiency of 96 % is located between 12000-17000 rpm and 5-15 Nm. Additionally, the operating efficiency for low speed levels has increased. One could argue that this could be a beneficial feature, since an ISG in a mild hybrid system frequently operates at lower speed levels.

With ferrite magnets the maximum torque is increased to 51.8 Nm, which is roughly a 15 % increment compared to the SynRM. The reluctance torque contributes with about 75 % of the total torque production and the remaining 25 % is related to the ferrite magnets [12]. If the magnet placement in the PMSynRM had been optimized, an increment in maximum torque magnitude could probably been achieved. Overall, the introduction of ferrite magnets in the rotor barriers improve the performance in the whole operating range considerably.

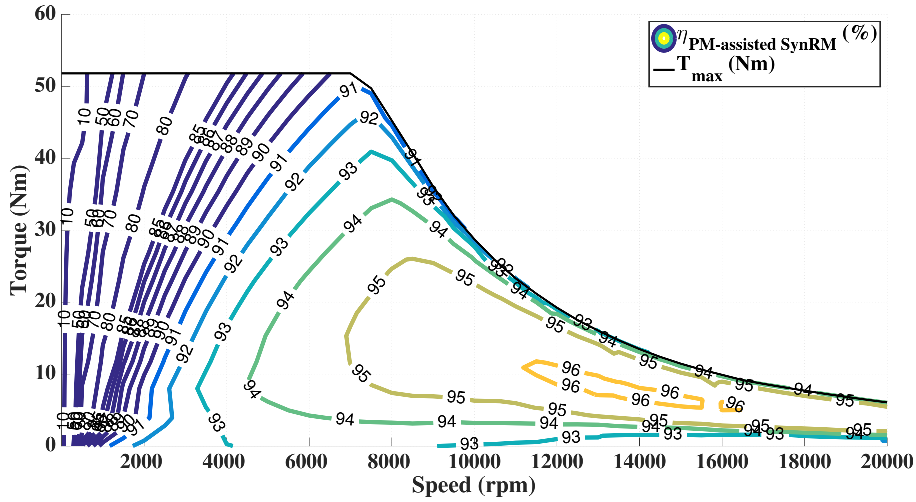

Figure 5.10 Efficiency map in motoring mode as a function of torque and speed, for the PMSynRM.

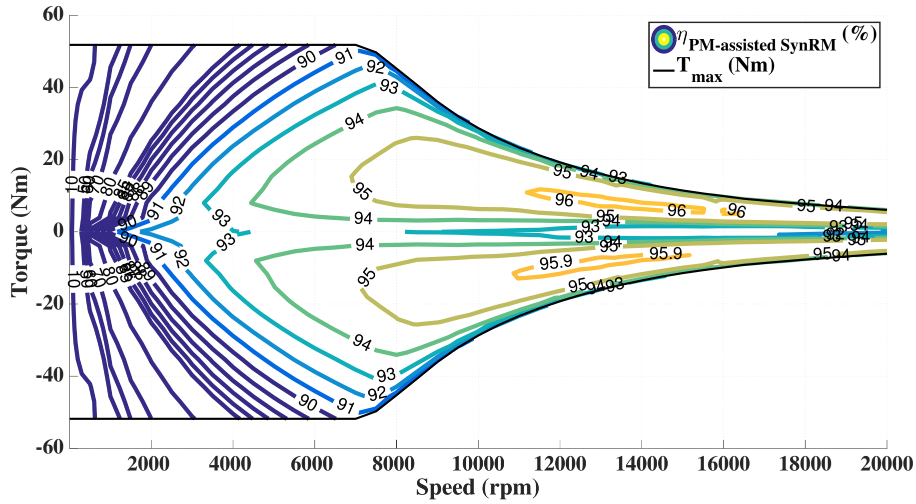

Figure 5.11 Efficiency map in motoring and generation mode as a function of torque and speed, for the PMSynRM.

The mechanical output power as well as power losses for the PMSynRM is presented in Figure 5.12. At nominal speed, the machine reaches a peak power of 35 kW, which can be provided until a speed level of 10000 rpm, which is an improvement compared to the SynRM where the output power drops rapidly after nominal speed. At maximum speed the PMSynRM can provide 10 kW of power. The ferrite magnets makes the machine less sensitive to a reduction of the saliency ratio in the field weakening region. Power losses mainly consists of copper and iron losses. Since the PMSynRM has the identical geometry as the SynRM, their iron losses resembles each other a lot. The PMSynRM can provide more torque compared to the SynRM for the same current magnitude, and hence it has lower copper losses.

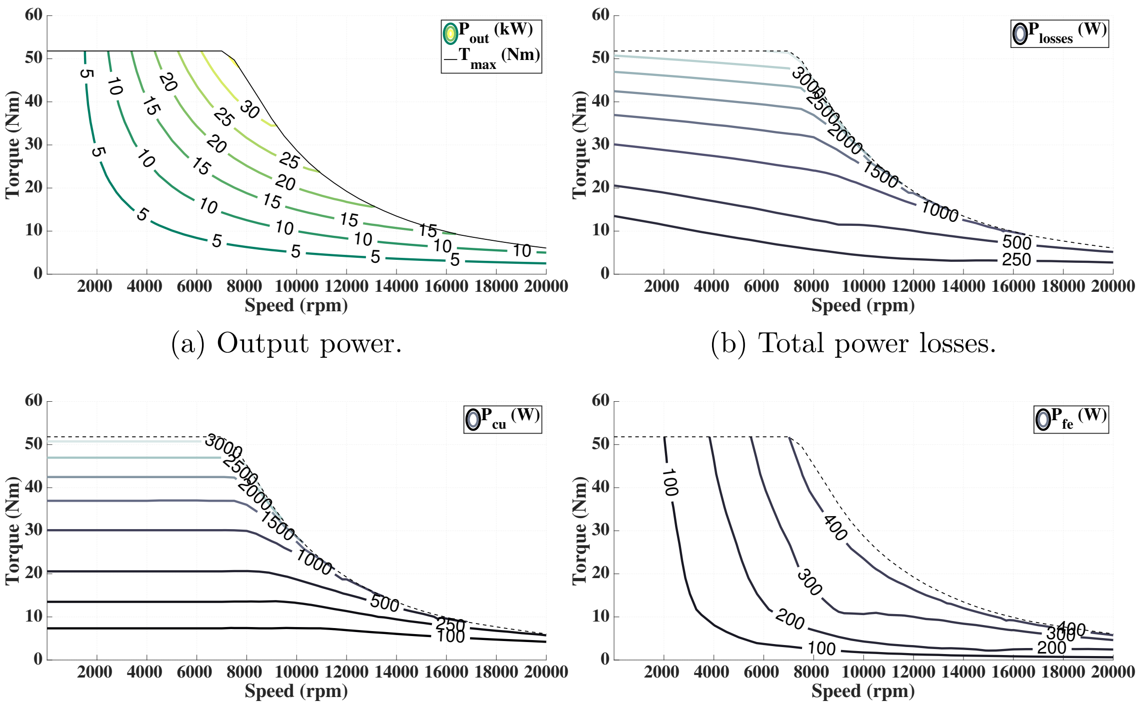

(a) Output power.

(b) Total power losses.

(c) Copper losses.

(d) Iron losses.

Figure 5.12 Output power and losses as a function of torque and speed, for the PMSynRM.

5.1.1 Initial attempt on the IM

Since slip of the machine needed to be evaluated for each operating point, the FEM simulations of the IM were considerably more time-consuming compared to the synchronous machines. For this reason, the IM has only been evaluated in motoring mode between a speed range of 1000-8500 rpm. However, by mapping the the slip by extrapolation as described in Chapter 4.5 a simulation with specific slip could be conducted in the constant torque region.

Efficiency map in motoring mode and mechanical output power for the IM are presented in Figure 5.13 (a) and (b), respectively. The highest efficiency of 94.7 % is found between 6700-8500 rpm and at a torque level between 10-15 Nm. In the constant torque region, the machine could provide a torque of 65 Nm. The efficiency map in generating mode is expected to reflect its characteristics in motor mode, but have not been evaluated due to the project time constraints. The output peak power of the IM increases linearly in the constant torque region and ends up at 50 kW when the voltage limit is reached.

Although the IM is not thermally analyzed, it can be observed in Figure 5.13 (c) that the power losses of the machine are about 1 kW higher in comparison to the other machines. This could be a indication that the temperature in the IM might be higher compared to the synchronous machines. The resistive losses in the stator copper windings and in the rotor aluminum bars are presented in Figure 5.13 (d) and (e). Also here it is shown that the resistive losses are dependent on the torque. The iron loss in the IM is shown in Figure 5.13 (f) and are mainly speed dependent. Since the resistive losses are the most dominant loss part, its characteristics resembles the total power losses of the IM.

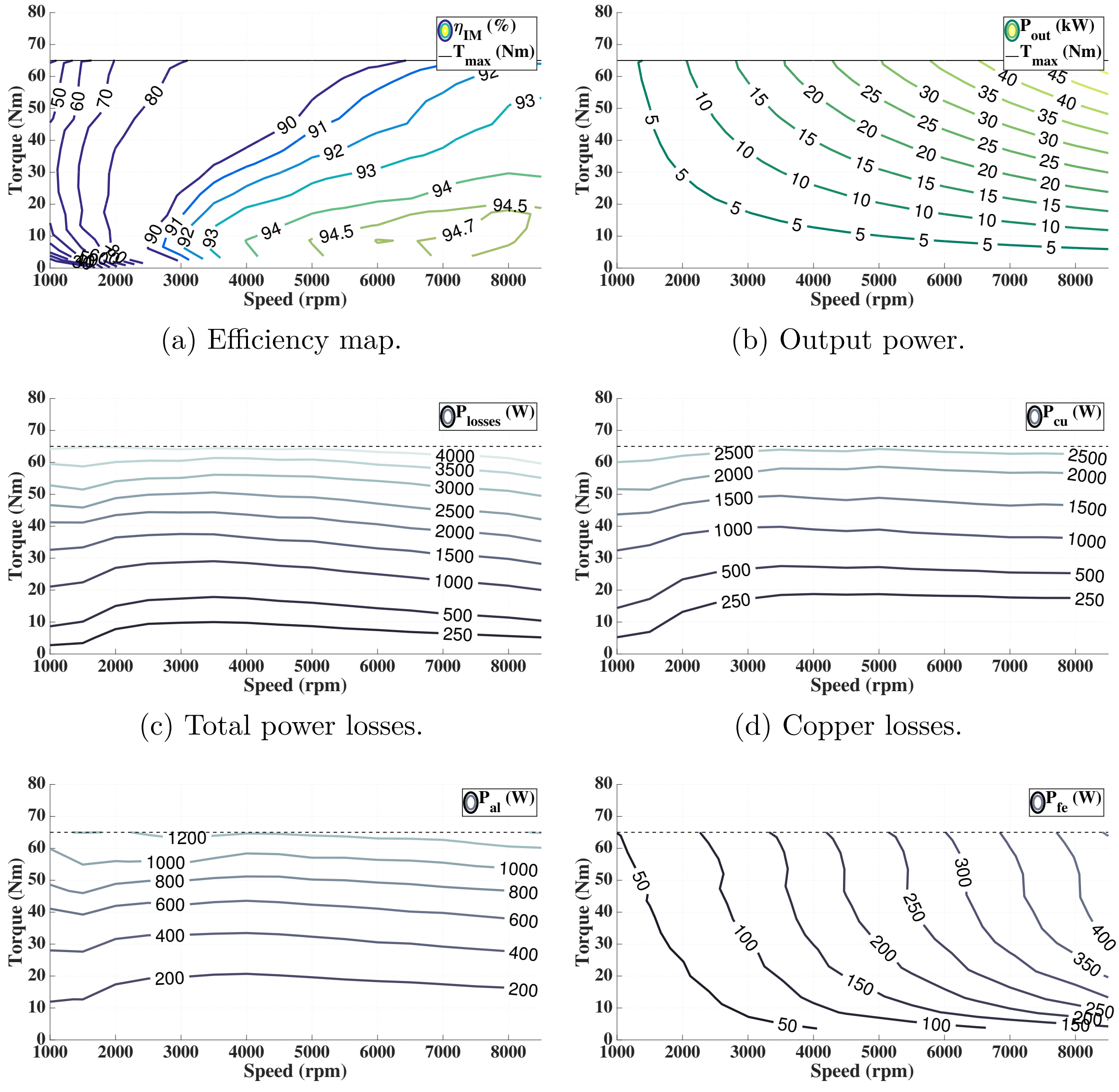

(a) Efficiency map. (b) Output power.

(c) Total power losses. (d) Copper losses.

(e) Rotor aluminum losses. (f) Iron losses.

Figure 5.13 Efficiency map in motoring mode, output power and losses as a function of torque and speed between 1000-8500 rpm, for the IM.

5.2 Comparative evaluation of performance

The operating points of interest specified in Section 4.1 are evaluated and presented in Table 5.1. It can be observed that only the 8-pole PMSM and the IM can provide the required cold crank torque of 55. The 8-pole PMSM machine also provides the highest output power at 2000 rpm and has the top efficiency during the most frequent operating point of 4600 rpm and 1 kW. Moreover, it can be concluded that the ferrite magnets of the PMSynRM enhance the performance at all operating points of interest significantly, compared to the SynRM. The IM shows promising performance, slightly below the 8-pole PMSM except the maximum torque, but does need to be thermally analyzed due the high resistive rotor losses.

Table 5.1 Comparison of machine performance at the operating points of interest.

	PMSM 8-pole	**PMSM 4-pole**	**SynRM**	**PMSynRM**	**IM**
Max. torque (Nm)	60.5	52.4	44.8	51.8	65
Max. output power @ 2krpm (kW)	11.1	7.6	6.1	7.6	9.6
Rms current magnitude @ 2krpm and 2.5kW (A)	347	251	496	382	370
Operating efficiency @ 4.6krpm and 1kW (%)	94.5	92.2	91.6	93.5	94.2

As the machines are designed to be operating in a mild hybrid vehicle it is of great importance to evaluate the weight of each machine, considering that car manufacturers tends to reduce or maintain a low vehicle weight in general. Mass of main machine components are presented in Table 5.2, along with the total mass. Mass is determined from material density and component volume. Cooling system and frame are not included, since they are equal for all machine topologies in this work.

The rotor of the SynRM is about 80 % lighter compared to the rotor weight of the PMSMs. The weight of the stator is somewhat equal for all machine topologies, except for some minor deviations due to the customized stator design processes. Mass of the stator winding differs between 8-pole and 4-pole machines. This is mainly due to the winding pole pitch length, for which is half the length in a 8-pole machine compared to a 4-pole machine with equal stator outer diameter. The IM is the heaviest machine due to the solid rotor design and the mass of the aluminum rotor bars.

Table 5.2 Mass of machine components (kg).

	PMSM 8-pole	**PMSM 4-pole**	**SynRM**	**PMSynRM**	**IM**
Stator lamination	4.98	4.98	5.53	5.53	5.53
Stator winding	2.41	3.10	3.04	3.04	3.04
Rotor lamination	3.06	3.07	0.85	0.85	3.68
Rotor winding	-	-	-	-	0.26
PMs	1.06	1.06	-	0.42	-
Total	**11.51**	**12.21**	**9.42**	**9.84**	**12.51**

The performance in relation to the mass and the volume of the machines are presented in Table 5.3. The cooling system and frame are not included. A stator outer diameter of 165 mm, a stack length of 80 mm and an axially winding overhang of 50 mm results in a volume of 2.78 dm^3 for all machines. The 8-pole PMSM has the best performance in relation to its mass and volume. However, at specific torque the PMSynRM matches the 8-pole PMSM due to its low weight and relative high maximum torque. It should be noticed that the performance between the 4-pole PMSM and the PMSynRM are very similar. This might be explained by an insufficient design of the 4-pole PMSM 4-pole or an optimized design of the PMSynRM, since it was expected that power density should be superior to other machine topologies [12].

Table 5.3 Comparison of power and torque density, and specific power and torque.

	PMSM 8-pole	**PMSM 4-pole**	**SynRM**	**PMSynRM**	**IM**
Power density (kW/dm^3)	19.67	13.84	10.56	12.75	18.2
Specific power (kW/kg)	4.69	3.11	3.08	3.56	4.00
Torque density (Nm/dm^3)	22.03	19.12	16.32	18.86	23.67
Specific torque (Nm/kg)	5.26	4.30	4.76	5.26	2.20

To accurately estimate the costs of an electric machine can be difficult due to price fluctuations of raw material over time which can also differ between different markets. In this work, only material costs are considered. The estimated cost of the materials per kilo are presented in Table 5.4. The rare-earth magnets chosen for the PMSMs are of type Hitachi NEOMAX NMX-37F expected to contain two rare-earth materials: around 31 % Neodymium and 3.5-4.5 % Dysprosium [25]. The costs were determined using data updated in the end of December 2016 [42]. The material cost of copper and aluminum are based on an average price over three months at London Metal Exchange, and have been collected in May 2017. Silicone steel is a type of iron alloy commonly utilized in electrical applications, for which the material cost is dependent on the alloy content. The price of the material was obtained from [43] and the material cost of ferrite magnets are collected from [44].

Table 5.4 Material cost.

	Cost (*USD/kg*)	**Cost** (*SEK/kg*)	**Collected**
Copper	5.7	49.7	May 24, 2017
Aluminum	1.9	16.6	May 24, 2017
Silicon Steel	2.1	18.3	[43]
NdFeB magnet	32.6	284	Dec 31, 2016 [42]
Ferrite magnet	7	61	[44]

The total cost of the materials used in the machines are presented in Table 5.5, along with the cost per torque for which the maximum torque is used. The SynRM is the least costly machine in terms of raw material, whereas the PMSM 4-pole is the most expensive. The NdFeB magnets are by far the most expensive material and represents about 50 % of the total material cost in the PMSMs. The least cost per torque is provided by the IM. However, due to the high power losses the thermal characteristics need to be evaluated if it is realistic to demand such high torque from the machine without causing overheating. The second best cost per torque is provided by the PMSynRM. The low cost of the ferrite magnets in combination with the optimized rotor design of the SynRM, makes it a cost effective choice for mild hybrid traction applications.

Table 5.5 Machine costs and costs per torque.

	PMSM 8-pole	**PMSM 4-pole**	**SynRM**	**PMSynRM**	**IM**
Cu (*SEK*)	119.7	153.9	150.9	150.9	150.9
Al (*SEK*)	-	-	-	-	4.3
Fe (*SEK*)	147.1	147.2	116.7	116.7	168.5
PM (*SEK*)	301	301	-	25.6	-
Material cost (*SEK*)	567.8	602.1	267.6	293.2	323.7
Cost/T (*SEK/Nm*)	9.38	11.49	5.97	5.66	4.98

As the mild hybrid system should contribute to the reduction of CO_2 emissions in the transportation sector, it is by great significance to evaluate the environmental impacts related to the electric machine production. One approach of measuring the environmental impact related to production of raw materials is in CO_2 equivalents ($kg{\cdot}CO_2\text{-}eq$), which converts all emitted gases from the process into CO_2 weight. The CO_2 equivalents of the material used in the machines is presented in Table 5.6, where the PMs are assumed to be produced in China with a local energy mix [45]. The NdFeB magnets has the highest environmental impact of the materials used in the machine topologies. However, there is a possibilities of reduction by using recycled magnets, in this way the CO_2 equivalent could be lowered [46].

The emissions of the material produced for each machine part is presented in Table 5.7. It can be observed that the PMSMs have a higher total CO_2 equivalent due to the NeFeB magnets. Even though PMSynRM utilize ferrite magnets, it ends up being less environmental harmful in comparison to the IM. The reason of this is the solid rotor of the IM. The machine with the least environmental impact in terms of materials is the SynRM, which is produced using a material combination emitting 53 % less greenhouse gas in comparison to the one in the 4-pole PMSM.

Table 5.6 CO_2 equivalent per kilo produced material.

	Environmental impact ($kg{\cdot}CO_2\text{-}eq$)
Copper	5.93 [47]
Aluminum	15.2 [47]
Steel	1.5 [47]
NdFeB magnet	57.1 [45]
Ferrite magnet	15.2 [45]

Table 5.7 Comparison of the CO_2 equivalent emitted while producing the material of the machines.

	PMSM 8-pole	**PMSM 4-pole**	**SynRM**	**PMSynRM**	**IM**
Cu ($kg{\cdot}CO_2\text{-}eq$)	14.3	18.4	18.0	18.0	18.0
Al ($kg{\cdot}CO_2\text{-}eq$)	-	-	-	-	4.0
Fe ($kg{\cdot}CO_2\text{-}eq$)	12.1	12.1	9.6	9.6	13.8
PM ($kg{\cdot}CO_2\text{-}eq$)	60.5	60.5	-	6.4	-
Total ($kg{\cdot}CO_2\text{-}eq$)	55.0	59.1	27.6	34.0	35.8

5.3 Full vehicle system simulations

The machine performance in both motoring and generation mode have been implemented in full vehicle simulations conducted by supervisor Stefan Skoog. Operating points for an ISG in a 48 V mild hybrid test vehicle with P0 topology and transmission ratio 1:3 have been registered during highway and city drive routes. The registered operating points have been implemented in the efficiency maps for all machine topologies, in order to examine the machines as a part of the vehicle system.

5.3.1 Highway drive

A map over the drive route and logged drive cycle for the highway test drive are shown in Figure 5.14. The test drive was conducted around the area of Säve airport. The registered drive cycle shows a driving pattern with recurrent constant speed periods, many around 70 km/h with some variations, and some speed transients.

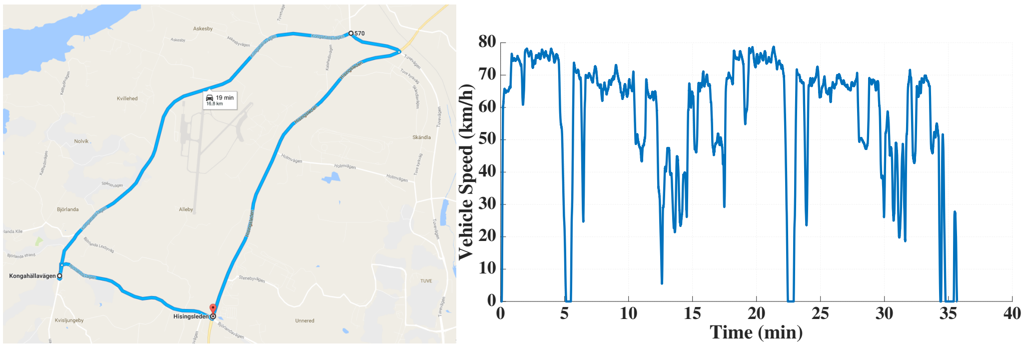

(a) Drive route.

(b) Drive cycle.

Figure 5.14 Drive route and logged drive cycle with vehicle speed over time, for the highway test drive around Säve airport.

Figure 5.15 presents registered operating points for the ISG during the highway test drive, implemented in the efficiency maps for all simulated machine topologies. It can be observed that the ISG operates frequently between 3000-6000 rpm, mainly at torque levels between -10 and 10 Nm. It is very active in generation mode, providing regenerative braking torque to the energy storage system. Some operating points exists at low speeds and high torque levels, where the ISG cranks the ICE.

The operating points for the ISG does however not intersect with the operating regions of highest efficiency, for neither of the machines. Since the highest speed of which the ISG operates at is located around 7000 rpm, it does not intersects with the highest efficiency areas which are mostly located between 10000-16000 rpm. If the operating points should intersect more frequent with the areas of highest efficiency, the machines could be redesigned in order to shift the highest efficiency operating area closer to lower speed levels. As a suggestion, the stator windings turns could be reduced or use two winding layers instead. Another approach could be to use a higher transmission ratio in order to shift operating points of the ISG against higher speed levels. It is though important to ensure that the machine has the capability to operate continuously at maximum speed.

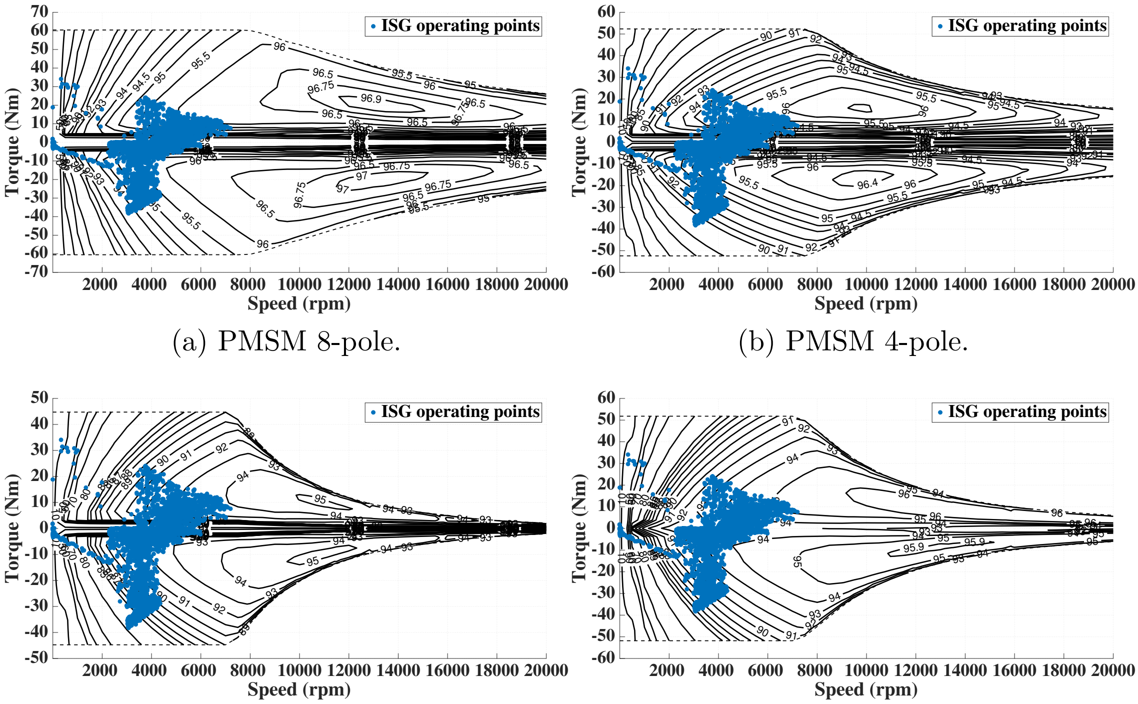

(a) PMSM 8-pole.

(b) PMSM 4-pole.

(c) SynRM.

(d) PMSynRM.

Figure 5.15 Efficiency maps in motoring and generation mode with registered operating points from the ISG for the highway test drive.

Efficiency at all operating points during the highway drive cycle, accumulated power losses as well as rms efficiency for the examined machine topologies are presented in Figure 5.16. The 8-pole PMSM has the highest rms efficiency of 92.5 % and lowest accumulated losses at the end of the drive route. Lowest rms efficiency has the SynRM with 89.5 %. Since the PMSynRM has high efficiency within low torque level regions in both motoring and generation mode where most of the ISG operating points are located, its rms efficiency is slightly higher compared to the 4-pole PMSM, for which the efficiency drops considerably at low torque levels.

Moreover, it can be concluded that for the highway drive cycle the 8-pole provides the most sufficient performance in terms of rms efficiency and accumulated power losses. The PMSynRM could also be considered as a suitable option due to its satisfactory performance in relation to its low costs.

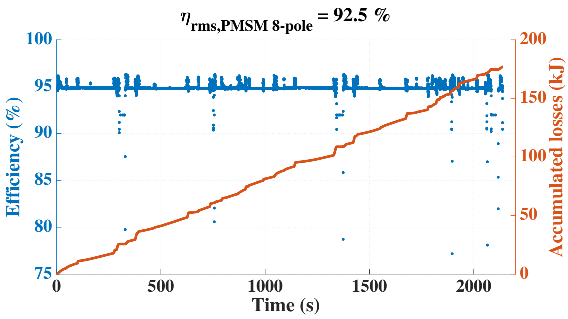

(a) PMSM 8-pole.

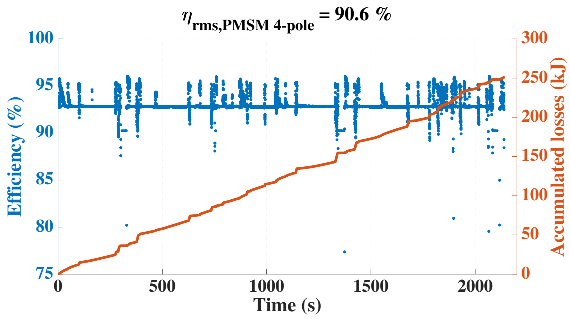

(b) PMSM 4-pole.

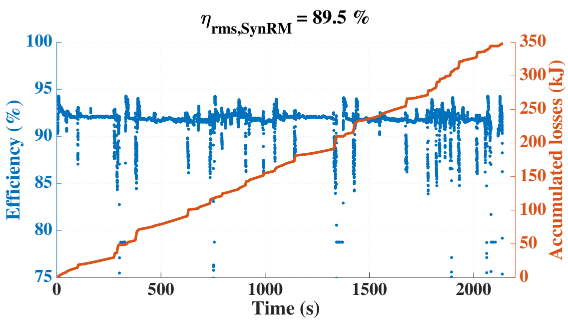

(c) SynRM.

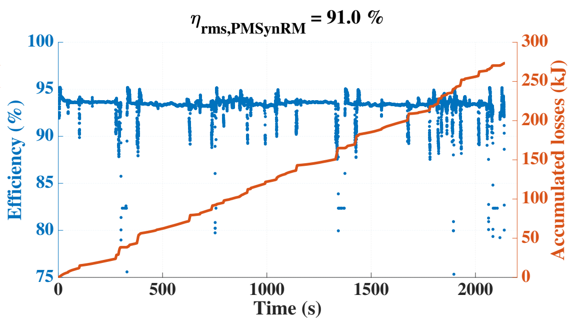

(d) PMSynRM.

Figure 5.16 Machine efficiency at all operating points and accumulated power losses over time, as well as rms efficiency, during the highway drive cycle.

5.3.2 City drive

Map over the drive route and logged drive cycle for the city test drive are shown in Figure 5.17. The test drive was conducted in the area of Lundby and Sannegården. The registered drive cycle shows a driving pattern with frequent speed transients and with a vehicle speed mostly around 30-40 km/h.

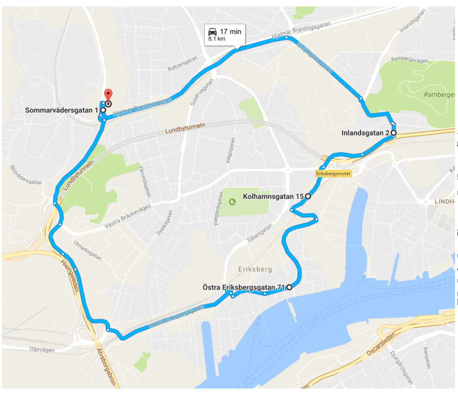

(a) Drive route.

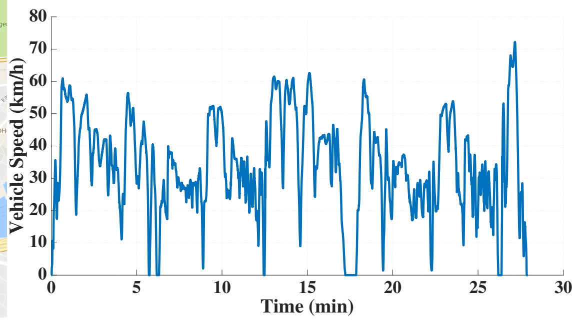

(b) Drive cycle.

Figure 5.17 Drive route and logged drive cycle with vehicle speed over time, for the city test drive in the area of Lundby and Sannegården.

Registered operating points for the ISG during the city test drive are presented in Figure 5.18. As for the highway drive cycle, the operating points are added to the efficiency maps in motoring and generation mode for all machine topologies in order to examine the convergence between ISG operating points and areas with high efficiency. The city drive cycle has many speed transients due to rapid deceleration and accelerations, and hence more operating points are located at low speeds and high torque levels compared to the highway drive cycle. The operating points of the ISG do not intersect with the areas of highest efficiency. As suggested, a higher transmission ratio could be appropriate or a different machine design in order to lower the nominal speed point.

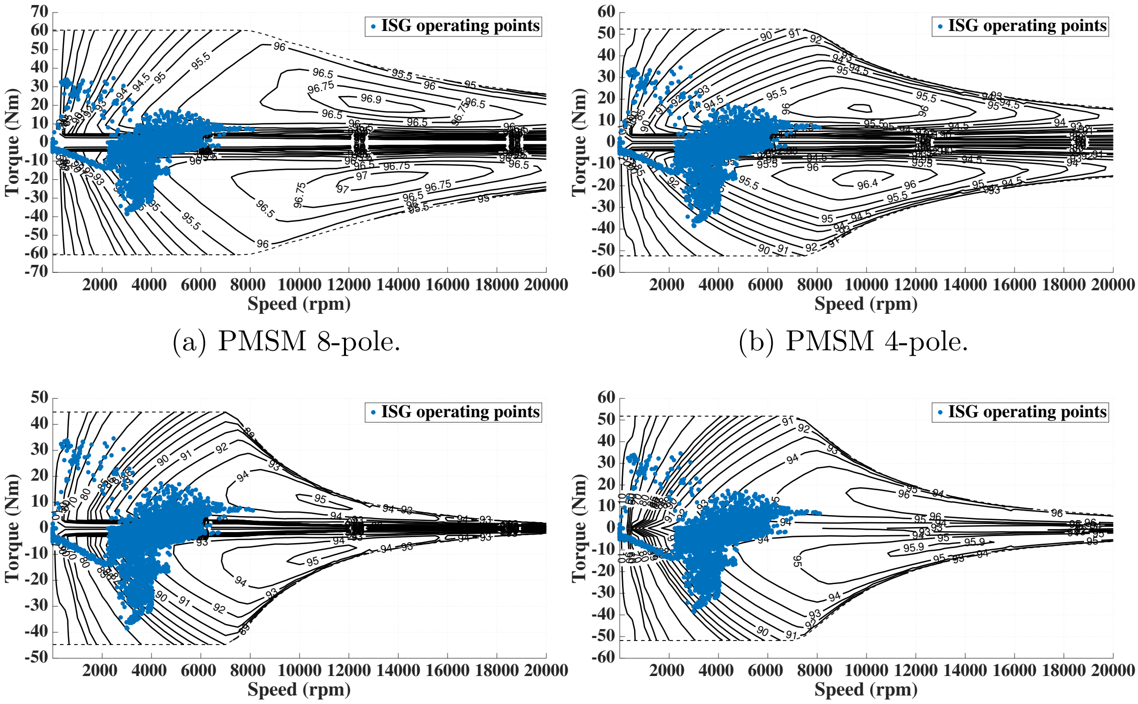

(a) PMSM 8-pole. (b) PMSM 4-pole. (c) SynRM. (d) PMSynRM.

Figure 5.18 Efficiency maps in motoring and generation mode with registered operating points from the ISG for the city test drive.

Figure 5.19 presents efficiency of all operating points during the city drive cycle, accumulated power losses and rms efficiency for the examined machine topologies. The rms efficiency is slightly lower compared to the highway drive cycle, since the city drive cycle has more operating points at low speed and high torque areas where the operating efficiency is generally low. The 8-pole PMSM has likewise the highest rms efficiency with 90.3 %, whereas the SynRM has the lowest with 87.4 %.

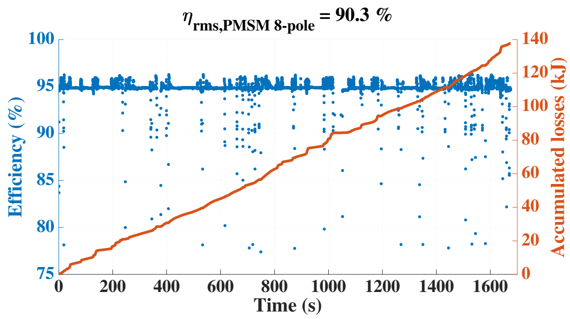

(a) PMSM 8-pole.

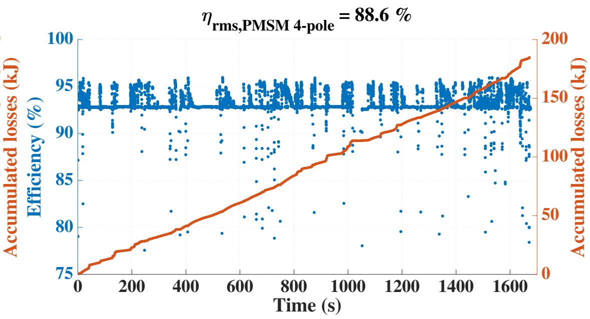

(b) PMSM 4-pole.

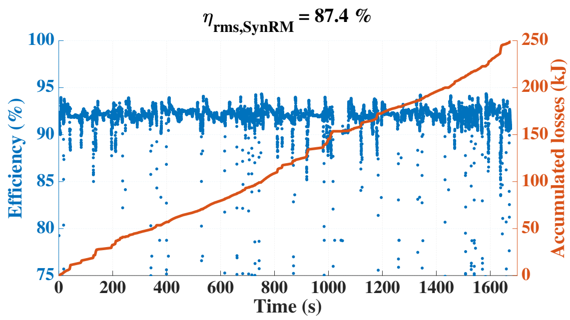

(c) SynRM.

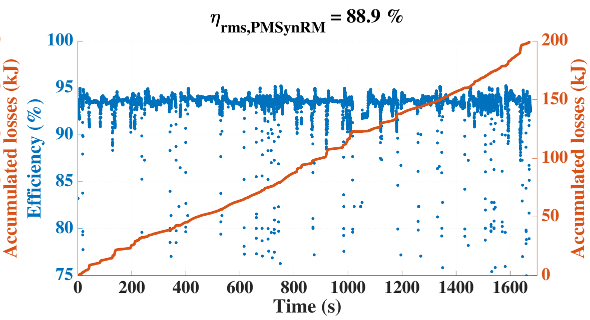

(d) PMSynRM.

Figure 5.19 Machine efficiency at all operating points and accumulated power losses over time, as well as rms efficiency, during the city drive cycle.

6

Implementation and Evaluation of Thermal Models

During periods of high load demand, electric machines experience increasing power losses which can cause the internal temperature to rise substantially. Frequent temperature fluctuations with high peaks can diminish the machine performance considerably and have severe impacts on the machine lifetime. It is hence of great importance to accurately estimate the temperature distribution in the various machine parts. The following chapter discusses the methodology of the implemented lumped-parameter thermal models, presents resulting temperature characteristics to a load step, and evaluates how appropriate each machine topology is in terms of temperature performance.

6.1 Lumped-parameter network models

The lumped-parameter network models are in this work based on a 9-node thermal network representing a water cooled IPMSM [25], where the internal heat generation is assumed to be evenly distributed in each machine section. For the PMs, heat transfer is considered in the radial direction only, whereas heat transfer in the axial direction only is assumed for the windings and the shaft.

Implemented thermal network are electrically represented in Figure 6.1 and 6.2, for the PMSMs, SynRM and PMSynRM, respectively. The 9-node thermal network has been utilized as base, but the rotor region has been modified according to respected machine topology. The models include heat distribution between the main machine parts and provide the possibility to anticipate the temperature response in each network node, with the help of input data as power losses in the stator yoke and teeth, active and end windings, PMs, rotor yoke and bearings.

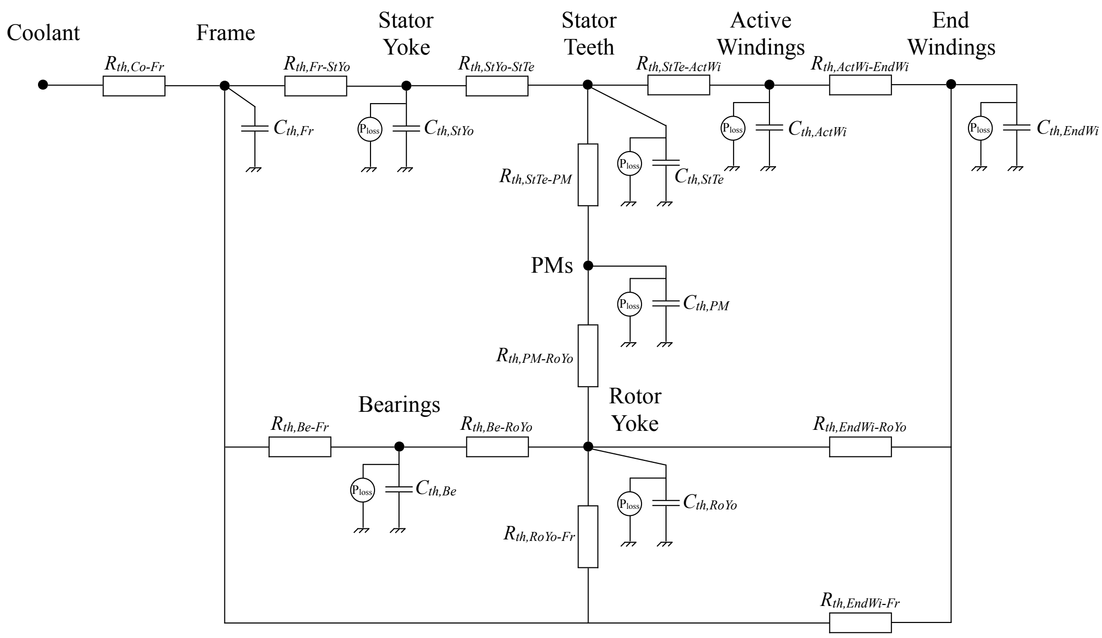

Figure 6.1 Implemented thermal network model, utilized for the PMSMs and the PM-SynRM.

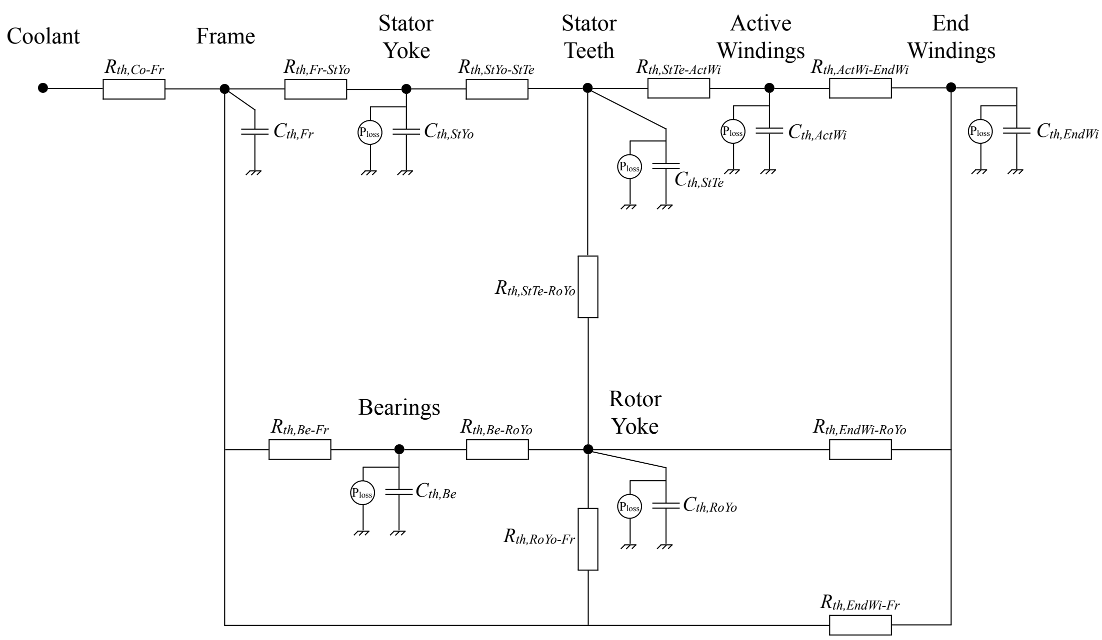

Figure 6.2 Implemented thermal network model, utilized for the SynRM.

6.1.1 Stator frame and cooling

The cooling system utilized for all machines in this work are assumed to be a water cooling system with a temperature of 65°C and a flow rate of 6 L/min, shaped as a spiral of four turns containing channels with rectangular cross sections. Each cooling channel has a width ω_{cool} of 30 mm, a height h_{cool} of 5 mm, and are distanced by 10 mm from each other [25]. In order to maintain a compact machine construction and a consistent temperature distribution along the stator aluminum frame, the channels are assumed to be integrated inside the frame. From the inner and outer frame boundaries there exists a radial distance $l_{Fr,low}$ of 3 mm to the cooling channels.

The stator frame is modelled as a hollow cylinder with an inner and outer radius of $r_{Fr,in}$ and $r_{Fr,in}+l_{Fr,low}$, respectively. For simplicity, only the radial heat transfer between inner surface of the cooling channels and the outer surface of the stator frame are considered and hence the conductive thermal resistance of the stator frame can be calculated as followed.

$$R_{th,Fr} = \frac{ln\left(\frac{r_{Fr,in}+l_{Fr,low}}{r_{Fr,in}}\right)}{2\pi\lambda_{Al}l_{stk}} \tag{6.1}$$

The surface area of the inner cooling channel boundaries is calculated as

$$A_{cool} = 4 \cdot 2\pi\omega_{cool}(r_{Fr,in} + l_{Fr,low}) \tag{6.2}$$

and with a correction factor $k_{conv,corr}$ of 0.5 since it is assumed that half of the total heat flux between the cooling channels and the stator frame goes through the inner channel surface. The convection thermal resistance for the cooling system can then be expressed as

$$R_{th,Co} = \frac{k_{conv,corr}}{A_{cool}\alpha_{trans}} \tag{6.3}$$

where α_{trans} is the average heat transfer coefficient (W/m^2K). For turbulent flow, α_{trans} is a function of the coolant temperature and the flow rate, and with 65°C and 6 L/min gives an average heat transfer coefficient of 1988 W/m^2K [25]. The network node of the stator frame is placed radially in the middle of the frame. Therefore, the thermal resistance from the coolant node point to the stator frame node point can be calculated from

$$R_{th,Co-Fr} = R_{th,Co} + \frac{1}{2}R_{th,Fr} \tag{6.4}$$

The thermal capacitance of the stator frame has a volume consisting of a hollow cylinder representing the frame cylinder, but without the volume of the cooling system channels, and two end caps. All thermal capacitances are determined according to (3.49).

6.1.2 Stator yoke

The stator yoke is modeled as a hollow cylinder with perfectly insulated laminated sheets of electrical steel, and thus assuming only radial heat flow [33]. The thermal resistance of the stator yoke can then by expressed as

$$R_{th,StYo} = \frac{ln\left(\frac{r_{Yo,out}}{r_{Yo,in}}\right)}{2\pi\lambda_{Fe}l_{th,cond}} \tag{6.5}$$

where $r_{Yo,out}$ and $r_{Yo,in}$ are the outer and inner stator yoke radius respectively and $l_{th,cond}$ is the thermally conductive core length and is calculated from [25]

$$l_{th,cond} = k_{sf}l_{stk} \tag{6.6}$$

where k_{sf} is the stacking factor and assumed to be 0.95. The interface between the aluminum frame and the stator yoke will always contain a small air pocket that will affect the heat transfer due to the low thermal conductivity of air. This contact resistance between the two machine parts are modeled as a hollow cylinder with a thickness $l_{contFr-Yo}$ of 10 μm and can be expressed as

$$R_{th,contFr-StYo} = \frac{ln\left(\frac{r_{Yo,out}+l_{contFr-Yo}}{r_{Yo,out}}\right)}{2\pi\lambda_{Air}l_{stk}} \tag{6.7}$$

The network node of the stator yoke is placed radially in the middle of the yoke and hence the thermal resistance from the stator frame node point to the stator yoke node point can be described by

$$R_{th,Fr-StYo} = \frac{1}{2}R_{th,Fr} + R_{th,contFr-StYo} + \frac{1}{2}R_{th,StYo} \tag{6.8}$$

The volume for the thermal capacitance of the stator yoke is modelled as a hollow cylinder.

6.1.3 Stator teeth

By assuming radial heat transfer only due to the perfect insulation between the between the sheets of electrical steel, all the thermal resistances for the stator teeth can be modeled to be in parallel with each other. By integration along the radial direction with the teeth, the total thermal resistance can be determined from [25]

$$R_{th,StTe} = \int_{St,in}^{StYo,in} \frac{1}{\lambda_{Fe}Q_s l_{th,cond} w_{tooth}(r)} dr \tag{6.9}$$

where $r_{StYo,in}$ and $r_{St,in}$ are the radial distances to the inner stator yoke and inner stator point respectively and thus represents the total length of a single tooth, Q_s is the number of stator slots and w_{tooth} is the tooth width which varies with the radial coordination. Alternatively, the integration in 6.9 can be replaced by an analytical expression specific to tooth geometry [33]. With a known stator tooth geometry as illustrated in Figure 6.3, the total thermal resistance of the stator teeth can be calculated as

$$R_{th,StTe} = \frac{1}{\lambda_{Fe} Q_s l_{th,cond}} \left[\frac{y_1}{x_1} + \frac{y_3}{x_3} + \frac{y_2}{x_1 - x_2} \left(ln \left| \frac{x_1 y_2}{x_1 - x_2} \right| - ln \left| y_2 - \frac{x_1 y_2}{x_1 - x_2} \right| \right) - \right.$$
$$\left. - \frac{\pi}{4} + \frac{a}{\sqrt{a^2 - 1}} \arctan \left(\frac{a + 1}{\sqrt{a^2 - 1}} \right) \right] \quad (6.10)$$

where a is defined as followed.

$$a = \frac{x_3 + 2y_4}{2y_4} \quad (6.11)$$

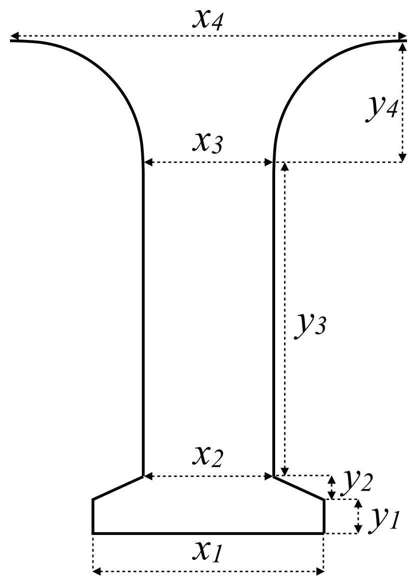

Figure 6.3 Stator tooth geometry.

The network node of the stator teeth is located radially in the middle of the teeth and therefore the thermal resistance from the stator yoke node point to the stator teeth node point consists of half the thermal resistance from each machine part, as in

$$R_{th,StYo-StTe} = \frac{1}{2} R_{th,StYo} + \frac{1}{2} R_{th,StTe} \quad (6.12)$$

The thermal capacitance of the stator teeth has a volume found from the surface area of the stator teeth and rim, which are measured in Ansys Maxwell, multiplied with the stack length.

6.1.4 Stator windings

Power losses for all electric machines studied in this work mainly consists of resistive losses in the stator copper windings, and in the rotor aluminum bars for the IM. Therefore, it is essential to model the thermal distribution for these machine parts in a proper way in order to achieve accurate estimations of the temperature characteristics.

The stator windings are modelled as an equivalent rectangular slot shape consisting of a homogeneous mixture of winding copper and impregnation material, which for simplicity are assumed to have uniform heat dissipation [33]. From the average value of the upper $w_{slot,up}$ and lower slot width $w_{slot,low}$, the total width of the equivalent rectangular slot is calculated as

$$w_{slot,eq} = \frac{w_{slot,up} + w_{slot,low}}{2} - 2(d_{slot,lin} + d_{slot,air}) \tag{6.13}$$

where $d_{slot,lin}$ and $d_{slot,air}$ are two surface layers around the equivalent winding mix representing the slot liner of 0.164 mm and an air film of 10 μm, respectively [25]. The total height of the equivalent rectangular slot is found from

$$h_{slot,eq} = \frac{2A_{slot}}{w_{slot,up} + w_{slot,low}} - 2(d_{slot,lin} + d_{slot,air}) \tag{6.14}$$

where A_{slot} is the area of one original stator slot. The thermal resistance from the stator teeth node point to the active winding node point are estimated as [33]

$$R_{th,StTe-ActWi} = \frac{R_w R_h}{Q_s l_{th,cond}(R_w + R_h)}\left(1 - \frac{R_{w0}R_{h0}}{720(R_{w0} + R_{h0})}\right) \tag{6.15}$$

where R_w, R_h, R_{w0} and R_{h0} are thermal resistances per unit length in the width and height directions, respectively. The resistances R_w and R_h are defined as

$$R_w = 0.5(R_{iw} + \frac{R_{w0}}{6}) \tag{6.16}$$

$$R_h = 0.5(R_{ih} + \frac{R_{h0}}{6}) \tag{6.17}$$

where R_{iw} and R_{ih} are thermal resistances per unit length which the slot liner and air film contributes with and they are found from

$$R_{iw} = \frac{d_{slot,lin}}{\lambda_{slot,lin} h_{slot,eq}} + \frac{d_{slot,air}}{\lambda_{air} h_{slot,eq}} \tag{6.18}$$

$$R_{ih} = \frac{d_{slot,lin}}{\lambda_{slot,lin} w_{slot,eq}} + \frac{d_{slot,air}}{\lambda_{air} w_{slot,eq}} \tag{6.19}$$

where $\lambda_{slot,lin}$ is the thermal conductivity of the slot liner and is assumed to be 0.2 W/mK [25]. The thermal resistances of the equivalent winding mix are found from

$$R_{w0} = \frac{w_{slot,eq}}{\lambda_{Wi,mix} h_{slot,eq}} \tag{6.20}$$

$$R_{h0} = \frac{h_{slot,eq}}{\lambda_{Wi,mix} w_{slot,eq}} \tag{6.21}$$

where $\lambda_{Wi,mix}$ is the thermal conductivity of the equivalent winding mix and is assumed to be equal to 0.55 W/mK [25]. With an axial heat flow from the active winding to the end winding, occurring in parallel in the stator slots, the thermal resistance between the active and end winding node points is

$$R_{th,ActWi-EndWi} = \frac{l_{av}}{6Q_s A_{Cu} \lambda_{Cu}} \tag{6.22}$$

where A_{Cu} is the cross sectional area of one copper winding. The cross sectional area of one winding is multiplied with the total number of slots together with the stack length or the length of winding overhang, in order to obtain the volumes of the active and end windings, respectively. Thus thermal capacitances of the active and end windings can be determined.

6.1.5 Internal air

Internal air includes all the air inside the frame except for the air gap between stator and rotor. It consists of three different convective thermal resistances between the end regions of the machines to the internal air node point, which are thus from the inner frame surface, the rotor end shield surface and the end winding surface. The thermal resistances are linked in a Y-connection centered around the internal air node point, each with an own heat transfer coefficient [33]. The thermal resistance for the convective heat transfer to the frame is defined as

$$R_{th,InAir-Fr} = \frac{1}{\alpha_{Fr,in} A_{Fr,in}} \tag{6.23}$$

where $A_{Fr,in}$ is the inner frame surface area, which consists of two inner end shield areas and the inner frame shell surface area. The convective heat transfer coefficient for the inner frame surface $\alpha_{Fr,in}$ is empirically determined from [48]

$$\alpha_{Fr,in} = 15 + 6.75 v_r^{0.65} \tag{6.24}$$

where v_r is the rotor peripheral speed (m/s). The thermal resistance for the convective heat transfer of the rotor end shield is determined from

$$R_{th,InAir-Ro} = \frac{1}{\alpha_{Ro} A_{Ro}} \tag{6.25}$$

where its area A_{Ro} is calculated as a circular surface area with the average air gap radius [25], and its convective heat transfer coefficient α_{Ro} is expressed as [48]

$$\alpha_{Ro} = 16.5 v_r^{0.65} \tag{6.26}$$

The thermal resistance for the convective heat transfer between the end winding surface and the internal air is defined as

$$R_{th,InAir-EndWi} = \frac{1}{\alpha_{EndWi} A_{EndWi}} \tag{6.27}$$

where its area is approximated as [48]

$$A_{EndWi} = \pi l_{passive} r_{EndWi,av} \tag{6.28}$$

where $r_{EndWi,av}$ is the end winding average radial distance. Its convective heat transfer coefficient empirically approximated from [48]

$$\alpha_{EndWi} = 6.5 + 5.25 v_r^{0.6} \tag{6.29}$$

For simplicity, the Y-node is converted to a Δ-node in order to remove the internal air node point. The net thermal conductance G_T then becomes as followed.

$$G_T = \frac{1}{R_{th,InAir-Fr}} + \frac{1}{R_{th,InAir-Ro}} + \frac{1}{R_{th,InAir-EndWi}} \tag{6.30}$$

The thermal resistances between the rotor yoke node point and the stator frame node point, between the end winding node point and the rotor yoke node point, and between the end winding node point and the stator frame node point can then be respectively expressed as

$$R_{th,RoYo-Fr} = \frac{R_{th,InAir-Fr} R_{th,InAir-Ro} G_T}{2} \tag{6.31}$$

$$R_{th,EndWi-RoYo} = \frac{R_{th,InAir-Ro} R_{th,InAir-EndWi} G_T}{2} \tag{6.32}$$

$$R_{th,EndWi-Fr} = \frac{R_{th,InAir-Fr} R_{th,InAir-EndWi} G_T}{2} \tag{6.33}$$

6.1.6 Air gap

The air gap between the stator and rotor has a cylindrical surface area A_{AirGap} along the stack length, with an average air gap radius. The thermal resistance for the air gap can then be determined as

$$R_{th,AirGap} = \frac{1}{\alpha_{AirGap} A_{AirGap}} \tag{6.34}$$

where α_{AirGap} is the average air gap heat transfer coefficient and is dependent on the temperature and the speed of the machine. For simplicity, α_{AirGap} is in this work assumed to be equal to 130 W/m^{2}K, which is in line with speeds around 12000 rpm [25].

6.1.7 Rotor core

Due to substantial divergences in the rotor design between the different machine topologies, a mutual thermal model for this machine part can not be applied. Therefore, each rotor is modelled individually. However, heat flow in the radial direction only is considered for all models, as for the stator. Furthermore, the rotor models are replaced by equivalent geometries, divided into different sections, in order to simplify the modelling.

6.1.7.1 PMSM

The PMSM rotor geometries with V-shaped PMs are converted into a equivalent model with one arced PM [25]. The equivalent model represents one 8^{th} of the rotor for the 8-pole PMSM, as illustrated in Figure 6.4. Whereas for the 4-pole PMSM, it represents one 4^{th} of the rotor. It is assumed that there exists an air gap $l_{PM,Gap}$ under the PM, with 123 μm thickness, which is a scaled version from [25].

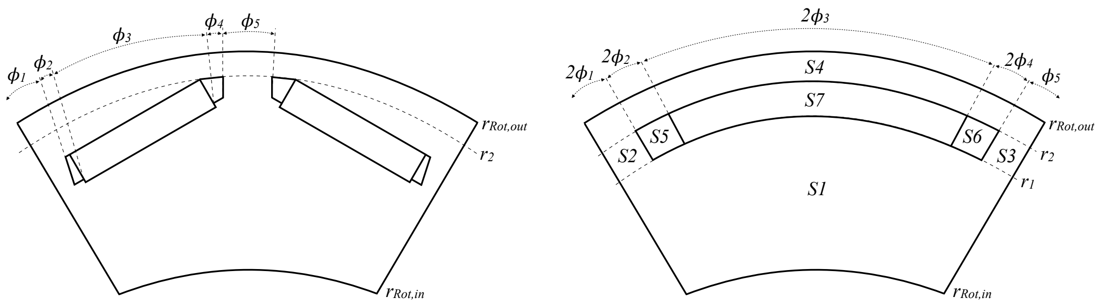

(a) PMSM rotor geometry. (b) Equivalent rotor geometry.

Figure 6.4 PMSM rotor geometry with V-shaped PMs and equivalent rotor geometry with one arced PM.

The equivalent geometries are divided into seven sections with heat flow in the radial direction only [25]. Section S1 and S4 are modelled as hollow cylinders, while section S2, S3, S5-S7 and the small air gap under the PM are modelled as a segment of a hollow cylinder. The section thermal resistances can hence be expressed as

$$R_{th,RoS:1,4} = \frac{ln\left(\frac{r_{out}}{r_{in}}\right)}{2\pi\lambda l_{stk}} \tag{6.35}$$

$$R_{th,RoS:2,3,5-7} = \frac{ln\left(\frac{r_{out}}{r_{in}}\right)}{\phi n_p \lambda l_{stk}} \tag{6.36}$$

where radii (r_{out} and r_{in}) and angles (ϕ) used for the equivalent rotor geometry conversion are presented in Table 6.1. The angles are measured from the machine models in Ansys Maxwell. It is assumed that the heat distribution in section S2, S3 and S5-S7 occur in parallel and that their equivalent thermal resistance is $R_{th,Arc}$ [25].

Table 6.1 Rotor parameters used for the conversion to the equivalent rotor geometry for the 8- and 4-pole PMSM.

	r_{out}	r_{in}	ϕ	λ
$R_{th,RoS1}$	r_1	$r_{Rot,in}$	2π	Iron
$R_{th,RoS2}$	r_2	r_1	$2\phi_1$	Iron
$R_{th,RoS3}$	r_2	r_1	ϕ_5	Iron
$R_{th,RoS4}$	$r_{Rot,out}$	r_2	2π	Iron
$R_{th,RoS5}$	r_2	r_1	$2\phi_2$	Air
$R_{th,RoS6}$	r_2	r_1	$2\phi_4$	Air
$R_{th,RoS7}$	r_2	r_1	$2\phi_3$	Magnet
$R_{th,MagAir}$	$r_1+l_{PM,Gap}$	r_1	$2\phi_3$	Air

The network node for the PMs is located radially in the middle of the arced equivalent PM, and therefore the thermal resistance from the stator teeth node point to the PM node point is expressed as

$$R_{th,StTe-PM} = \frac{1}{2}R_{th,StTe} + R_{th,AirGap} + R_{th,RoS4} + \frac{1}{2}R_{th,Arc} \tag{6.37}$$

Since the network node for the rotor yoke is likewise located radially in the middle of the rotor, the thermal resistance between the PM node point and the rotor yoke node point is found as

$$R_{th,PM-RoYo} = \frac{1}{2}R_{th,Arc} + R_{th,MagAir} + \frac{1}{2}R_{th,RoS1} \tag{6.38}$$

The volume for the thermal capacitance of the PMs is found numerically, meanwhile the volume used to determine the thermal capacitance for the rotor yoke is found by measuring the surface area in Ansys Maxwell and multiplying it with the stack length.

6.1.7.2 SynRM

As for the PMSMs, the SynRM rotor geometry with three air barriers is converted into a equivalent model with one arced air barrier. The equivalent model represents one 4^{th} of the total SynRM rotor geometry, as shown in Figure 6.5.

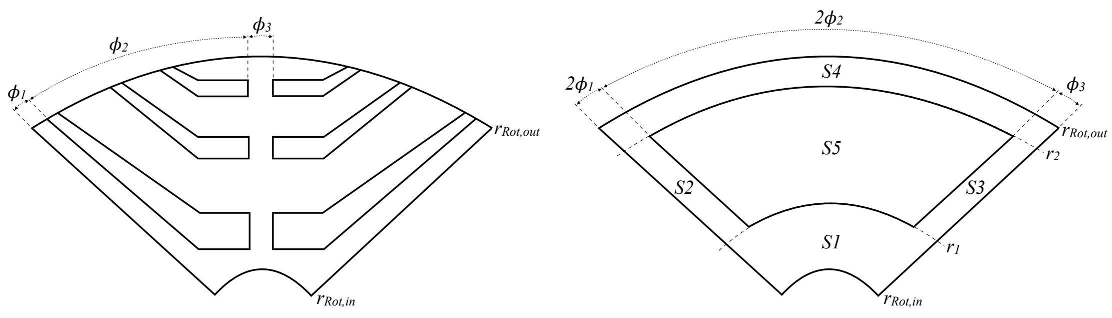

(a) SynRM rotor geometry. (b) Equivalent rotor geometry.

Figure 6.5 SynRM rotor geometry with three air barriers and equivalent rotor geometry with one arced air barrier.

Same procedure is utilized for the SynRM rotor conversion as for the PMSM rotor conversion, but with the magnet section excluded. For simplicity, same radius r_2 is used as for the PMSM. If the arced air barrier section S5, with outer and inner radius r_2 and r_1 respectively, would take the shape of an annulus its area can be found as

$$A_{annulus} = \pi(r_2^2 - r_1^2) \tag{6.39}$$

The arced air barrier section S5 has the same area A_{air} as the three air barriers of the SynRM rotor and is measured in Ansys Maxwell. It can mathematically be expressed as

$$A_{air} = \frac{2\phi_2}{360} A_{annulus} = \frac{2\phi_2}{360} \pi(r_2^2 - r_1^2) \tag{6.40}$$

Accordingly, the inner radius r_1 of the arced air barrier can be calculated as

$$r_1 = \sqrt{r_2^2 - \frac{A_{air}}{\phi_2}} \tag{6.41}$$

Thermal resistances for the different sections are calculated according to (6.35) and (6.36). Radii, angles and materials used for thermal conductivity are presented in Table 6.2. It is furthermore assumed that the heat distribution in section S2, S3 and S5 occur in parallel and that their equivalent thermal resistance is $R_{th,Arc}$.

Table 6.2 Rotor parameters used for the conversion to the equivalent rotor geometry for the SynRM.

	r_{out}	r_{in}	ϕ	λ
$R_{th,RoS1}$	r_1	$r_{Rot,in}$	2π	Iron
$R_{th,RoS2}$	r_2	r_1	$2\phi_1$	Iron
$R_{th,RoS3}$	r_2	r_1	ϕ_3	Iron
$R_{th,RoS4}$	$r_{Rot,out}$	r_2	2π	Iron
$R_{th,RoS5}$	r_2	r_1	$2\phi_2$	Air

The network node point for the rotor yoke is located radially in the middle of section S1, and hence the thermal resistance from the stator teeth node point to the rotor yoke node point is expressed as

$$R_{th,StTe-RoYo} = \frac{1}{2} R_{th,StTe} + R_{th,AirGap} + R_{th,RoS4} + R_{th,Arc} + \frac{1}{2} R_{th,RoS1} \tag{6.42}$$

6.1.7.3 PMSynRM

The rotor geometry of the PMSynRM has the design of the SynRM and the characteristics of the PMSMs. The equivalent rotor model can hence be represented as a combination of them both. As presented in Figure 6.6, it has the appearance of the equivalent SynRM rotor model, where the three air barriers are converted into one arced air barrier, whereas the PMs are converted into one arced PM.

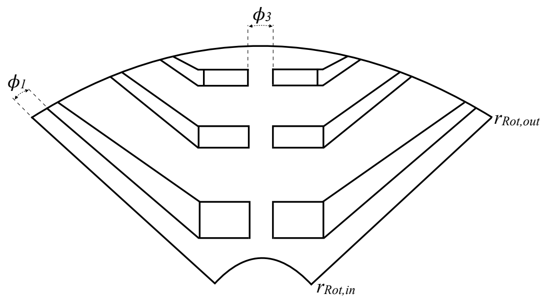

(a) PMSynRM rotor geometry.

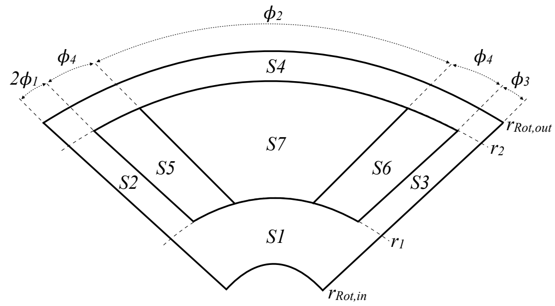

(b) Equivalent rotor geometry.

Figure 6.6 PMSynRM rotor geometry with three air barriers and equivalent rotor geometry with one arced air barrier.

The PM area is measured in Ansys Maxwell and from it the angles ϕ_2 and ϕ_4 can be calculated. Thermal resistances for all the sections in the equivalent rotor model are calculated according to (6.35) and (6.36). Heat distribution in S2, S3 and S5-S7 are assumed to occur in parallel and that their equivalent thermal resistance is $R_{th,Arc}$. Radii, angles and materials used for thermal conductivity are presented in Table 6.3.

Table 6.3 Rotor parameters used for the conversion to the equivalent rotor geometry for the PMSynRM.

	r_{out}	r_{in}	ϕ	λ
$R_{th,RoS1}$	r_1	$r_{Rot,in}$	2π	Iron
$R_{th,RoS2}$	r_2	r_1	$2\phi_1$	Iron
$R_{th,RoS3}$	r_2	r_1	ϕ_3	Iron
$R_{th,RoS4}$	$r_{Rot,out}$	r_2	2π	Iron
$R_{th,RoS5}$	r_2	r_1	ϕ_4	Air
$R_{th,RoS6}$	r_2	r_1	ϕ_4	Air
$R_{th,RoS7}$	r_2	r_1	ϕ_2	Ferrite magnet

As for the PMSMs, the network node for the PMSynRM is placed radially in the middle of the equivalent arced PM, and therefore the thermal resistance between the stator teeth node point and the PM node point can be calculated according to (6.37). Since no air gap is assumed to exist around the PMs, the thermal resistance from the PM node point to the rotor yoke node point is found as

$$R_{th,PM-RoYo} = \frac{1}{2}R_{th,Arc} + \frac{1}{2}R_{th,RoS1} \tag{6.43}$$

6.1.8 Shaft

It is assumed that only conductive heat flow in the axial direction is present in the machine shaft, and that it is a lossless part with homogeneous temperature distribution. Since the shaft consists of two regions with different shaft radius, so will its thermal resistance, as in [25]

$$R_{th,Sh} = \frac{l_{stk}}{\pi r_{RoYo,in}^2 \lambda_{Steel}} + \frac{2l_{Sh,ext}}{\pi r_{Sh,ext}^2 \lambda_{Steel}} \tag{6.44}$$

where the first part along the lamination stack has a radius equal to the rotor yoke inner radius $r_{RoYo,in}$, and the second part between the lamination stack and the bearings has a radius $r_{Sh,ext}$ of 16.4 mm for the PMSMs [25] and equal to the rotor yoke inner radius for SynRM and PMSynRM. The length to the bearings outside the lamination stack $l_{Sh,ext}$ is 36.9 mm on both sides for all the machine topologies and the thermal conductivity for the shaft steel material λ_{Steel} is 51.9 W/mK.

The thermal capacitance of the shaft is neglected for all machine topologies, since it has very limited impact on the temperature in neighbouring machine parts [25].

6.1.9 Bearings

With an average bearing diameter d_b of 44.3 mm, the bearing thermal resistance can be determined from [25]

$$R_{th,Be} = 0.45 \cdot 33(0.12 - d_b) \tag{6.45}$$

Power losses in the bearings are dependent on the machine torque T_e and the angular speed ω_r, as in

$$P_{Be} = \frac{r_{Be}\mu_{Be}T_e\omega_r}{r_{Rot,out}} \tag{6.46}$$

where r_{Be} is the bearing bore radius which is equal to $r_{Sh,ext}$, and μ_{Be} is the bearing friction coefficient which is assumed to be equal to 0.0015 [25]. The thermal contact resistance between the rotor yoke and the shaft is modelled as a hollow cylinder consisting of a 10 μm thick air film $l_{contRoYo-Sh}$, and can can hence be written as

$$R_{th,contRoYo-Sh} = \frac{ln\left(\frac{r_{Rot,in}+l_{contRoYo-Sh}}{r_{Rot,in}}\right)}{2\pi\lambda_{Air}l_{stk}} \tag{6.47}$$

The thermal resistance from the bearing node point to the stator frame point in the thermal network can then be calculated as [33]

$$R_{th,Be-Fr} = \frac{1}{4}R_{th,Be} \tag{6.48}$$

and the thermal resistance between the bearing node point and the rotor yoke node point can be determined from

$$R_{th,Be-RoYo} = \frac{1}{2}R_{th,RoS1} + R_{th,contRoYo-Sh} + \frac{1}{2}R_{th,Sh} + \frac{1}{4}R_{th,Be} \tag{6.49}$$

The thermal capacitance of the bearings is found by assuming that the specific heat constant for the bearings is the same as for the shaft material, and that its mass is a scaled version from [25].

6.1.10 Summary of thermal resistances and capacitances

The resulting thermal network resistances (W/mK) and capacitances (J/K) are presented in Table 6.4 and 6.5 respectively, for all considered machine topologies. For each individual machine, the values are determined at nominal speed, at 65°C coolant temperature and at a flow rate of 6 L/min.

Table 6.4 Resulting thermal network resistances (W/mK), for the PMSMs, SynRM and PMSynRM.

	PMSM 8-pole	**PMSM 4-pole**	**SynRM**	**PMSynRM**
$R_{th,Co-Fr}$	0.0050	0.0050	0.0050	0.0050
$R_{th,Fr-StYo}$	0.0121	0.0133	0.0146	0.0146
$R_{th,StYo-StTe}$	0.0215	0.0225	0.0257	0.0257
$R_{th,StTe-ActWi}$	0.0461	0.0526	0.0526	0.0526
$R_{th,ActWi-EndWi}$	0.0511	0.0657	0.0643	0.0643
$R_{th,RoYo-Fr}$	0.3871	0.4073	0.4316	0.4316
$R_{th,EndWi-RoYo}$	2.0933	1.4867	1.7033	1.7033
$R_{th,EndWi-Fr}$	1.0872	0.7722	0.8029	0.8029
$R_{th,StTe-PM}$	0.3006	0.3005	-	0.8855
$R_{th,PM-RoYo}$	0.2339	0.2339	-	0.6181
$R_{th,StTe-RoYo}$	-	-	0.4516	-
$R_{th,Be-Fr}$	0.2811	0.2811	0.2970	0.2970
$R_{th,Be-RoYo}$	1.3828	1.3828	5.1227	5.1227

Table 6.5 Resulting thermal network capacitances (J/K), for the PMSMs, SynRM and PMSynRM.

	PMSM 8-pole	**PMSM 4-pole**	**SynRM**	**PMSynRM**
$C_{th,Fr}$	537	703	686	686
$C_{th,StYo}$	1539	1909	2303	2303
$C_{th,StTe}$	1234	863	777	777
$C_{th,ActWi}$	408	408	408	408
$C_{th,EndWi}$	521	787	761	761
$C_{th,PM}$	434	434	-	343
$C_{th,RoYo}$	1702	1709	471	471
$C_{th,Be}$	146	146	102	102

6.2 Losses in machine parts

Power loss components for the whole operating region in motoring mode for the examined machines are presented in Figure 6.7-6.10. Losses include stator lamination losses in yoke and teeth regions, resistive losses in stator active and end windings, rotor lamination losses and bearing losses. Losses in PMs are included for the PMSMs. Since the ferrite magnets in the PMSynRM were assumed to be a lossless component, they are not included. The results are extracted from the FEM simulations, and are used as input data for the lumped-parameter network models in Figure 6.1 and 6.2.

The most dominant losses for all machine topologies are the winding losses. whereas most of the losses occur in the end windings. This shows the great importance of not only considering the active length of the windings, especially for machines with low length and high diameter ratio. The 4-pole PMSM, SynRM and PMSynRM have a stator winding distribution similar to each other, which also reflects the stator winding losses. The winding losses for the 8-pole PMSM are however significantly lower compared to the other machines. One reason could be the length of the winding pole pitch, which in a 8-pole machine is half the length compared to in a 4-pole machine with equal stator inner diameter. The resistive losses in the windings are dependent in the square of the current magnitude, which makes them very torque dependent. Since the winding losses are significantly lower for the 8-pole PMSM, it requires less current in order to reach a certain torque level compared to the other machines. One could argue that this is not only an advantage in terms of low power losses, but also an advantage regarding the system components connected to the machine such as the power inverter and electric cables. If less current is required, the power rating of these components can be restrained and thus also the costs.

The stator and rotor lamination losses are foremost speed dependent. Some torque dependence exist, especially at high speed and low torque levels. The power losses in the rotor lamination are relatively low and hence most of the losses occur in the stator lamination, where the majority are located in the stator teeth region for the PMSMs and in the stator yoke region for the SynRM and PMSynRM.

The PM losses for the PMSMs are low compared to the losses in windings and lamination, and have thus low impact on the overall operating machine efficiency. To neglect the losses in the ferrite magnets for the PMSynRM can hence be seen as a valid assumption. The PM losses in the 4-pole PMSM are somewhat higher than the rotor lamination losses. The bearing losses are very low compared to the overall losses, especially for the SynRM and the PMSynRM due their short shaft diameter.

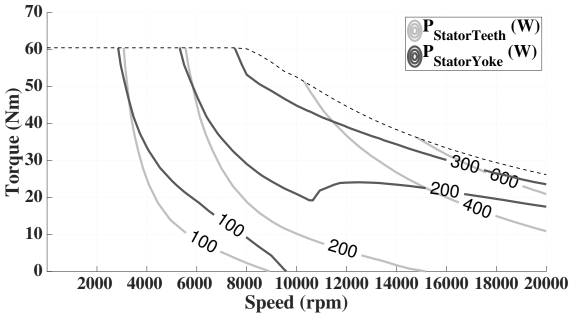

(a) Stator lamination losses.

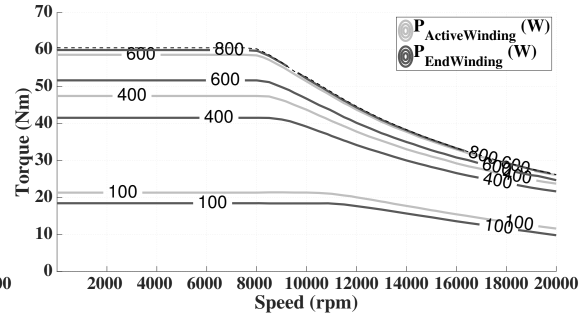

(b) Winding losses.

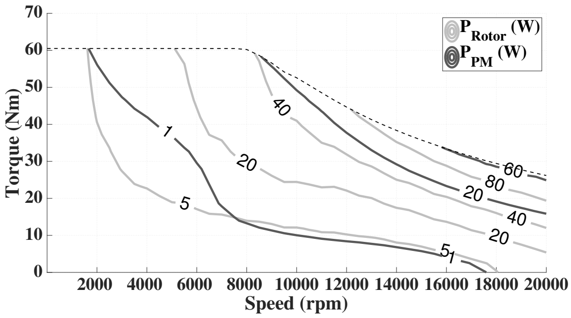

(c) Rotor lamination and PM losses.

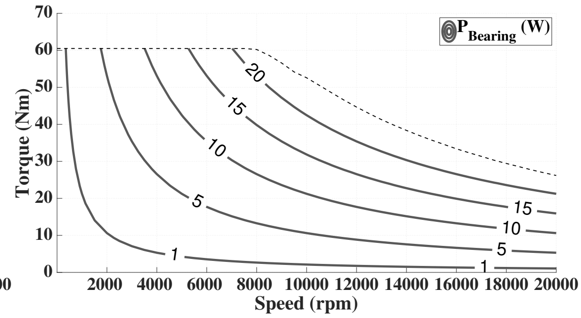

(d) Bearing losses.

Figure 6.7 Machine part losses as a function of torque and speed, for the 8-pole PMSM.

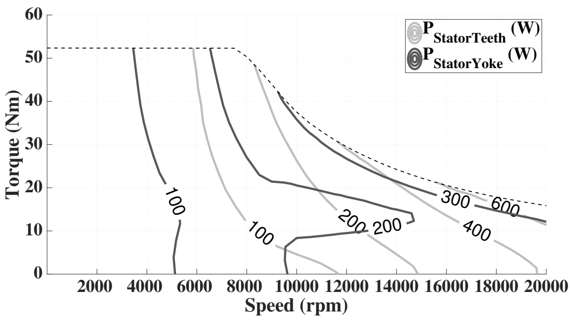

(a) Stator lamination losses.

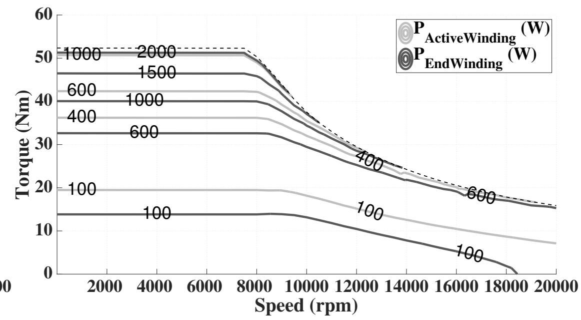

(b) Winding losses.

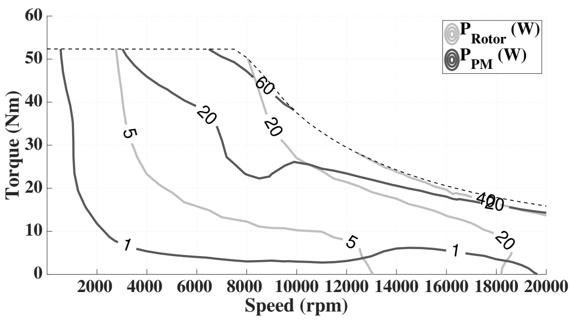

(c) Rotor lamination and PM losses.

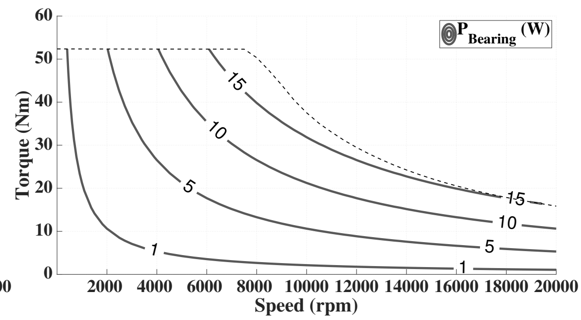

(d) Bearing losses.

Figure 6.8 Machine part losses as a function of torque and speed, for the 4-pole PMSM.

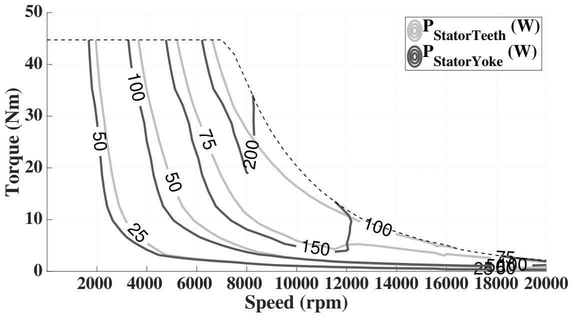

(a) Stator lamination losses.

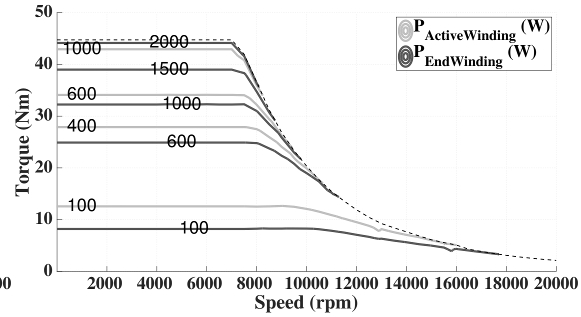

(b) Winding losses.

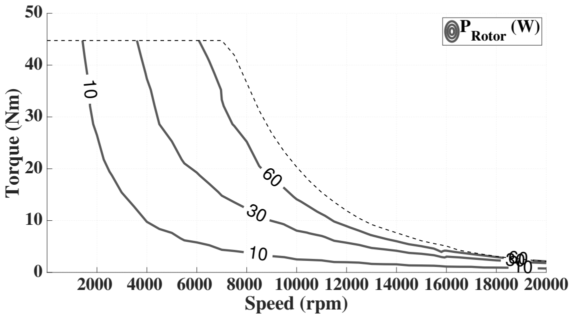

(c) Rotor lamination losses.

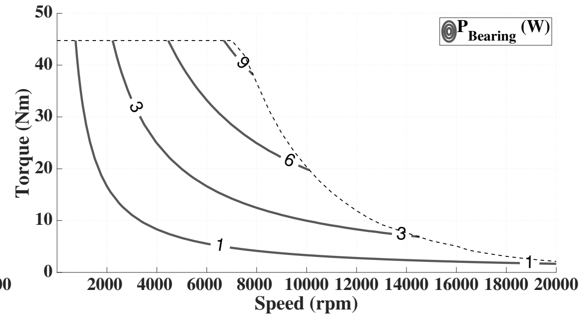

(d) Bearing losses.

Figure 6.9 Machine part losses as a function of torque and speed, for the SynRM.

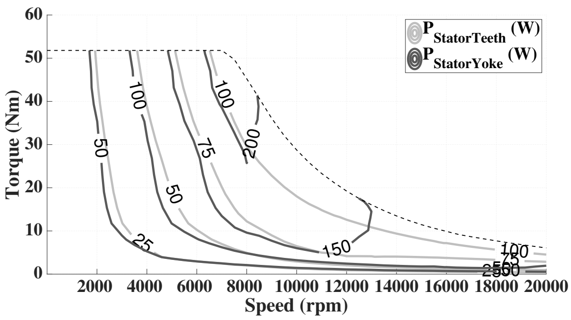

(a) Stator lamination losses.

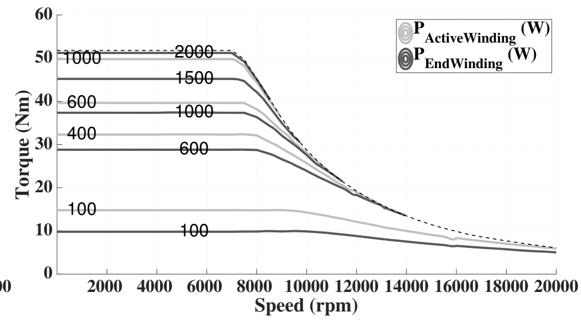

(b) Winding losses.

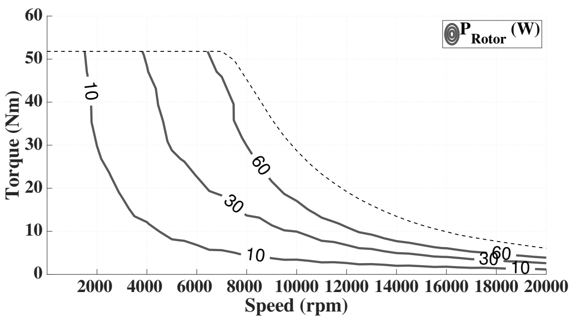

(c) Rotor lamination losses.

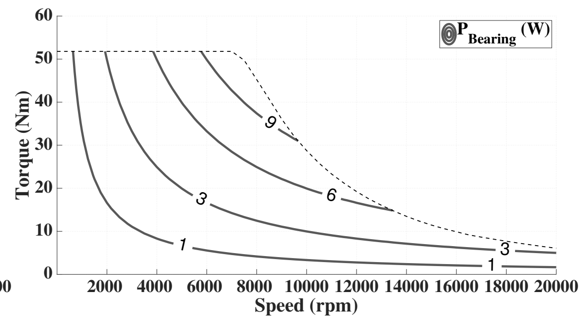

(d) Bearing losses.

Figure 6.10 Machine part losses as a function of torque and speed, for the PMSynRM.

6.3 Transient thermal response comparison

To investigate the thermal characteristics of the machine parts and the thermal distribution between them, two different load steps of 10 kW and 20 kW at nominal speeds have been examined. The power losses at the specific operating points are added to the lumped-parameter network models in Figure 6.1 and 6.2, at coolant temperature of 65°C and a flow rate of 6 L/min. The results are presented in Figure 6.11-6.14.

The machines are supposed to be able to generate 10 kW continuously in a mild hybrid system, and hence they should withstand this thermally. During short time intervals, the machines should be able to provide a peak power of 20 kW. Hence these are the operating points of interest to investigate. The rare-earth magnets in the PMSMs has a thermal capability of maximum 140°C, whereas the critical thermal limit for the stator windings is 150°C [25].

Since most power losses occur in the stator windings, the temperature response is highest in that region for all machines. The length of the end windings are longer than the stack length, especially in the 4-pole PMSM, SynRM and PMSynRM, and thus this component will have the highest temperature during continuous operation. The temperature in machine parts with significant power losses and located near the stator windings also increases substantially at a load step, such as the stator teeth region. Machine parts such as the frame and the stator yoke are located closest to the cooling system and thus only have a small variation from the coolant temperature of 65°C during continuous operation.

The 8-pole PMSM has the most satisfying thermal response, both at 10 kW and 20 kW. The end windings reach a steady state temperature 92°C and 125°C respectively, after around 15 min continuous operation. Even though it is not likely that it will need to operate at 20 kW continuously in a mild hybrid system, the machine still has the thermal capability to do it. The steady state temperature of the PMs are 82°C and 94°C respectively, which is below the critical limit of 140°C. The thermal characteristics when the load step goes off resembles the characteristics when the load step goes on. It can thus be concluded that the 8-pole PMSM has satisfying thermal response and fulfills the requirements.

The thermal characteristics of the 4-pole PMSM resembles the ones for the 8-pole PMSM. The stator winding and PM temperatures are below the critical limits and it can run continuously both at 10 kW and 20 kW. The temperature in the end windings are somewhat higher than for the 8-pole PMSM, since it requires more current at this level of output power.

For the SynRM, the temperature of the end windings reaches a steady state value of 116°C at 10 kW continuous operation which is below the critical limit. However, for continuous operation at 20 kW the temperature in the end and active windings reach 240°C and 195°C, respectively. It though requires that the SynRM runs continuously at 20 kW for at least 2 min, which for the probability to occur can be regarded low. Similar characteristics can be seen for the PMSynRM. It can run continuously at 10 kW without exceeding the critical limits, but at 20 kW the end windings exceeds 150°C after approximately 3 min.

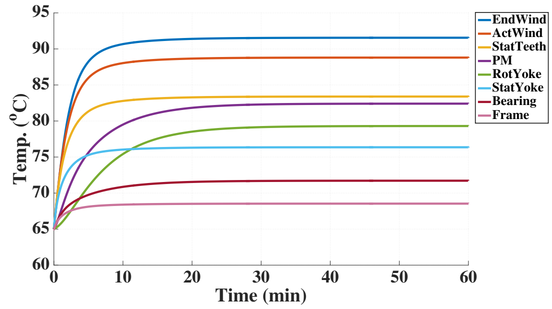

(a) 10 kW load step on.

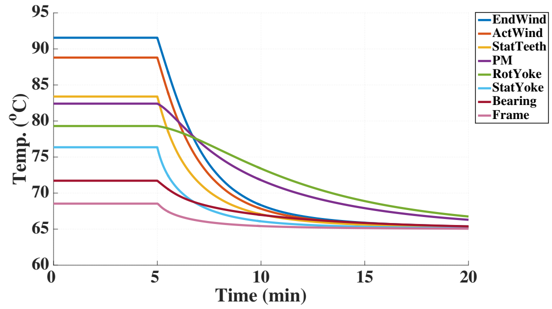

(b) 10 kW load step off.

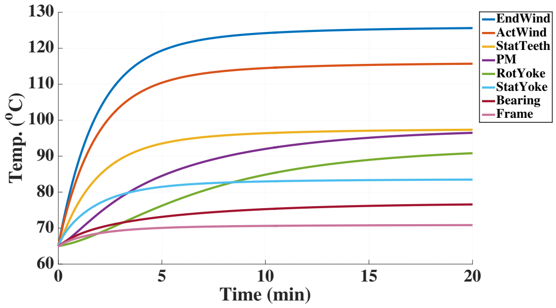

(c) 20 kW load step on.

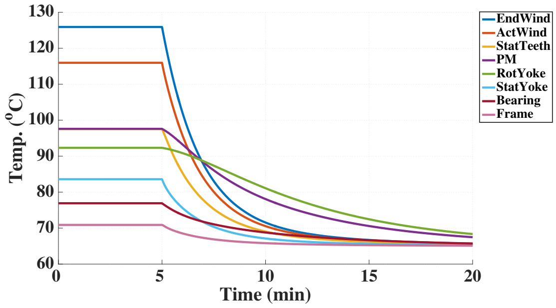

(d) 20 kW load step off.

Figure 6.11 Temperature characteristics as a function of time for the 8-pole PMSM, during load steps of 10 kW and 20 kW at nominal speed of 7800 rpm.

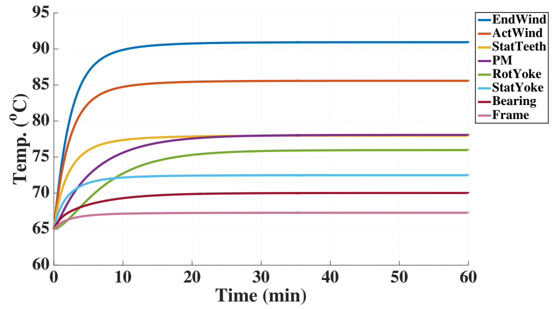

(a) 10 kW load step on.

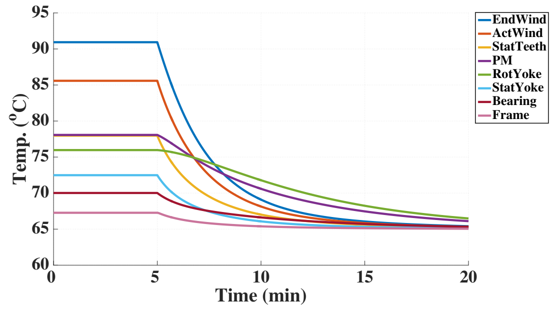

(b) 10 kW load step off.

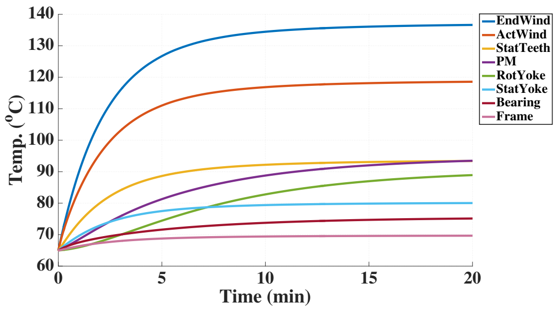

(c) 20 kW load step on.

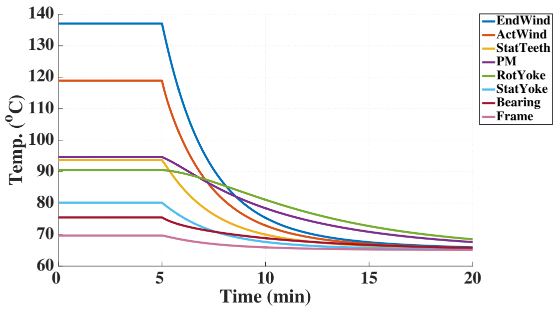

(d) 20 kW load step off.

Figure 6.12 Temperature characteristics as a function of time for the 4-pole PMSM, during load steps of 10 kW and 20 kW at nominal speed of 7400 rpm.

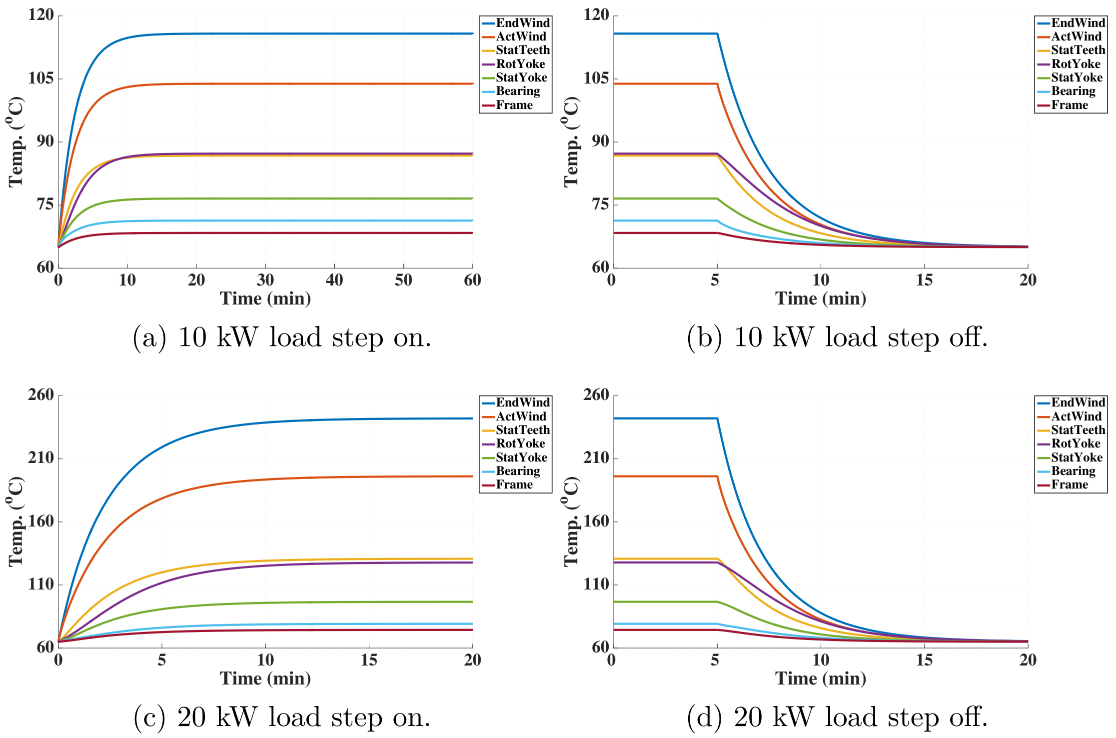

(a) 10 kW load step on.

(b) 10 kW load step off.

(c) 20 kW load step on.

(d) 20 kW load step off.

Figure 6.13 Temperature characteristics as a function of time for the SynRM, during load steps of 10 kW and 20 kW at nominal speed of 7000 rpm.

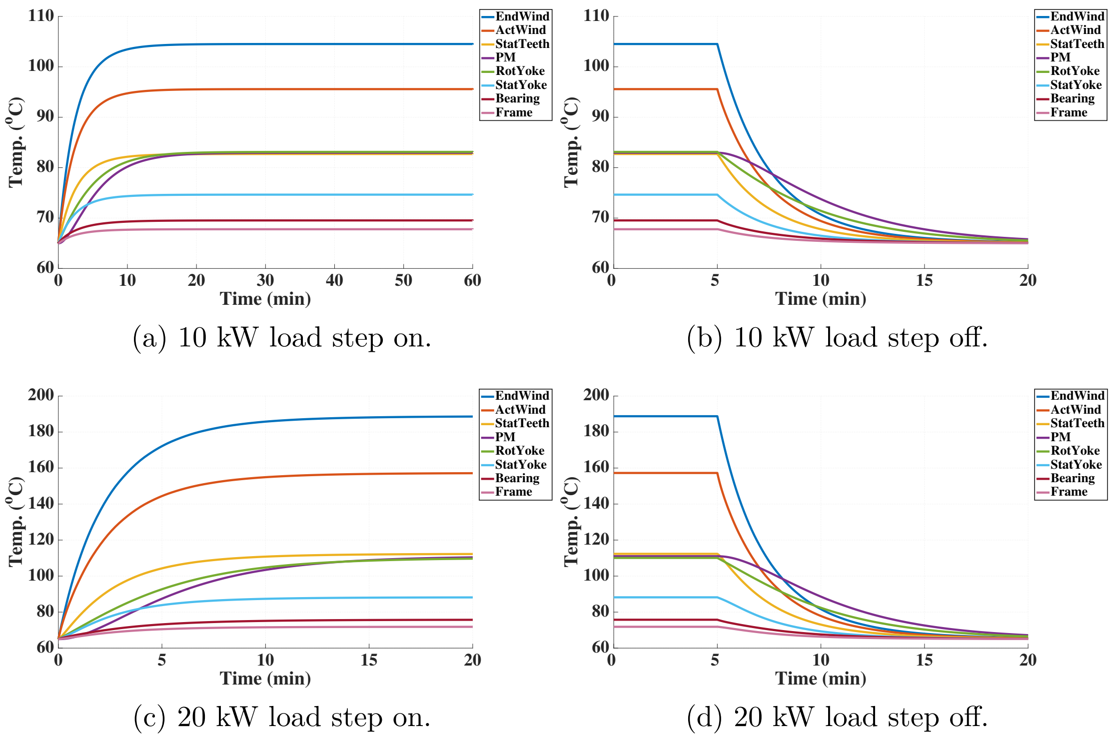

(a) 10 kW load step on.

(b) 10 kW load step off.

(c) 20 kW load step on.

(d) 20 kW load step off.

Figure 6.14 Temperature characteristics as a function of time for the PMSynRM, during load steps of 10 kW and 20 kW at nominal speed of 7100 rpm.

7
Conclusions and Future Work

7.1 Conclusions

In this work, various electric machine topologies have been modeled in electromagnetic field software and through FEM simulations analyzed in terms of performance characteristics and thermal response. The results have been utilized in full vehicle simulations where the machines have been evaluated when they are implemented in a mild hybrid system. Furthermore, a thermal evaluation was conducted in order to investigate the temperature distribution within the machines. For this study, two PMSMs, a SynRM, a PMSynRM and an IM were chosen to be examined. A reference PMSM from the Toyota Prius 2004 [35] was optimized and scaled according to geometrical dimensions, which resulted in a machine with 80 mm stack length and 165 mm stator outer diameter. The stator of this PMSM was later used as reference for the additional machine topologies. It was chosen that the machines should fulfill performance requirements such as a cold crank torque of 55 Nm and 10 kW continuous operation at nominal speed.

The objective of the FEM simulations was to establish efficiency maps in both motoring and generation mode for the whole operating region between 0-20000 rpm, as well as information about maximum torque, peak power and characteristics of power losses. The results show that the 8-pole PMSM has the highest operating efficiency 96.9 % of all studied machines. This is mainly a consequence of the high output power generation and low resistive losses in the stator windings. The operating regions with highest efficiency are located in the field weakening region, for all machines. The implemented ferrite magnets of the PMSynRM increase the highest operating efficiency of the SynRM by 1 % and raise the maximum torque by 7 Nm, which is considered as a satisfying improvement. The 8-pole PMSM and the IM fulfill the cold crank torque requirement. The FEM simulations were very extensive and time-consuming, and hence the IM has only been investigated in the constant torque region below nominal speed.

The most frequent operating point of an ISG implemented in a mild hybrid system was concluded to occur at 4600 rpm and 1 kW, for which the 8-pole PMSM have the highest operating efficiency of 94.5 %. All machines can easily provide 2.5 kW at a speed of 2000 rpm. Furthermore, the 8-pole PMSM has the highest power density of 19.67 kW/dm^3, while the IM has the highest torque density of 23.67 Nm/dm^3. Due to the low weight of the PMSynRM and overall beneficial performance numbers, it has the highest specific torque of 5.26 Nm/kg together with the 8-pole PMSM. The PMSynRM is further one of the best options when comparing material costs and CO_2 equivalent per kilo produced material.

Data from the FEM simulations have been utilized in full vehicle simulations for a mild hybrid system with P0 topology. Operating points for an ISG during two types of drive cycles, one highway drive and one city drive, were implemented in the efficiency maps for respective machine. The resulting machine rms efficiency are rather similar for the highway 89.5-92.5 % and city drive cycle 87.4-90.3 %. The 8-pole PMSM has the highest rms efficiency for both drive cycles, whereas the SynRM has the lowest. It was concluded that the operating points of the ISG does not fully intersect with the operating regions with highest efficiency, for neither of the machines and nor of the drive cycles. If a higher transmission ratio could be utilized, it would most probably improve the overall performance substantially.

Power losses in different machine parts at 10 kW and 20 kW for nominal speed have been used as input data for the thermal model. The results show that both the 8- and 4-pole PMSM can operate 10 kW and 20 kW continuously without exceeding the critical limits of 150°C for the stator windings and 140°C for the PMs. The SynRM and PMSynRM can provide 10 kW of power continuously at nominal speed, but at 20 kW the windings exceed 150°. However, this occurs after 2-3 min of continuous operation and it is expected that the machines only should provide a peak power of 20 kW during short time intervals. The dominant power losses occurs in the end windings, which is expected for machines with low length and high diameter ratio. Iron losses are relatively low compared to the winding losses, especially in the rotor lamination, and hence the assumption of lossless ferrite magnets for the PMSynRM is considered as valid.

Due to advantageous properties such as high power and torque density, satisfying operating efficiency and promising thermal response, makes the PMSM topology an interesting option to be utilized in mild hybrid traction applications. However, the PMs are sensitive for irreversible demagnetization and are compounded by rare-earth materials. The PMSynRM with ferrite magnets could also be considered an interesting option due to its overall high performance in relation to its low material costs and CO_2 equivalent per kilo produced material.

7.2 Future work

Since the IM is a commonly utilized machine topology for traction vehicle applications, it would be interesting to further analyze its operating characteristics and performance to the same extent as for the PMSM, SynRM and PMSynRM. It is partially evaluated in the constant torque region below nominal speed, but its performance in the field weakening region needs to studied more thoroughly. An accurate thermal evaluation of the machine would most probably be necessary to conduct, since high temperatures can emerge in the rotor of the IM due to resistive losses in the current carrying rotor bars.

One could argue that the P2 topology is one of the mild hybrid system topologies of highest interest, due its wide range of hybrid applications. To study the machines when operating in a P2 mild hybrid system would be valuable in order to evaluate hybrid functions such as coasting and pure electric traction at low vehicle speeds. The thermal characteristics of the machines have in this work been evaluated in two operating points. If all operating points from a real-world drive cycle are implemented in the thermal models, a more realistic thermal response can be obtained. The transmission ratio could further be optimized in order for the operating points to completely intersect with the operating regions of highest efficiency.

Furthermore, the electric machines have in this study been evaluated during two types of drive cycles, i.e. during highway and city driving. It would be interesting to investigate the machines at several types of driving cycles during various circumstances, such as climate conditions and traffic situations, so that a more accurate and comprehensive comparison can be achieved. The performance results should be related to impacts in CO_2 emissions, since this is one of the largest driving forces to the increasing vehicle electrification. Therefore, is it also of great importance to include other environmental aspects related to electric machines such as extraction of raw materials, large-scale manufacturing, life cycle costs and recycling in future studies.

Moreover, the machine designs have in this study only been optimized to some basic extent. It would be interesting to thoroughly optimize each machine topology and customize them for certain operation points in a mild hybrid application. For example, winding distribution, slot- and pole combinations and choice of material would be valuable to evaluate. Finally, future studies should involve other components of the power supply such as the power inverter and the energy storage system, since they are obviously vital parts in the mild hybrid system.

Bibliography

[1] The European Commission, "Greenhouse gas emission statistics," 2016. [Online]. Available: http://ec.europa.eu/eurostat/statistics-explained/index.php/Greenhouse_gas_emission_statistics. Accessed: 2017-01-20.

[2] The European Commission, "Reducing CO2 emissions from passenger cars," 2017. [Online]. Available: http://ec.europa.eu/clima/policies/transport/vehicles/cars_en. Accessed: 2017-01-20.

[3] M. Kuypers, "Application of 48 Volt for Mild Hybrid Vehicles and High Power Loads," SAE Technical Paper 2014-01-1790, 2014, doi:10.4271/2014-01-1790.

[4] I. Boldea, L. N. Tutelea, L. Parsa, and D. Dorrell, "Automotive Electric Propulsion Systems With Reduced or No Permanent Magnets: An Overview," *IEEE Trans. Ind. Electr.*, vol. 61, no. 10, pp. 5696-5711, Oct. 2014.

[5] L.R. Huang, Z.Q. Zhu, and W.Q. Chu, "Optimization of Electrically Excited Synchronous Machine for Electrical Vehicle Applications," *8th IET International Conference on Power Electronics, Machines and Drives (PEMD)*, Apr. 2016.

[6] Z. Yang, F. Shang, I. P. Brown, and M. Krishnamurthy, "Comparative Study of Interior Permanent Magnet, Induction, and Switched Reluctance Motor Drives for EV and HEV Applications," *IEEE Trans. Transport. Electrific.*, vol. 1, no. 3, pp. 245-254, Oct. 2015.

[7] M. Zeraoulia, M. E. H. Benbouzid, and D. Diallo, "Electric Motor Drive Selection Issues for HEV Propulsion Systems: A Comparative Study," *IEEE Trans. Veh. Technol.*, vol. 55, no. 6, pp. 1756-1764, Nov. 2006.

[8] D. Bucherl, R. Nuscheler, W. Meyer, and H. G. Herzog, "Comparison of Electrical Machine Types in Hybrid Drive Trains: Induction Machine vs. Permanent Magnet Synchronous Machine," *18th International Conference on Electrical Machines (ICEM)*, Sep. 2008.

[9] C. S. Kim *et al.*, "48V Power Assist Recuperation System (PARS) with a permanent magnet motor, inverter and DC-DC converter," *1st International Future Energy Electronics Conference (IFEEC)*, Nov. 2013.

[10] X. Chen, and S. Shen, "Comparison of Two Permanent-Magnet Machines for a Mild Hybrid Electric Vehicle Application," SAE Technical Paper 2008-01-1552, 2008, doi:10.4271/2008-01-1552.

[11] N. Zhao, and N. Schofield, "An Improved Induction Machine Design Procedure for Electric Vehicle Traction," *8th IET International Conference on Power Electronics, Machines and Drives (PEMD)*, Apr. 2016.

[12] L. Chen, J. Wang, P. Lombard, P. Lazari, and V. Leconte, "Design optimisation of permanent magnet assisted synchronous reluctance machines for electric vehicle applications," *International Conference on Electrical Machines (ICEM)*, Nov. 2012.

[13] T. Finken, M. Felden, and K. Hameyer, "Comparison and design of different electrical machine types regarding their applicability in hybrid electrical vehicles," *18th International Conference on Electrical Machines (ICEM)*, Sep. 2008.

[14] G. Bailey, N. Mancheri, and K. Van Acker, "Sustainability of Permanent Rare Earth Magnet Motors in (H)EV Industry," *Journal of Sustainable Metallurgy*, vol. 3, pp 1-16, Mar. 2017.

[15] J. Junak, "Development of vehicle drivetrain and its components - solutions for CO_2 reduction," *International Conference on Sustainable Mobility Applications, Renewables and Technology (SMART)*, Nov. 2015.

[16] S. A. Fayazi, S. Farhangi, and B. Asaei, "Fuel Consumption and Emission Reduction of a Mild Hybrid Vehicle," *34th Annual Conference of IEEE Industrial Electronics (IECON)*, Nov. 2008.

[17] R.-P. Hangiu, A.-T. Filip, C. S. Martis, and K. A. Biro, "Performance Assessment of an Integrated Starter Alternator for Hybrid Electric Vehicles," *International Conference and Exposition on Electrical and Power Engineering (EPE)*, Oct. 2012.

[18] F. Millo, M. Badami, C. Ferraro, and L. Rolando, "Different Hybrid Powertrain Solutions for European Diesel passenger cars," *SAE Int. J. Engines* 2(2):493-504, 2010, doi:10.4271/2009-24-0064.

[19] A. Boglietti, R. Bojoi, A. Cavagnino, M. Cossale, and A. Tenconi, "Analysis of Different Forced Convection Cooling Systems for Belt-Driven Starter-Generator," *41st Annual Conference of IEEE Industrial Electronics (IECON)*, Nov. 2015.

[20] A. Cavagnino, M. Cossale, A. Tenconi, and S. Vaschetto, "Prototyping Experiences on 48V Starter-Alternators," *International Conference on Electrical Machines (ICEM)*, Sep. 2016.

[21] A. K. Jain, S. Mathapati, V. T. Ranganathan, and V. Narayanan, "Integrated Starter Generator for 42-V Powernet Using Induction Machine and Direct Torque Control Technique," *IEEE Trans. Power Electron.*, vol. 21, no. 3, pp. 701–710, May 2006.

[22] K. T. Chau, *Electric Vehicle Machines and Drives: Design, Analysis and Application,* Singapore: John Wiley & Sons - IEEE Press, 2015.

[23] C. Liu, K. T. Chau, and J. Z. Jiang, "A Permanent-Magnet Hybrid Brushless Integrated Starter–Generator for Hybrid Electric Vehicles," *IEEE Trans. Ind. Electron.*, vol. 57, no. 12, pp. 4055–4064, Dec. 2010.

[24] P. Tokat, "Design and Evaluation of a Permanent Magnet Generator for Wave Power Applications," Thesis for the degree of Licentiate of Engineering, Chalmers University of Technology, 2015. [Online]. Available: http://publications.lib.chalmers.se/records/fulltext/217403/217403.pdf.

[25] E. Grunditz, "Design and Assessment of Battery Electric Vehicle Powertrain, with Respect to Performance, Energy Consumption and Electric Motor Thermal Capability," Thesis for the degree of Doctor of Philosophy in Engineering, Chalmers University of Technology, 2016. [Online]. Available: http://publications.lib.chalmers.se/records/fulltext/236616/236616.pdf.

[26] A. Rabiei, "Energy Efficiency of an Electric Vehicle Propulsion Inverter Using Various Semiconductor Technologies," Thesis for the degree of Licentiate of Engineering, Chalmers University of Technology, 2013. [Online]. Available: http://publications.lib.chalmers.se/records/fulltext/187097/187097.pdf.

[27] R. Rajabi Moghaddam, "Synchronous Reluctance Machine (SynRM) in Variable Speed Drives (VSD) Applications," Thesis for the degree of Doctor of Philosophy in Engineering, Royal Institute of Technology, 2011. [Online]. Available: http://www.diva-portal.org/smash/get/diva2:417890/FULLTEXT01.pdf.

[28] M. J. Kamper, and A. F. Volschenk, "Effect of rotor dimensions and cross magnetisation on L_d and L_q inductances of reluctance synchronous machine with cageless flux barrier rotor," *Electric Power Applications, IEE Proceedings B*, vol. 141, no. 4, pp. 213–220, Jul. 1994.

[29] A. E. Fitzgerald, C. Kingsley Jr and S. D. Umans, *Electrical Machinery,* 6th ed. United States of America: McGraw-Hill, 2003.

[30] F. Incropera, D. Dewitt, T. Bergman, and A. Lavine, *Fundamentals of Heat and Mass Transfer,* 7th ed. United States of America: John Wiley & Sons, 2011.

[31] P. Mellor, D. Roberts, and D. Turner, "Lumped parameter thermal model for electrical machines of TEFC design," *Electric Power Applications, IEE Proceedings B*, vol. 138, no. 5, pp. 205–208, Sep. 1991.

[32] S. Skoog, "Experimental and model based evaluation of mild hybrid fuel consumption gains and electric machine utilization for personal vehicle application," *IEEE Conference and Expo on Transportation Electrification Asia-Pacific (ITEC Asia-Pacific)*, 2017.

[33] J. Lindström, "Development of an Experimental Permanent-Magnet Motor Drive," Thesis for the degree of Licentiate of Engineering, Technical Report No. 312L, Chalmers University of Technology, 1999.

[34] O. Josefsson, "Energy Efficiency Comparison Between Two-level and Multilevel Inverters for Electric Vehicle Applications," Thesis for the degree of Licentiate of Engineering, Chalmers University of Technology, 2013. [Online]. Available: http://publications.lib.chalmers.se/records/fulltext/174182/174182.pdf.

[35] Ansoft Maxwell Field Simulator, (2011) "Study of a permanent magnet motor with MAXWELL 20: Example of the 2004 Prius IPM Motor", Tutorial example from Ansoft Maxwell, accessed 2011.

[36] D. Staton, A. Boglietti, and A. Cavagnino, "Solving the more difficult aspects of electric motor thermal analysis in small and medium size industrial induction motors," *IEEE Trans. Energy. Convers.*, vol. 20, no. 3, pp. 620–628, Aug. 2005.

[37] M. Humphries, “Rare Earth Elements: The Global Supply Chain,” *Congressional Research Service*, Dec. 2013.

[38] D. Tanaka, M. Sanada, S. Morimoto, and Y. Inoue, "Comparison of IPMSMs Using Bonded and Sintered Rare-Earth Magnets with Different Magnet Arrangements," *19th International Conference on Electrical Machines and Systems (ICEMS)*, Nov. 2016.

[39] T. Masuko, and I. Miki, "A novel rotor structure of IPMSM with rare earth and ferrite magnets," *19th International Conference on Electrical Machines and Systems (ICEMS)*, Nov. 2016.

[40] L. Alberti, N. Bianchi, and S. Bolognani, "Variable-Speed Induction Machine Performance Computed Using Finite-Element," *IEEE Trans. Ind. Appl.*, vol. 47, no. 2, pp. 789-797, Jan. 2011.

[41] W. L. Soong, and N. Ertugrul, "Field-Weakening Performance of Interior Permanent-Magnet Motors," *IEEE Trans. Ind. Appl.*, vol. 38, no. 5, pp. 1251-1258, Oct. 2002.

[42] MineralPrices.com, [Online]. Available: http://www.mineralprices.com. Accessed: 2017-05-24.

[43] C. Du-Bar, "Design and analysis of a fault-tolerant fractional slot PMSM for a vehicle application," Thesis for the degree of Doctor of Philosophy in Engineering, Chalmers University of Technology, 2016. [Online]. Available: http://publications.lib.chalmers.se/records/fulltext/241697/241697.pdf.

[44] H. Cai, B. Guan, and L. Xu, "Low-Cost Ferrite PM-Assisted Synchronous Reluctance Machine for Electric Vehicles," *IEEE Trans. Ind. Electron.*, vol. 61, no. 10, pp. 5741-5748, Oct. 2014.

[45] A. Nordelöf, PhD Candidate, Environmental Systems Analysis, Chalmers University of Technology, private communication, May 2017.

[46] H. Jin, P. Afiuny, T. McIntyre, Y. Yih, and J. Sutherland, "Comparative Life Cycle Assessment of NdFeB Magnets: Virgin Production versus Magnet-to-Magnet Recycling," *Procedia CIRP*, vol. 48, pp. 45-50, May 2016.

[47] M. Simonsen, "Metal production," Vestlandsforskning, 2009. [Online]. Available: http://sip1.vestforsk.no/pdf/Felles/MetalProduction.pdf. Accessed: 2017-05-29.

[48] G. Kylander, "Thermal modelling of small cage induction motors," Thesis for the degree of Doctor of Philosophy in Engineering, Technical Report No. 265, Chalmers University of Technology, 1995.